TECHNISCHE UNIVERSITÄT
MÜNCHEN

Max-Planck-Institut für extraterrestrische Physik

Advanced Photometric Studies of Gamma-ray Burst Afterglows

Thomas Christian Krühler

Vollständiger Abdruck der von der Fakultät für Physik der Technischen Universität München zur Erlangung des akademischen Grades eines

Doktors der Naturwissenschaften

genehmigten Dissertation.

Vorsitzender:		Univ.-Prof. Dr. A. J. Buras
Prüfer der Dissertation:	1.	Priv.-Doz. Dr. J. Greiner
	2.	Univ.-Prof. Dr. F. von Feilitzsch

Die Dissertation wurde am 10.09.2009 bei der Technischen Universität München eingereicht und durch die Fakultät für Physik am 17.11.2009 angenommen.

Abstract

Gamma-ray Bursts (GRBs) are cosmic, stellar explosions, that emit a typical amount of energy of 10^{51} erg in γ-rays on short time scales of 0.1 to 100 seconds. This energy is released via shocks in ultra-relativistic jets and makes GRBs the most luminous objects in the Universe after the Big Bang. The prompt emission in γ-rays is followed by a longer-lasting afterglow, which can be detected in all wavelengths ranges from radio, optical, to X- and γ-rays up to several days after the explosion. The large energy release and high luminosity of GRBs and their afterglows make them ideal probes for studies of the early Universe and the cosmic evolution.

This PhD thesis describes the basic principles and scientific applications of a new measurement technique designed for detailed studies of GRB afterglows. The Gamma-Ray Burst Optical/Near-infrared Detector (GROND), built and operated by the Max-Planck-Institut für extraterrestrische Physik in collaboration with the Thüringer Landessternwarte, is a seven-channel imager, capable of simultaneous observations in seven broad-band filters in the optical and the near-infrared wavelength regime (380 nm−2400 nm). GROND is mounted at the 2.2 m MPG/ESO telescope at LaSilla observatory, Chile, fully operational since spring 2007 and dedicated to GRB afterglow studies.

GROND's main goal is a fast determination of the photometric redshift of GRBs via the drop-out technique. Absorption of photons on neutral hydrogen leads to a characteristic edge in the spectral energy distribution of GRB afterglows. At redshifts larger than $z \sim 3$, this Lyman-α edge at wavelength $\lambda_\alpha(z) = 121.6$ nm$(1 + z)$ is well within GROND's sensitivity limits and can be used to rapidly measure the distance scale to the GRB. Multi-band photometry thus obtains the information which is crucial for a fine-tuned setting of spectroscopic follow-up observations to enable detailed studies of high-redshift afterglows.

The GROND measurements are unique in the field of optical/near-infrared astronomy and provide new insights into GRB physics and cosmology. The afterglows of the two most distant GRBs to date, GRB 080913 and GRB 090423, for example, were both observed with GROND. The latter is located at a redshift of $z = 8.3$, which corresponds to a light-travel time of 13.04 Gyr or an age of the universe of 620 Myr, and is hence the most distant object ever detected to date. Furthermore, GROND measured the distance scale to the most energetic GRB so far, GRB 080916C. A redshift determination is the most crucial step to connect the extreme characteristics of these explosions to cosmology and unified theories of quantum gravity.

The structure of this thesis can be summarized as follows: The first chapter introduces to the basic concepts and scientific background of GRB physics. Afterwards, instrumental details about GROND, as well as its unique observations are presented. This part contains information about the modus operandi, and the software tools developed for data reduction and analysis. Together with data obtained in different spectral regimes, in particular at X-ray energies, the GROND data constitutes a multi-wavelength data set, which allows detailed studies of GRB afterglow physics. Chapter 3, 4 and 5 demonstrate scientific applications of this data on the basis of observations obtained for the afterglows of GRBs 070802, 071031 and 080710.

The spectral energy distribution of the afterglow of GRB 070802 at a redshift $z = 2.45$ has a characteristic absorption feature, which is generally related to absorption of photons on graphite grains. This 2175 Å feature is known from the Local Group, but could never be observed at this high redshift, i.e. at such an early stage of the universe. The GROND observations clearly showed, that Milky Way- or Large Magellanic Cloud-like dust was already formed in substantial amounts in a galaxy 2.7 Gyr after the Big Bang.

Superimposed to the optical and X-ray light curve of the afterglow of GRB 071031, which is a member of the GRB subclass of X-ray Flashes (XRFs), appears variability on relatively short time scales. Using the color information obtained with GROND and X-ray data, this variability can be related to continuous activity of the burst's inner engine. This result demonstrates, that the physical mechanisms producing GRBs are active on a time scale of hours, and hence much longer than suggested by measurements of the prompt γ-ray emission.

The optical light curve of the afterglow of GRB 080710 shows a characteristic early increase in brightness, which can be explained by a geometric offset of the observer with respect to the symmetry axis of the jet. A unified theory of standard GRBs and the softer XRFs might be obtained when attributing the observed morphology of the early optical light curves to different sight lines and the angular dependence of emitted energy with respect to the jet axis.

Zusammenfassung

Gammastrahlen Blitze (GRBs) sind kosmische Sternenexplosionen, die auf kürzesten Zeitskalen (0,1 bis 100 Sekunden) enorme Energien von etwa 10^{51} erg über Photonen im Bereich der γ-Strahlung abgeben. Damit stellen GRBs die energiereichsten Explosionen im Universum nach dem Urknall dar. Diese Energie wird über Synchrotronstrahlung von Elektronen in Stoßwellen eines Jets, dem gerichteten Ausstoß hoch-relativistischer Teilchen, erzeugt. Der prompten γ-Strahlung eines GRBs folgt das sogenannte Nachleuchten, eine über mehrere Tage abfallende Emission von Photonen in sämtlichen Energiebereichen des elektromagnetischen Spektrums. Durch die enorme Helligkeit von GRBs und die ihres Nachleuchtens sind sie ausgezeichnete Proben des frühen Universums, und können dazu benutzt werden, dessen Entwicklung seit der ersten Sternengeneration zu untersuchen.

Die vorliegende Dissertation beschreibt die wissenschaftlichen Grundlagen und Anwendungsbereiche eines Messverfahrens, welches am Max-Planck-Institut für extraterrestrische Physik in Kollaboration mit der Thüringer Landessternwarte entwickelt wurde, um detailliert das Nachleuchten von GRBs zu untersuchen. Der Gamma-Ray Burst Optical/Near-infrared Detector (GROND) ist eine astronomische Kamera, welche simultan in sieben verschiedenen Filterbändern beobachtet, und damit den kompletten Spektralbereich des sichtbaren Lichtes bis zu nah-infraroten Wellenlängen (380 nm$-$2400 nm) abdeckt. GROND wird dediziert zur automatischen Nachbeobachtung von GRBs eingesetzt, und am 2,2 m Teleskop der Max-Planck-Gesellschaft und der Europäischen Sternwarte der südlichen Hemisphäre des LaSilla Observatoriums in Chile betrieben.

Die Hauptanwendung der GROND Kamera besteht in der schnellen Messung der photometrischen Rotverschiebung von GRBs mit Hilfe der sogenannten Drop-out Technik. Bei Rotverschiebungen größer als $z \sim 3$ befindet sich die Absorption von Photonen an neutralem Wasserstoff, die Lyman-α Kante, deutlich innerhalb des Messbereichs von GROND. Diese Absorption bei einer Wellenlänge von $\lambda_\alpha(z) = 121{,}6\ \mathrm{nm}(1+\mathrm{z})$ lässt sich als charakteristische Kante innerhalb der spektralen Energieverteilung des Nachleuchtens mit GROND eindeutig nachweisen, und ermöglicht auf diese Weise eine schnelle Bestimmung der Entfernung des GRBs. Mit dieser Information können weitere Beobachtungen des Nachleuchtens, insbesondere hochauflösende Spektroskopie, auf dessen Helligkeit und die Rotverschiebung des GRBs angepasst, und somit genauer durchgeführt werden als jemals zuvor.

Die in dieser Arbeit vorgestellte Messmethode und ihre Anwendungen sind einzigartig im Bereich der optischen, beziehungsweise nah-infraroten Astronomie und ermöglichen neue Erkenntnisse im Bereich der GRBs und Kosmologie. Beispielsweise wurde in kürzester Zeit die Rotverschiebung zu den zwei bislang entferntesten GRBs (080913 und 090423) gemessen. Letzterer ist mit einer Rotverschiebung von $z = 8{,}3$, welche etwa einem Alter des Universums von 620×10^6 Jahren entspricht, das zur Zeit weitentfernteste, vom Menschen beobachtete Objekt im Universum. Ebenso konnte die Rotverschiebung des bislang energiereichsten Gammablitzes (GRB 080916C) mit GROND bestimmt werden. Die Entfernungsbestimmung zu GRBs ist ein essentieller Schritt um die beispiellosen Eigenschaften dieser Explosionen in Zusammenhang mit Kosmologie und vereinheitlichten Theorien der Quantengravitation zu bringen.

Die vorliegende Arbeit gliedert sich wie folgt: Kapitel 1 führt in die physikalischen Grundlagen und wissenschaftlichen Zusammenhänge von GRB Theorie und Beobachtungen ein. Im folgenden Kapitel werden Einzelheiten des Messverfahrens und der GROND Kamera beschrieben. Es wird im Detail auf die Datenerfassung und die im Rahmen dieser Dissertation entwickelte Software zur Datenreduktion und -analyse eingegangen. Die Kombination mit Daten aus anderen Spektralbereichen, insbesondere aus dem Röntgenbereich, ermöglicht genaue Untersuchungen des Nachleuchtens von GRBs. Anhand der Beispiele von drei GRBs (070802, 071031 und 080710) wird demonstriert, welche neuen Forschungsergebnisse mit Hilfe von exakter Photometrie in mehreren Filtern gleichzeitig gewonnen werden können.

Kapitel 3 befasst sich mit GRB 070802 bei einer Rotverschiebung von $z = 2{,}45$. Dessen Nachleuchten zeigte in seiner spektralen Energieverteilung die charakteristische Absorption von kohlenstoffhaltigem Staub. Dieses sogenannte 2175 Å Feature, welches aus Galaxien der Lokalen Gruppe bekannt ist, konnte somit erstmals bei hohen Rotverschiebungen, das heißt in einem sehr frühen Stadium des Universums, nachgewiesen werden. Aus den GROND Messungen kann daher geschlossen werden, dass Staub in einer Form, die etwa dem der Milchstraße oder der Großen Magellanschen Wolke gleicht, bereits bei einem Alter des Universums von $2{,}7 \times 10^9$ Jahren in signifikanten Mengen erzeugt worden sein muss.

Kapitel 4 behandelt GRB 071031 bei $z = 2{,}69$, der zur Klasse der Röntgenstrahlen Blitze (XRFs) gehört. Überlagert zu dem typischen Nachleuchten wurde hier Variabilität gemessen, welche mit Hilfe der zeitlichen und spektralen Signatur dem charakteristischen Verhalten von verzögerter Aktivität des GRBs zugeordnet werden kann. Dieses Ergebnis zeigt deutlich, dass die Prozesse, die einem GRB zu Grunde liegen, mehrere Stunden andauern können, und somit wesentlich länger, als die Beobachtungen der γ-Strahlung nahelegen.

Kapitel 5 beschreibt Beobachtungen des Nachleuchtens von GRB 080710 bei $z = 0{,}85$, die unmittelbar nach dem GRB eingeleitet wurden. Diese zeigen einen charakteristischen Helligkeitsanstieg der Lichtkurve, der sich mit relativistischen Effekten und einem geometrischen Versatz des Beobachters von der Symmetrieachse des GRBs erklären lässt. Anhand von GRB 080710 kann gezeigt werden, dass verschiedene Sichtlinien und die Winkelabhängigkeit der emittierten Strahlung vom Abstand von der Jetachse zu einer vereinheitlichten Theorie von spektral harten GRBs und weichen XRFs führen könnten.

Contents

Chapter 1

A Short Introduction to Gamma-ray Burst Physics and Observations

Only very few other subjects in astronomy have shown a comparable evolution in the recent past as the field of Gamma-ray Burst (GRB) science. First detected in the late sixties as mysterious, brief flashes of γ-rays, it has been demonstrated by now that a GRB is a violent, extragalactic, stellar explosion followed by a longer-lasting afterglow. The class of GRBs and their afterglows thus comprehends the most energetic, luminous and distant events in all energy ranges from the radio band to γ-rays detected by mankind at redshifts from $z = 0.0085$ (Galama et al., 1998) up to $z = 8.3$ (Tanvir et al., 2009; Salvaterra et al., 2009).

Apart from their intrinsic record-breaking properties, which make GRBs ideal tools for studies of the early Universe, their physical nature is still hardly understood. While there is strong evidence that long GRBs with a typical duration of $T_{90} \gtrsim 2$ s are related to the collapse of super-massive, fast-rotating Wolf-Rayet stars, the progenitors of short-duration ($T_{90} \lesssim 2$ s) GRBs remain to be identified. Other open questions include what governs the burst's central engine, the microphysical conditions in the ejecta, the amount of beaming and jet structure and whether the prompt emission properties can be used to turn GRBs into standard candles. The latter would enable direct tests of cosmology out to redshift of 8 and above.

The discovery of GRBs, which triggered a large number of space and ground-based follow-up programs was made in 1967 by the *Vela* satellites, that monitored the compliance of the nuclear test treaty, and published in 1973 (Klebesadel et al., 1973). At that time, space astronomy was just beginning to play an important role in science, and it took until 1991 to launch a mission designated for high-energy astronomy and GRB physics. The Compton Gamma-Ray Observatory (CGRO) hosted four instruments sensitive to photons from 30 keV to 30 GeV, where the Burst And Transient Source Experiment (BATSE) was specifically designed for GRB prompt emission studies. Until its deorbit in 2000, BATSE detected over 2700 GRBs, and obtained the bulk of information about the prompt emission characteristics available to date. In 2009, two major satellite missions are in orbit to study the afterglow (*Swift*, since 2004, Gehrels et al., 2004) and

prompt phase (*Fermi*). Launched in 2008, the two instruments onboard *Fermi*, the GRB Monitor (GBM, Meegan et al., 2009) and the Large Area Telescope (LAT, Atwood et al., 2009) with their combined sensitivity over 7.5 decades of energy from 8 keV to 300 GeV open a new field of physics regarding prompt emission properties (see Fig 1.1 and Abdo et al., 2009a,b). In addition, several other space missions have GRBs as one of their primary science drivers (e.g., the Italian satellite "Astro-rivelatore Gamma a Immagini Leggero" (AGILE), the International Gamma-Ray Astrophysics Laboratory (INTEGRAL) or Suzaku).

In addition to the space observatories, a large number of ground-based projects aim on gathering information about the afterglow. Most crucial is the determination of the distance scale to the GRB, i.e. a redshift measurement with atomic absorption lines via optical spectroscopy, typically performed with telescopes of the 8 m class. But also smaller-sized, robotic telescopes play an important role, especially with respect to the early phase of the GRB. As the very early afterglow, or the optical emission related to the prompt phase, can be extremely bright, small telescopes with aperture sizes in the range of 15 to 80 cm are able to obtain valuable data during the first stages of the explosion. Although limited to the brighter end of the afterglow distribution, the rapid response and slewing capabilities of order few ten seconds provide information which is not accessible by other means. Located in between in detection efficiency and response time is the growing number of instruments dedicated to and specialized on afterglow studies mounted on telescopes of the 2 m class. With somewhat longer slew times, but greatly enhanced sensitivity as compared to small robotic telescopes, these instruments are able to provide a complete and unbiased sample of afterglows, and the trigger information for 8 m class telescopes, as brightness of the optical transient and redshift estimates. Pioneering in this field is the Gamma-Ray Burst Optical/Near-infrared Detector (GROND, Greiner et al., 2008), a seven-channel imager in the optical and near-infrared regime mounted at the 2.2 m MPG/ESO telescope at LaSilla observatory, Chile. Noteworthy are also the projects which study the low-energy afterglow, in particular in the radio and sub-millimeter band, and studies of the host galaxy properties with large aperture ground-based telescopes and the Hubble Space Telescope (HST) in the optical/near-infrared and the Spitzer Space Telescope in the mid-infrared. Only a combination of data obtained with satellites and ground-based follow-up, is able to provide a complete picture of the event, followed from start to finish.

1.1 The Fireball Scenario

1.1.1 The Prompt Phase

First studies of the γ-ray phenomenology with BATSE data showed, that GRBs are distributed isotropically over the sky (Meegan et al., 1992; Fishman et al., 1994; Paciesas et al., 1999), strongly supporting cosmological distances (see Fig. 1.2, also Section 1.4). According to their duration distribution, which is roughly bimodial, GRBs can be divided into two populations (Kouveliotou et al., 1993): Long ($T_{90} \gtrsim 2$ s) versus short ($T_{90} \lesssim 2$ s) bursts. Their photon spectra as a function of energy $N(E)$, are non-thermal (see Fig 1.1), and typically well described with the empirical Band function (Band et al., 1993) of two power laws with low- and high-energy photon index $\alpha \sim -1$ and

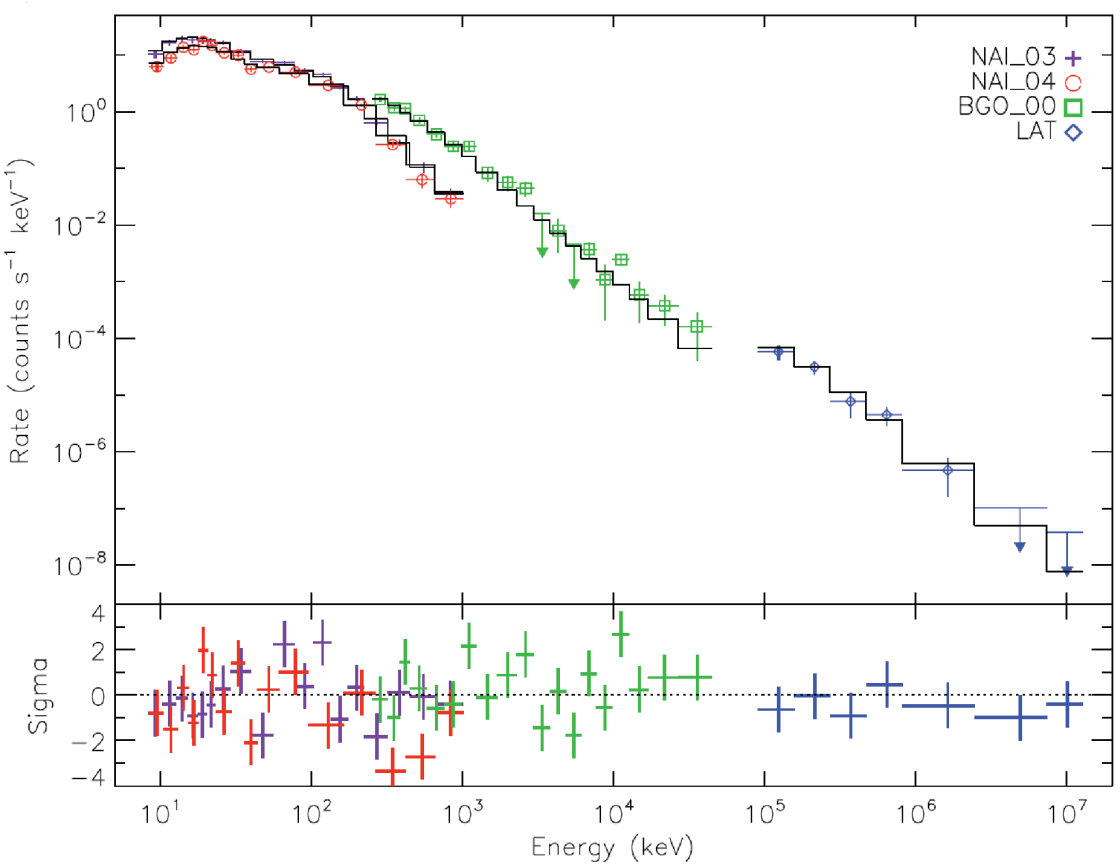

Figure 1.1 In the top panel the prompt emission count spectrum from GRB 080916C (Abdo et al., 2009a) as obtained with the two instruments onboard *Fermi*, GBM and LAT. Shown is the combined data from three different detectors from the GBM, two NaI (purple and red) and one Bismuth germanate (BGO, green) scintillator together with the LAT data (blue). The spectrum is well described with a Band function (black) over six decades of energy (10 keV to 10 GeV). The lower panel shows the residuals of the data to a Band function fit. The redshift of this burst is $z = 4.35^{+0.15}_{-0.15}$ (Greiner et al., 2009c), as obtained with GROND with the tools developed and described in this thesis (Chapter 2). The figure is adapted from Abdo et al. (2009a).

$\beta \sim -2.3$, smoothly connected at a peak energy $E_{\rm peak}$ in the 300 keV range with a large spread from few keV to MeV (Preece et al., 2000; Kaneko et al., 2006).

$$N(E) = \begin{cases} N_0 E^{\alpha} \exp\left(-\frac{E(2+\alpha)}{E_{\rm peak}}\right), & E < \frac{(\alpha-\beta)E_{\rm peak}}{(2+\alpha)} \\ N_0 \left[\frac{(\alpha-\beta)E_{\rm peak}}{(2+\alpha)}\right]^{\alpha-\beta} E^{\beta} \exp(\beta-\alpha), & E > \frac{(\alpha-\beta)E_{\rm peak}}{(2+\alpha)} \end{cases}$$

The temporal structure of the prompt emission is very irregular, and many bursts show variability time scales much shorter than the duration of the burst, i.e. substructure in the range of milliseconds (Fishman et al., 1993, see also Fig. 1.3). Together with the cosmological distances, a typical fluence detected in γ-rays of $10^{-4} - 10^{-7}$ erg/cm^2 (Paciesas et al., 1999), translates to an isotropic energy release of order $10^{52} - 10^{55}$ erg, or up to few solar rest-masses transformed into γ-rays. Generally, the energy emitted in neutrinos or gravitational waves in such a violent explosion, e.g., core-collapse supernovae (ccSN), is a factor 100 higher than what is released in pho-

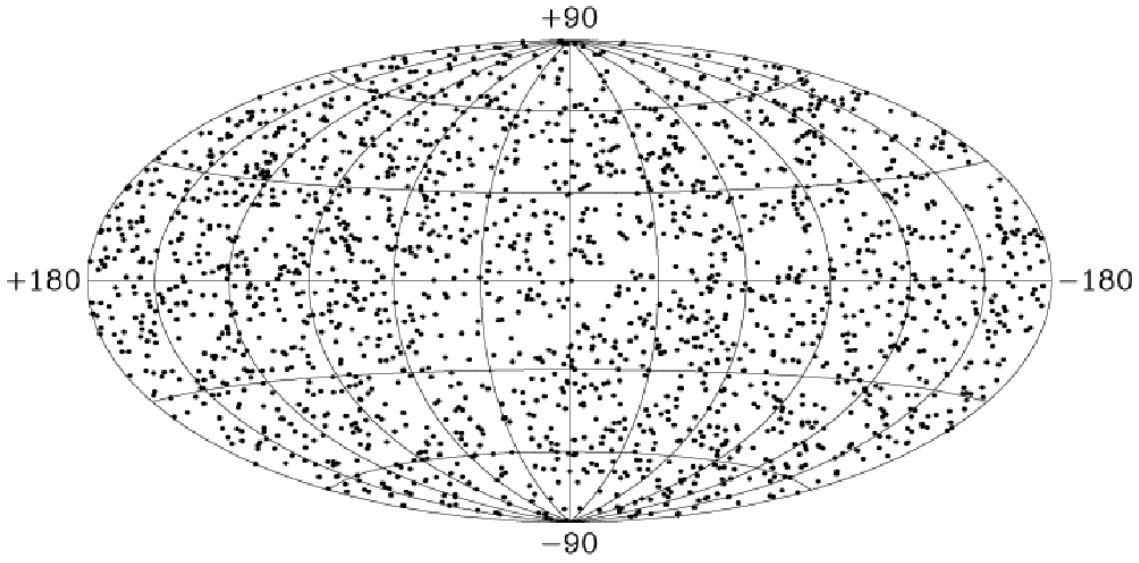

Figure 1.2 The BATSE GRB sky map in galactic coordinates. GRBs are distributed isotropically over the sky, and there is no excess in either the galactic or supergalactic plane for long bursts. Adapted from Paciesas et al. (1999).

tons, challenging the gravitational energy budget accessible to even the most massive stars. The measured γ-ray fluence thus strongly supports a beamed emission (Rhoads, 1997), which would relax the conditions of energy release in photons to $\sim 10^{51}$ erg (Frail et al., 2001), making the total amount of emitted energy comparable to ccSN, though released on much shorter time scales.

Due to causality arguments with respect to the short variability time scales, these high fluences must originate from compact regions, which then implies a formation of a fireball mostly consisting of photons and electron/positron pairs (Paczynski, 1986). As the luminosity in this small region is much larger than the Eddington Luminosity, the fireball naturally expands relativistically (Paczynski, 1986), if the baryonic load is sufficiently small (Shemi & Piran, 1990). A highly relativistic expansion is also required to overcome the so-called compactness problem, as at rest the fireball would be optically thick against pair production for the observed photons in the MeV to GeV range (Fenimore et al., 1993). The Lorentz factor of the outflow Γ then must comply with (Mészáros, 2002, see also Lithwick & Sari, 2001):

$$\Gamma \gtrsim 10^2 (\epsilon_{\gamma,10\mathrm{GeV}})^{1/2} (\epsilon_{t,1\mathrm{MeV}})^{1/2}$$

to produce $\epsilon_\gamma = 10\,\mathrm{GeV}$ photons against target photons of $\epsilon_t = 1$ MeV in the burst's rest-frame. The schematic behavior of the Lorentz factor of the outflow and the location of characteristic radii in the evolution of the fireball is shown in Fig. 1.4. The energy of the fireball is released in shocks, where the kinetic energy of the outflow is efficiently transformed into non-thermal particle and photon energies (Rees & Mészáros, 1992). Internal shocks between ejected shells with different Lorentz factors are thought to produce the prompt emission, and external shocks with the circumburst medium generate the afterglow emission both via synchrotron radiation (Rees & Mészáros, 1994). The characteristic synchrotron frequency ν_m of the outflow, blueshifted due to the highly

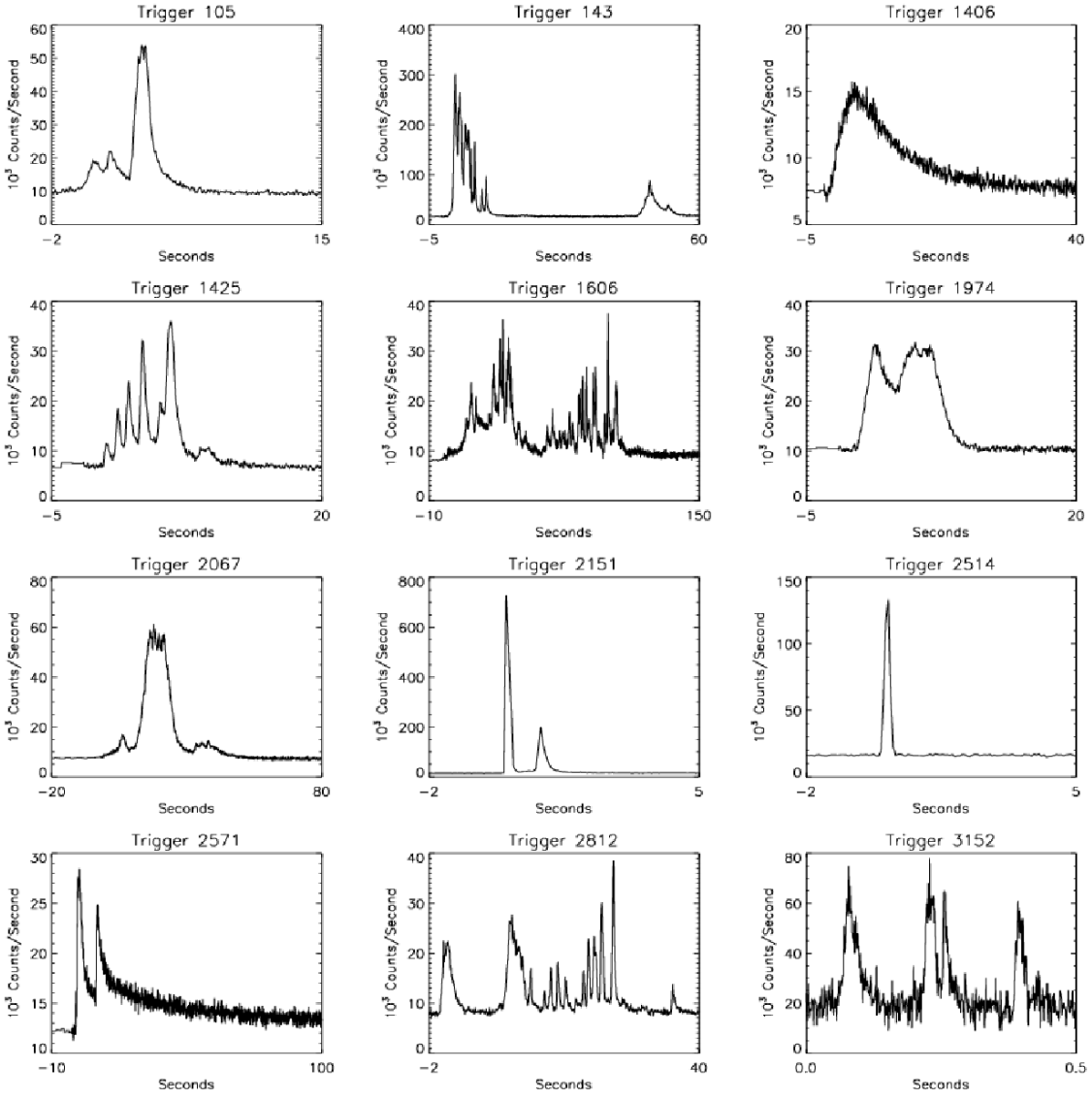

Figure 1.3 Variety of GRB light curves from the BATSE sample. The duration and morphology is very diverse for different bursts. GRBs can be very long (e.g., left bottom, trigger 2571 or trigger 1606), extremely short (trigger 2151, 2514, 3152), very spiky (trigger 143, 1425, 1606, 2812, 3152) or rather smooth (trigger 1406), and some of them seem to consist out of a superposition of different peaks. One of the most commonly inferred GRB morphologies is the fast rise exponential decay (FRED) pulse profile (e.g., trigger 1406, or two FREDs for trigger 2571). Please note the different time scales. Data from the public BATSE archive http://gammaray.msfc.nasa.gov/batse/grb/catalog/ (Paciesas et al., 1999).

relativistic motion into the observers frame is then dependent on the strength of the magnetic field B, and the Lorentz factors of the shocked relativistic electrons γ_e and of the emitting material Γ:

$$\nu_{\rm m} \sim q_e B/(2\pi m_e c)\gamma_e^2\Gamma$$

with the charge q_e and mass m_e of the electron. The emitted power P in the ejecta's co-moving rest-frame $P_{\rm rest}$ or observers frame $P_{\rm obs}$ by a single electron with γ_e, assuming no significant energy losses due to cooling, can be calculated accordingly:

$$P_{rest} = (4/3)\sigma_T c U_B \gamma_e^2$$
$$P_{obs} = \Gamma^2(4/3)\sigma_T c U_B \gamma_e^2$$

with the Thomson cross section σ_T and the magnetic field energy density $U_B = B^2/8\pi = \epsilon_B e$. Here, ϵ_B is the ratio of magnetic energy to the total energy density e dissipated in the shock.

Typically, the energy- or velocity distribution of particles in the shock $N(\gamma)$ is described as a power law above a certain minimal Lorentz factor γ_m (e.g., Sari et al., 1998),

$$N(\gamma) \propto \gamma^{-p}$$

with the spectral index $p > 2$, to keep the total integrated energy finite. Initially, γ_m is equal for protons and electrons, and the energy ratio carried by electrons versus protons is $\sim m_e/m_p$. Collisionless shocks via chaotic electric and magnetic fields, however, can redistribute the energy between protons and electrons, a process which is usually described by the fraction of energy ϵ_e which goes into electrons (Mészáros, 2006). Furthermore, only a fraction of all shocked electrons ξ_e will be accelerated above γ_m (Bykov & Mészáros, 1996). By integrating over the initial velocity distribution $N(\gamma) \propto \gamma^{-p}$ one obtains the minimal Lorentz factor of the electron population:

$$\gamma_m \sim g(p)(\epsilon_e/\xi_e)(m_p/m_e)\Gamma$$

where $g(p) = (p-2)/(p-1)$. The theoretical synchrotron spectrum $F_\nu(\nu)$ is then a broken power law with $F_\nu \propto \nu^{1/3}$ at $\nu < \nu_{\rm m}$ and $F_\nu \propto \nu^{-(p-1)/2}$ for $\nu > \nu_{\rm m}$ (Rybicki & Lightman, 1979). The power-law shape and the spectral indices below and above $\nu_{\rm m}$ are roughly compatible with the observations over a large energy range (see Fig. 1.1) and thus support the energy dissipation in shocks via synchrotron radiation.

This fireball and its synchrotron radiation due to shocks are the main characteristics and the only observables of the progenitor, and the emission from the remnant remains hidden as it is dominated by the much brighter internal and external shocks. Hence, direct observations of the central engine are practically unfeasible, independent of the optical thickness of the outflow.

Alternatively to the fireball origin of the prompt GRB emission, several models have been pro-

posed which invoke different speculative radiation scenarios. The most plausible ones consider the prompt emission from highly magnetized or Poynting flux dominated outflows via the dissipation of field energy or magnetic reconnection (e.g., Mészáros et al., 1994; Usov, 1994; Drenkhahn & Spruit, 2002). Magnetic reconnection would lead to particle acceleration, and in the case of a slow energy dissipation the environment would be optically thin for the synchrotron radiation of the accelerated particles in the presence of the magnetic field of the outflow (Spruit & Drenkhahn, 2004). A magnetic field would thus provide the particle acceleration and energy dissipation mechanisms via synchrotron radiation to produce prompt γ-rays, followed by a standard external shock and the afterglow (see Section 1.1.2).

Other alternative models consider non-fluid, ultra-relativistic ejecta in the form of "cannonballs" in a supernova explosion (e.g., Dar & de Rújula, 2004). These bullets, which have about the mass of the Earth, produce prompt γ-ray emission by inverse Compton scattering of supernova light, and the afterglow by thermal bremsstrahlung and synchrotron radiation of accelerated electrons of the ambient medium (Dado et al., 2002). However, several unresolved issues remain in the cannonball model, for example the mechanism of coherent bullet formation and discrete nature of the ejecta. The latter is particularly controversial, as most high-energy astrophysical phenomena (e.g., the jets of Active Galactic Nuclei) are probably related to fluid or plasma outflows (Mészáros, 2006). Despite the lack of conclusive alternatives to the fireball model, also the standard models remain largely phenomenological and the radiation mechanism of the prompt emission, the role of magnetic fields and the microphysics of shocked particle acceleration stays the subject of discussion (Mészáros, 2006).

1.1.2 The Afterglow

As soon as the fireball ejecta expand into the circumburst medium, inevitably external shocks start to develop. The interaction of the ultra-relativistic shells and the external medium then gives rise to afterglow emission from radio to X-ray energies, first detected for GRB 970228 (van Paradijs et al., 1997; Vietri, 1997; Wijers et al., 1997; Frontera et al., 1998). The emission from external shocks is dependent on the amount of material which has been swept up by the shock-wave and reaches maximum luminosity at the typical deceleration radius $r_{\rm dec}$ and observed time $t_{\rm dec}$ (Rees & Mészáros, 1992; Mészáros & Rees, 1993):

$$r_{\rm dec} \sim (3E_0/(4\pi n_{\rm ext} m_p c^2 \Gamma_0^2))^{1/3}$$

$$t_{\rm dec} \sim r_{\rm dec}/(2c\Gamma_0^2)$$

with the isotropic equivalent energy released in γ-rays E_0, the external matter density $n_{\rm ext}$ and the proton mass m_p. At that point the Lorentz factor of the outflow $\Gamma_{\rm dec}$ is expected to be half of the initial Lorentz factor of the bulk of the emission Γ_0 (Panaitescu & Kumar, 2000). The dependency of the Lorentz factor on the radius is schematically shown in Fig. 1.4. An analytical calculation including the efficiency of the radiative energy transfer η and the cosmological redshift z, yields (Sari & Piran, 1999):

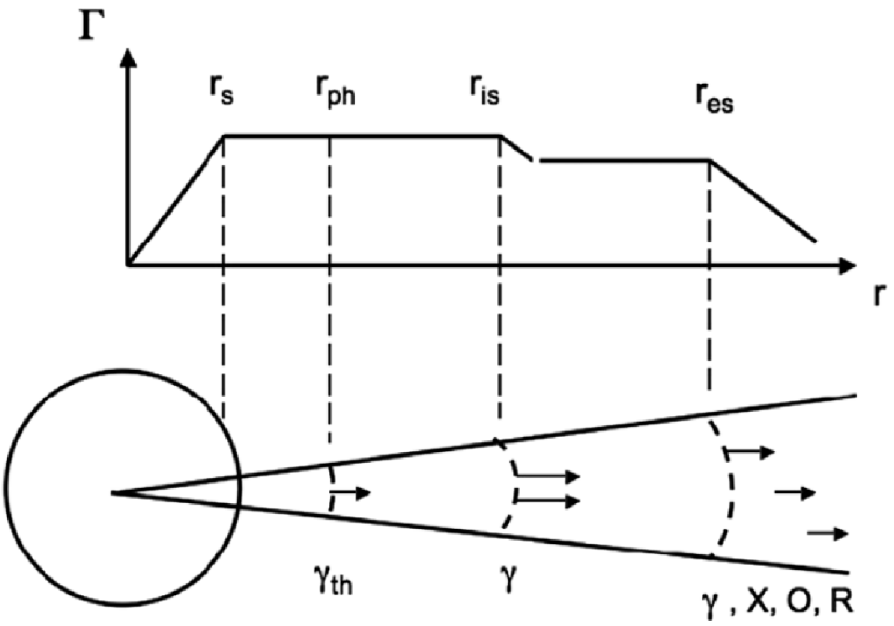

Figure 1.4 Schematic behavior of the jet's Lorentz factor Γ and nominal location of different radii. $r_{\rm s}$ is the saturation radius where the fireball is not accelerated anymore, $r_{\rm ph}$ the photospheric radius, where the Thompson optical depth τ is unity, $r_{\rm is}$ the dissipation radius for internal shocks, where two shells with different velocities typically catch up with each other producing the prompt emission, and $r_{\rm es} = r_{\rm dec}$ the external shock radius, where the circumburst medium starts to efficiently decelerate the ejecta which produces the afterglow. Both radial and velocity scale are logarithmic and $\gamma_{\rm th}$, γ, X, O and R indicate the location of thermal γ-ray production at the photosphere, or γ-ray, X-ray, optical and radio photon emission via synchrotron radiation. From Mészáros (2006).

$$\Gamma_{\rm dec} = \left(\frac{3E_0(1+z)^3}{32\pi n_{\rm ext} m_p c^5 \eta t_{\rm dec}} \right)^{1/8}$$

Measurements of the peak emission of the afterglow external shock can thus provide direct information about the conditions in the outflow, in particular the initial bulk Lorentz factor, the deceleration radius and the isotropic equivalent baryonic loading of the fireball $M_{\rm fb} = E_0/(\Gamma_0 c^2)$ (Molinari et al., 2007).

The emission from the external shock is again synchrotron radiation with a peak frequency $\nu_{\rm m}$, similarly proportional to the Lorentz factor of the ejecta, the electrons in the shock and the co-moving magnetic field as in the prompt phase (Mészáros & Rees, 1993). The particle and energy density (N/V and E/V, respectively) behind the forward shock propagating through a uniform and cold medium is given by the Blandford-McKee solution (Blandford & McKee, 1976), i.e. at first order $N/V(t) = 4\Gamma(t) n_{\rm ext}$ and $E/V(t) = 4\Gamma(t)^2 n_{\rm ext} m_p c^2$ (Piran, 1999). Under the assumption that the dominant emission process is forward shock emission, the entire spectrum of the afterglow can be calculated selfconsistently (Mészáros & Rees, 1997).

Above a critical Lorentz factor $\gamma_{\rm c}$, the electrons loose significant amount of their energy due to

cooling. γ_c is described by the time scale t it takes for an electron with $\gamma_e > \gamma_c$ to cool down to γ_c (Sari et al., 1998).

$$\gamma_c = \frac{6\pi m_e c}{\sigma_T \Gamma B^2 t}$$

The resulting theoretical afterglow spectrum is a three fold broken power law with spectral breaks at ν_a, the synchrotron self absorption, ν_m and ν_c, the cooling frequency (Sari et al., 1998; Granot & Sari, 2002a) and a maximum luminosity at $F_{\nu,\max}$. The part of the spectrum below ν_m is the low-frequency tail of the synchrotron radiation and independent on the electron spectral index p, i.e. $F_\nu \propto \nu^{1/3}$ (Katz, 1994). The high energy part above ν_c is described by the electrons with Lorentz factors greater than γ_c, which cool rapidly and emit practically all their energy at their synchrotron frequency. Following Sari et al. (1998), the afterglow spectrum is $F_\nu \propto \nu^{-p/2}$ in this regime, which gives direct observational access to the energy index of the electrons from the high energy spectral slope. Assuming that a constant fraction of the shock energy goes into electrons and the magnetic field, the shock wave is then fully defined by $n_{\rm ext}$, E_0, the energy index of the electrons in the shock p, and the efficiency factors of the magnetic field ϵ_B, of the electrons ϵ_e, the fraction of accelerated electrons ξ_e associated with the inter stellar material (ISM), the dependence of Γ on the radius r and the redshift z (Zhang & Mészáros, 2004). The time dependence of ν_a, ν_c, and ν_m in the adiabatic case ($\Gamma \propto r^{-3/2}$) is then given by (Zhang & Mészáros, 2004):

$$\nu_m(t) = (6\times10^{15})(1+z)^{1/2} g(p)^2 (\epsilon_e/\xi_e)^2 \epsilon_B^{1/2} E_{0,52}^{1/2} t_d^{-3/2}\,[\mathrm{Hz}]$$
$$\nu_c(t) = (9\times10^{12})(1+z)^{-1/2} \epsilon_B^{-3/2} n_1^{-1} E_{0,52}^{-1/2} t_d^{-1/2}\,[\mathrm{Hz}]$$
$$\nu_a(t) = (2\times10^{9})(1+z)^{-1} (\epsilon_e/\xi_e)^{-1} \epsilon_B^{1/5} n_1^{3/5} E_{0,52}^{1/5}\,[\mathrm{Hz}]$$

with $E_{0,52} = E_0$ in units of 10^{52} erg, n in 1 cm^{-3} and t in days.

The order of ν_m and ν_c defines two cases: the slow cooling ($\nu_m < \nu_c$) and fast cooling ($\nu_m > \nu_c$) case as shown in Fig. 1.5.

The normalization $F_{\nu,\max}$ is obtained by the flux integral over all radiating electrons, which is only a function of the turbulent magnetic field B in the shock, i.e. ϵ_B, and not of the other microphysical parameters ϵ_e, ξ_e and p (Wijers & Galama, 1999; Zhang & Mészáros, 2004):

$$F_{\nu,\max} = 20(1+z)\epsilon_B^{1/2} n^{1/2} E_{52} D_{\mathrm{L},28}^{-2}\,[\mathrm{mJy}]$$

where $D_{\mathrm{L},28}$ is the luminosity distance in units of 10^{28} cm.

A characteristic set of equations then relates the spectral index β, where $F_\nu(\nu) = \nu^{-\beta}$, to the temporal decay index of the light curve α, with $F_\nu(t) = t^{-\alpha}$. These closure relations depend on the type of circumburst medium, typically described with an index s, where $n_{\rm ext} \propto n_0^{-s}$, most commonly $s = 0$ for an homogeneous ISM-like circumburst medium, or $s = 2$ for a wind type environment. Furthermore, they differ between the spectral regime of slow or fast cooling

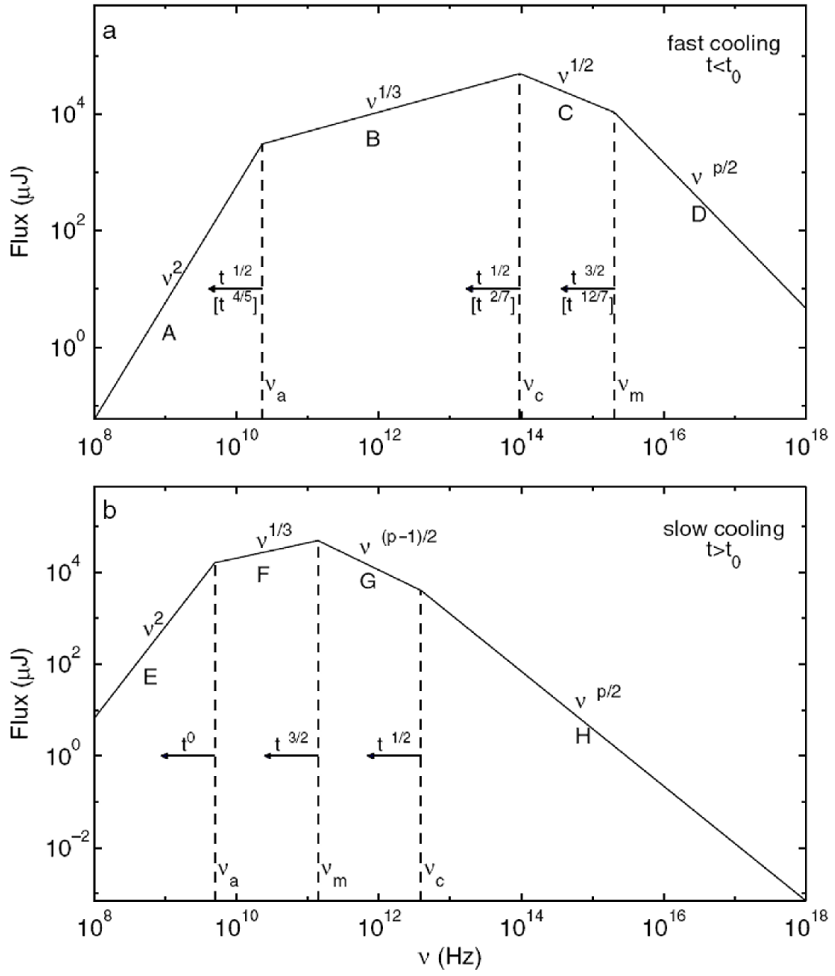

Figure 1.5 Schematic behavior of the different afterglow synchrotron spectra in the fast and slow cooling case. As the ejecta slow down, the characteristic frequencies move to lower energies. As the cooling frequency moves faster $\nu_{\rm c} \propto t^{-3/2}$ with respect to $\nu_{\rm m} \propto t^{-1/2}$, the afterglow is expected to go through a transition from fast to slow cooling regime at t_0. From Sari et al. (1998).

and the location of the observed frequency, the electron index p and a possible energy injection (e.g., Mészáros & Rees, 1997; Sari & Piran, 1999; Dai & Cheng, 2001; Zhang & Mészáros, 2004; Panaitescu, 2005; Zhang et al., 2006; Panaitescu et al., 2006b). Assuming the most simple condition of an ISM-like circumburst environment in the slow cooling case with $p \geq 2$ and no energy injection, the closure relation for $\nu_{\rm m} < \nu < \nu_{\rm c}$ or $\nu_{\rm c} < \nu$ is $\alpha = 3\beta/2$ or $\alpha = (3\beta - 1)/2$, respectively. By measuring the spectral and temporal index, the fireball model can thus be tested straight forwardly by observations, and the late ($t > 10^{4-5}$ s) afterglow generally was in good agreement with the expectations. With increasing temporal and spectral information of the afterglow after the advent of the *Swift* mission, however, more and more data about the early ($t < 10^{4-5}$ s) and late afterglow phase became available, raising questions about the validity and significance of the most simple fireball scenarios (see Section 1.2).

1.1.3 Jets and Jet Structure

Beamed emission from GRBs is already suggested by energetic considerations that GRBs must be related to an energy reservoir accessible to massive stars. If the outflow is collimated in a cone of half opening angle $\theta_{\rm jet}$ the evolution is similar to the spherical case, given that the relativistic beaming $1/\Gamma$ is smaller than $\theta_{\rm jet}$ and the observer is located face on to the jet (Mészáros et al., 1993). The light cone is then constrained to a region within the jet and disconnected from outer areas. As soon as the jet has decelerated to $1/\Gamma \sim \theta_{\rm jet}$, more energy is emitted in directions outside the central cone, and the jet starts to expand laterally with the co-moving speed of sound (Mészáros, 2006). This results in a characteristic steepening of the light curve of the afterglow with a change in the temporal index $\Delta\alpha \sim 3/4$ (Mészáros & Rees, 1999) if the sideways expansion is negligible, or a final decay with $\alpha = p$ when including the lateral spreading (Rhoads, 1999). These jet breaks are a pure geometrical effect, and thus truly achromatic by definition. One of the earliest detections of a jet break in a number of broad-band filters is shown in Fig. 1.6.

From the time $t_{\rm jet}$ where the break in the light curve occurs, the half opening angle of the jet can be calculated, depending on the redshift and circumburst profile (Sari et al., 1999; Bloom et al., 2003):

$$\theta_{\rm jet}^{\rm ISM} \approx 0.099 \left(\frac{t_{\rm jet}[\rm s]}{1+z}\right)^{3/8} \cdot \left(\frac{\eta_{0.2} n_1}{E_{0,53}}\right)^{1/8}$$

$$\theta_{\rm jet}^{\rm wind} \approx 0.075 \left(\frac{t_{\rm jet}[\rm s]}{1+z}\right)^{1/4} \cdot \left(\frac{\eta_{0.2} A_*}{E_{0,53}}\right)^{1/4}$$

where the burst characteristics have been normalized to typical values, e.g., E_0 to 10^{53} erg, n to 1 cm^{-3}, and A_* is the normalized wind density with $A = \dot{M}_{\rm w}/4\pi v_{\rm w} = 5 \times 10^{11} A_* {\rm g\ cm^{-1}}$. Here $\dot{M}_{\rm w}$ is the mass-loss rate of the progenitor in its final stage of stellar evolution and v_w the wind velocity with reference values of $\dot{M}_{\rm w} = 1 \times 10^{-5} M_\odot {\rm yr}^{-1}$ and $v_{\rm w} = 1000$ km/s, characteristic for a Wolf-Rayet star (Chevalier & Li, 2000).

With the knowledge of the jets opening angle, the beaming-corrected energy release in γ-rays

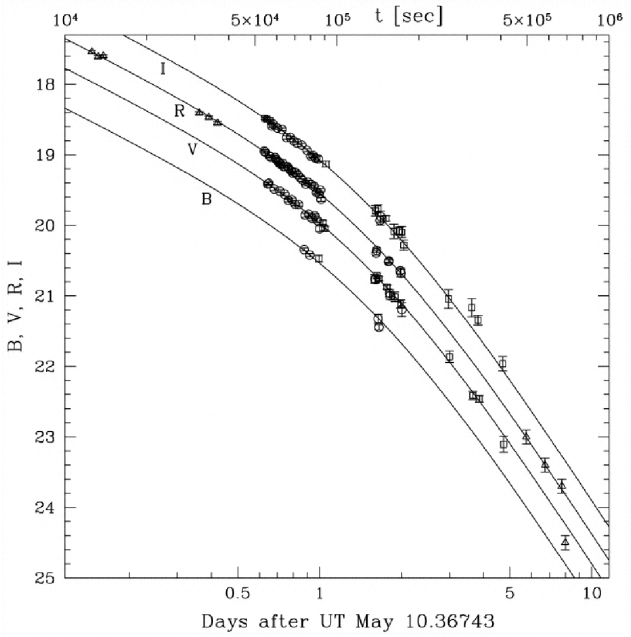

Figure 1.6 Multi-color light curve of the afterglow of GRB 990510 in four different photometric filters (B, V, R and I). The light curve is described by a characteristic smooth turnover from shallow to steep decay. This break in the light curve is generally related to the collimation of the ejecta and happens when the relativistic beaming is of the order of the jet half opening angle. From Stanek et al. (1999).

E_γ is then:

$$E_\gamma = f_\mathrm{b} E_0$$

where f_b is the beaming factor $f_\mathrm{b} = (1 - \cos\theta_\mathrm{jet})$. After correcting for the apparent beaming, the energy released in γ-rays by GRBs clusters at around $E_\gamma \approx 10^{51}$ erg, as shown in Fig 1.7 (Frail et al., 2001; Bloom et al., 2003). There is however, evidence for sub- and super-energetic bursts, with emitted beaming corrected energies significantly below or above 10^{51} erg, so the use of GRBs as direct standard candles is strongly questioned.

The apparently beamed emission of GRBs raises the question of the jet structure, i.e. the lateral energy distribution around the jets symmetry axis. Different jet configurations have been proposed, including the most popular uniform jet, where the energy distribution $\varepsilon(\theta)$ is described by a simple top hat. Frequently used is also the universal structured jet model, where $\varepsilon(\theta)$ is characterized by a power law with index k, i.e. $\varepsilon(\theta) = \varepsilon_c(\theta/\theta_c)^{-k}$ outside of a uniform core with angle θ_c (e.g., Lipunov et al., 2001). The jet structure of both models is schematically shown in Fig. 1.8. A more physical jet structure was introduced in Zhang & Mészáros (2002b) and Kumar & Granot (2003), where the angular profile of the jet is Gaussian shaped. In addition to these models of single jets, the combination of two components (e.g., Pedersen et al., 1998; Peng et al., 2005) has been used to explain the increasing diversity in optical afterglows. Here, the superposition of a narrowly collimated fast jet, and a broad jet with lower velocities can produce a broad type of afterglow light-curve morphologies. Further motivation for this model is provided by numerical

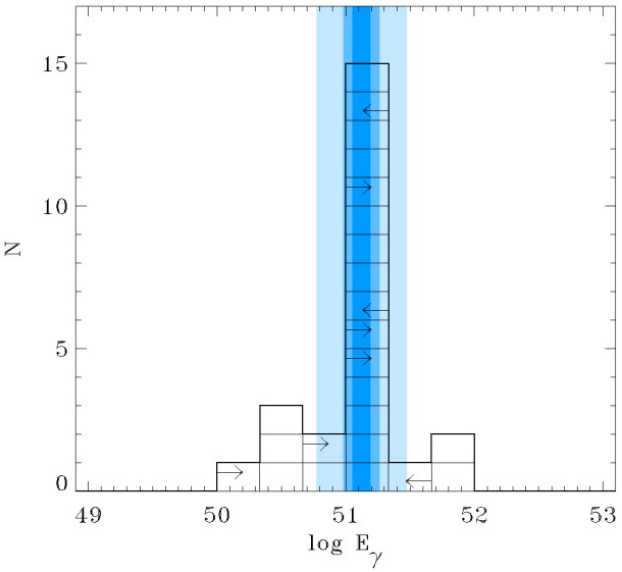

Figure 1.7 Clustering of the beaming-corrected energy release in γ-ray photons. After correcting the emitted energy for the jetted emission, there seems to appear a clustering around 10^{51} erg. There is however, evidence for sub- and super-energetic bursts in the recent years. Thus, GRBs are most probably not connected to a constant energy reservoir, which might have been deduced from earlier and limited samples. From Bloom et al. (2003).

simulations, which show evidence for a slower component around a hydrodynamically driven jet, that originates from compact objects (Ramirez-Ruiz et al., 2002; Vlahakis et al., 2003; Zhang et al., 2003b).

Although the morphology of the afterglow light curve is in principle a robust diagnostics for the jet structure (see Fig. 1.9), definite conclusions about the angular distribution of energy in the jet is not yet reached (e.g., Rossi et al., 2002). A part of the problem is related to the quality and quantity of obtained optical light curves, which are not well sampled in either time or frequency domain, and of inferior photometric accuracy. The lack of high quality data makes a comparison or discrimination between different jet structures so far inconclusive. Additional evidence about the jet structure can be obtained from polarization measurements (e.g., Wijers et al., 1999; Greiner et al., 2003a; Rossi et al., 2004). However, as in the case of light-curve modelling, previous measurements are not yet fully conclusive.

1.2 *Swift* and the Afterglow Era

After the launch of *Swift* in 2004, with its rapid slewing capabilities and two narrow field follow-up instruments, the X-ray- (XRT, Burrows et al., 2005b) and Ultraviolet/Optical Telescope (UVOT, Roming et al., 2005), observations of the early afterglow in the X-ray and ultraviolet/optical energy band were feasible for the first time in larger numbers of around 100 per year. One of the most surprising discoveries was the variety of features in the X-ray light curve. While previously, X-ray observations started earliest at 10 ks after the trigger, the fast *Swift* response now gives a complete description of the events starting as early as 100 s after the burst.

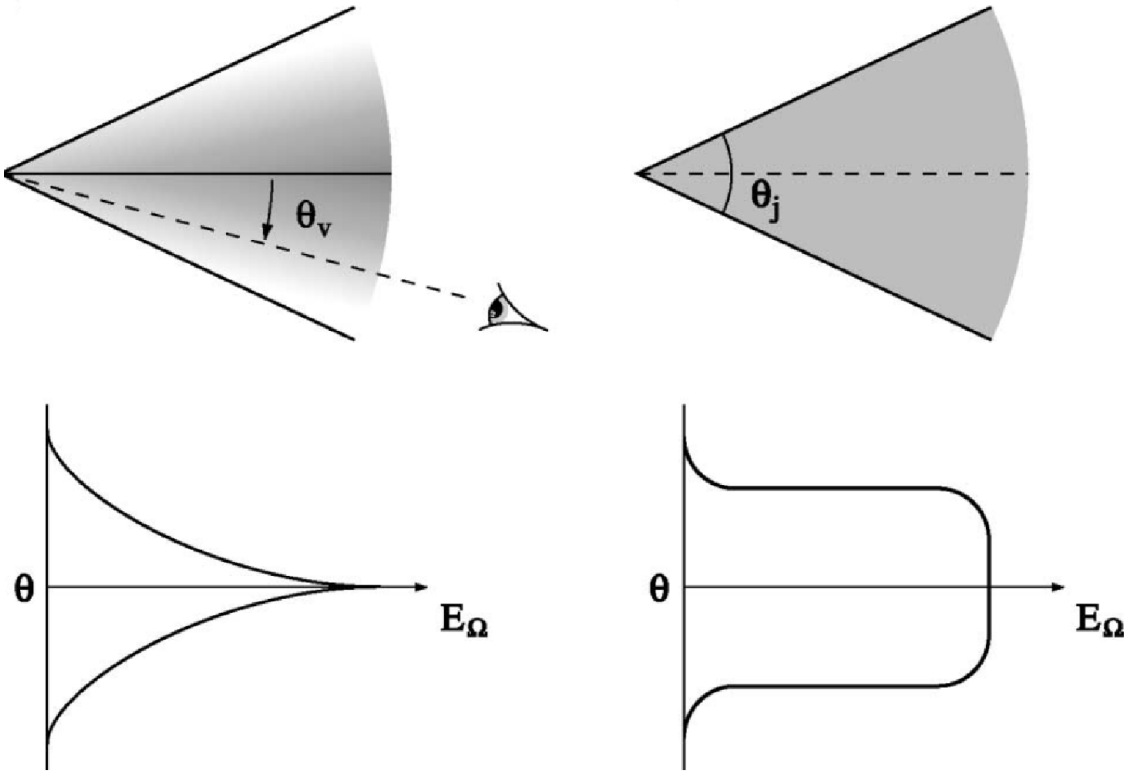

Figure 1.8 Schematic diagrams of the universal structured (left) and uniform jet model (right). $\theta_{\rm j}$ and $\theta_{\rm v}$ in the figure are $\theta_{\rm jet}$ and $\theta_{\rm obs}$ in the text. The universal structured jet shown here as a negligible inner cone, i.e. $\theta_c \sim 0$. Adapted from Lamb et al. (2005).

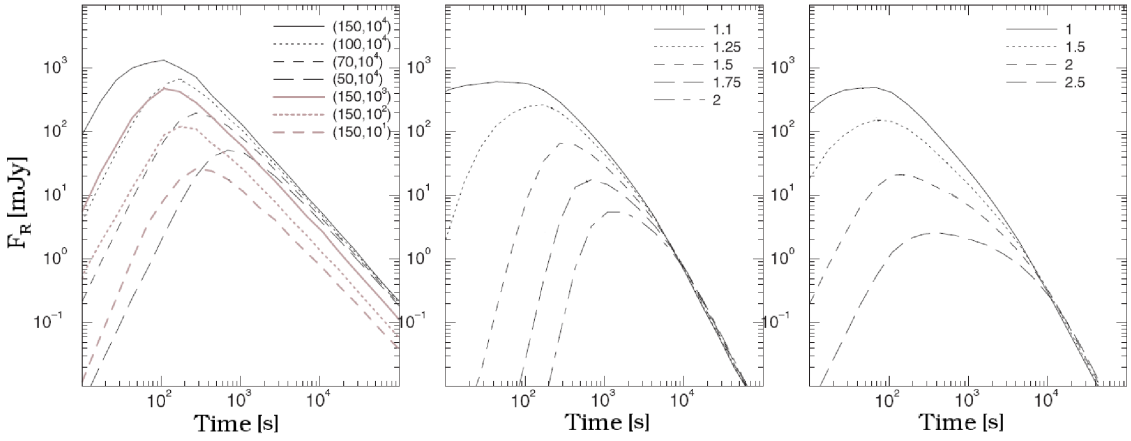

Figure 1.9 Numerical calculations of R-band optical light curves in different jet configurations. Left panel: Homogeneous uniform jet model with different initial Lorentz factors Γ, and circumburst media density n as shown as (Γ, n in cm^{-3}) in the key. The light curves initially rise in their pre-deceleration phase. The afterglow peak marks the onset of deceleration, i.e. the deceleration radius $r_{\rm dec}$. Middle panel: Uniform jet seen at different angles. The viewing angle is shown in the key as $\theta_{\rm obs}/\theta_{\rm jet}$. Right panel: Universal structured jet model seen at different angles. The power-law index k of $\epsilon(\theta) = \epsilon_c(\theta/\theta_c)^{-k}$ is 4 in this case. The viewing angle is shown in the legend as $\theta_{\rm obs}/\theta_{\rm c}$. Adapted from Panaitescu & Vestrand (2008).

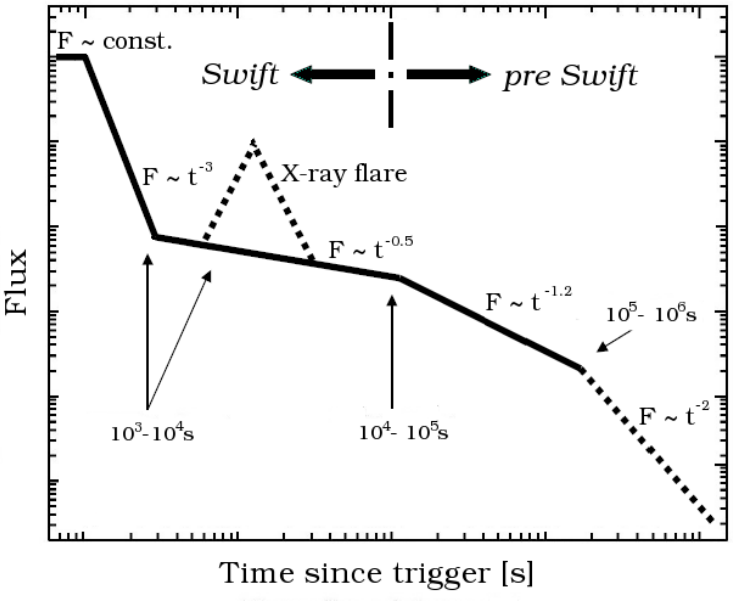

Figure 1.10 The canonical X-ray light curve in the *Swift* era. The very early X-ray data usually connect smoothly to the prompt emission. This is followed by a characteristic steep decline, related to high latitude emission. Afterwards there is a transition to a much shallower decline, or even plateau phase, which is followed by two breaks: first to the typical power-law decline of afterglow emission, and eventually a jet break. Superimposed onto all components X-ray flares can appear. Time scales are indicative, and not all features are present in all bursts. Dashed lines indicate sections which are only observed in a smaller fraction of afterglows. For physical processes shaping the X-ray light curve please see text. Adapted from Zhang et al. (2006).

1.2.1 A Generic X-ray Afterglow Light Curve

Already very early samples of *Swift* X-ray light curves showed, that there was evidence for a generic scheme underlying all X-ray afterglows (Nousek et al., 2006). Though not all features are observed in every burst, a single X-ray afterglow light curve can be described within the framework shown in Fig. 1.10. In detail, there is a very early stage which usually connects smoothly to the prompt emission (O'Brien et al., 2006), followed by a characteristic steep - flat - steep evolution. Finally, there is a late break in the light curve which is generally related to the jet break. It must be noted though, that the fraction of detections of achromatic late breaks consistent with a jet break is much lower than previously expected. Whether this apparent lack of jet breaks is the result of a larger redshift and beaming (on average, *Swift* detects fainter bursts at higher redshifts than previous missions) or the jet break in the X-ray band is masked by an additional emission component (e.g., flares, inverse Compton emission, separate jet component) is still a matter of debate (Sato et al., 2007; Ghisellini et al., 2007; Genet et al., 2007; Racusin et al., 2009). Superimposed to all epochs appear in roughly 50% of all cases X-ray flares which can be as energetic as the prompt phase itself (Falcone et al., 2006).

This generic scheme puts strong constraints on the physical concepts of the light curve and its implications about the central engine. The different stages in this generic light curve are discussed in detail below.

The Steep Decay

According to the standard fireball model (see Section 1.1), the prompt phase and the afterglow are emitted by internal and external shocks, and are thus spatially separated. In the very early phase, the emission from the prompt phase still dominates over the afterglow. A steep decay is expected due to the time delay of $t = (1+z)(r/c)(\theta^2/2)$ between the photons emitted along the line of sight and at an angle θ (e.g., Dermer, 2004). Hence, even after the energy dissipation in the prompt phase stops, there is a maximum delay of order $t_{\rm max} = (1+z)(r/c)(\theta_{\rm jet}^2/2)$, assuming that the observers line of sight is not far off the jet symmetry axis. The temporal and spectral dependence of the flux density F_ν for high latitude emission can be expressed using the co-moving surface brightness $L'_{\nu'}$ (Zhang et al., 2006), where ν' is the co-moving frequency of the shocked electrons. Transforming into the observers frame, using the Doppler factor $D = 1/(\Gamma(1-v\cos\theta/c))$ with the velocity of the outflow v, and thus $D \sim 2/\Gamma\theta^2$ as long as the relativistic beaming is much larger than θ, yields (Zhang et al., 2006):

$$F_\nu \propto L'_{\nu'} D^2 \propto \nu^{-\beta} D^{2+\beta}$$

Together with the dependence of the time delay on the emitting angle $t \propto \theta^2 \propto D^{-1}$, this becomes $F_\nu \propto L'_{\nu'} D^2 \propto \nu^{-\beta} t^{-2-\beta}$. Hence, the temporal decline index is $\alpha = 2 + \beta$ (Kumar & Piran, 2000). This relation is a characteristic for high-latitude emission and was shown to adequately describe samples of X-ray afterglows, where the steep decay is observed (Nousek et al., 2006; O'Brien et al., 2006). Therefore, the steep decay can be considered as the tail end of the prompt emission, and further is implicit proof that GRBs are beamed and that afterglow and prompt photons arise from different emission sites. Not all bursts, however, satisfy the earlier constraint. As the measured power-law index is strongly dependent on the choice of the reference time T_0, which is usually set to the trigger time, i.e. the start of the γ-ray emission, there is another degree of freedom which can be adapted to fit the relation for high-latitude emission. In fact, Liang et al. (2006) find, that the vast majority of steep tails can be accounted for with high-latitude emission if T_0 is set to the time of the last pulse of the burst, which is physically reasonable as this last pulse would largely dominate any tail emission.

The Shallow Decay Phase

The tail end of the prompt emission is usually followed by a plateau phase, with a decline index of order $\alpha \sim -0.5$ which is too shallow for the expectations from the standard model ($\alpha \sim -1.2$). Additional evidence that the shallow decay phase is physically different from the early steep decline is provided by spectral evolution. Typically the spectrum hardens during the steep - shallow transition. Hence, the shallow phase is usually considered as the first part of the light curve where the afterglow dominates. However, as the decline index is too shallow to be accounted for in the original form of the fireball model, there needs to be some sort of additional energy which is injected into the forward shock-wave during this epoch (Nousek et al., 2006).

The most popular mechanism of energy injection is the so-called refreshed shock scenario,

where later or slower shells catch up with the decelerating shock. These refreshed shocks might be produced by a long-lived engine, with reduced activity at later times, or a simultaneous ejection of shells with a distribution of Lorentz factors (Zhang et al., 2006). In the first case the activity of the central engine $L(t)$ can be described with a power-law dependence with time, i.e. $L(t) = L_0(t/t_\mathrm{b})^{-q}$, with a luminosity of the central engine L_0 at t_b and a typical value of $q \sim 1/2$. A longer lasting central engine is generally related to late accretion onto a central black hole (MacFadyen et al., 2001) or the spin down of a millisecond pulsar (Dai & Lu, 1998). The second case is described by a spread of Lorentz factors of the initial ejected mass. The dependency of amount of ejected mass M on its Lorentz factor is often described with a power law of index s, i.e. $M \propto \Gamma^{-s}$ (Rees & Mészáros, 1998). Slower shells progressively pile up onto the decelerating shock-wave, which mimics the effect of a late central engine activity. Hence q is somewhat degenerate to s, and for $q = 0.5$, $s = 2.6$ would produce similar effects on the light curve (Zhang et al., 2006).

An alternative way of energy injection, independent on the physics of the central engine, is given by a delayed energy transfer into the forward shock. As it takes time to sweep up enough matter for an efficient deceleration of the ejecta, the time scale from the prompt phase to the Blandford-McKee deceleration phase can be as long as several 10^3 seconds (Kobayashi & Zhang, 2007). The shallow decay phase may thus simply represent the time scale of energy transfer to the circumburst medium.

Other mechanisms of producing the shallow decay phase mostly relate to the jet structure. In both, an off-beam or two-component jet model, the shallow decay phase can be explained as a combination of the late tail of the steep decay phase and a delayed rise of the afterglow. In an off-axis scenario, the delayed onset is caused by a rising afterglow emission as more and more of the relativistically beamed jet enters the observer's sight line. In a two-component jet model, the rise is produced by a late deceleration of the lower Γ, broad jet. Hence, both scenarios result in an increasing afterglow emission at early times and consequentially in the shallow decay phase as a superposition of high latitude and increasing afterglow emission.

After the cessation of the energy injection into the forward shock, the afterglow follows what was known earlier and expected from the fireball model: a generic power-law decline eventually followed by a jet break. The discovery of the shallow decay phase however, was unexpected and provides a strong challenge to existing theories. Similar statements can be used for X-ray flares, which appear erratic superimposed onto around 50% of all X-ray afterglow light curves during its entire evolution.

X-ray Flares

Observationally, X-ray flares appear on both, short and long bursts, with a flux increase which can be as large as a factor of 500 on time scales of 100 s (Chincarini et al., 2007, see also Fig. 1.11). The rise and decay index are very steep, and depending on the time of reference can reach values of 7 and above. After the end of the flare, the flux level drops to the extrapolation of the previously established afterglow decline. Furthermore, flares show strong spectral hard-to-soft evolution throughout rise and decay, suggesting a different emission than the generic forward shock afterglow

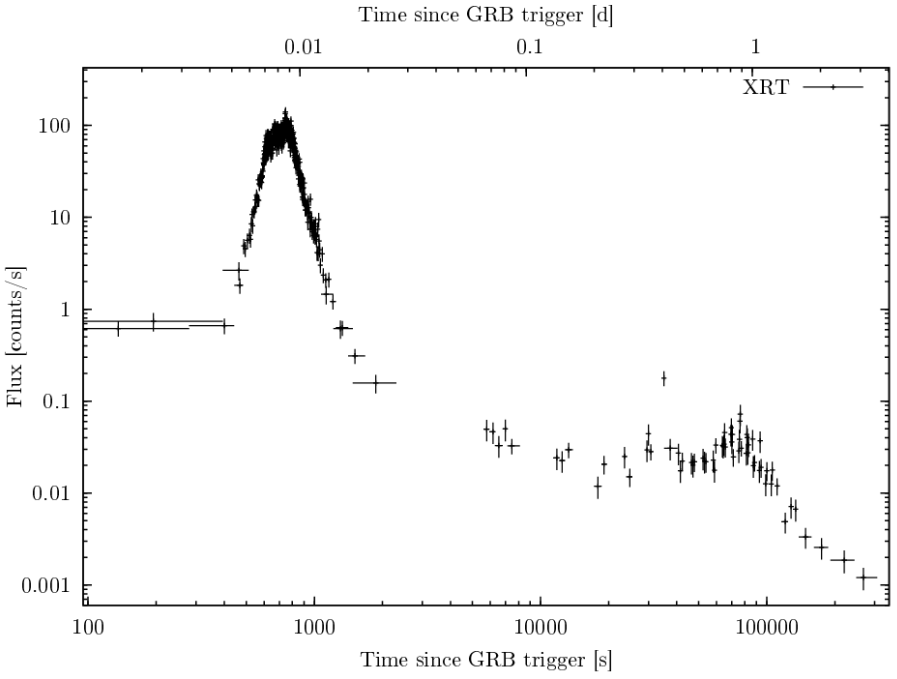

Figure 1.11 The remarkable light curve of the X-ray afterglow of GRB 050502B as the most dramatic example of X-ray flaring activity. Within few hundred seconds, the X-ray flux increases about a factor of 500, and drops back to the initial niveau ~ 400 s later. In addition to the first early flare, which peaks at 700 s, there is evidence for late flaring at around 80 ks.

(Falcone et al., 2007). One of the most dramatic examples is the flare of GRB 050502B (Fig. 1.11), where the flare contains more energy than the prompt emission itself (e.g., Burrows et al., 2005a; Falcone et al., 2006).

Previously, different models have been invoked to explain variability in an afterglow light curve. These models include inhomogeneities in the circumburst medium or the angular distribution of energy in the forward shock (patchy shells) or late energy injection, but all have difficulties explaining the strong variability of flares on short time scales (Ioka et al., 2005). In addition, they cannot account for the strong spectral evolution which is observed in all flares where a detailed spectral analysis is possible. The X-ray spectrum hardens during flares, and is no longer well fitted by a simple power law as typical for afterglow emission. In fact, a flare spectrum is better represented using a Band function peaking in the few keV energy range, and together with the highly variable light curve much more resembles what is observed during the prompt phase, but at lower energies (Butler & Kocevski, 2007; Krühler et al., 2009).

Given the above observational constraints, and the phenomenological similarity to the prompt phase, it is very likely that the X-rays flares are caused by similar processes as the prompt phase, i.e. late central engine activity (e.g., Falcone et al., 2006). This might result in either a late ejection of discrete shells with varying Γ, and their collision produces the X-ray flares, or late injection of energy from Poynting flux dominated outflows, where the dissipation of the magnetic fields causes the observed emission (Zhang et al., 2006).

The fact that flares appear on both, long and short duration bursts hints on a physical origin

related to a common stage of the different progenitors (see Section 1.3). In both cases, the initial source of energy is the infall of matter from an accretion disk onto a newly formed compact object. Due to gravitational instabilities, the accretion disk might fragment, in particular at the outer regions of the disk (Perna et al., 2006). These fragments would be accreted onto the black hole on longer time scales up to days, providing new fuel to the central engine. The energy output which is observed in forms of X-ray flares is then dominated by the mass supply and the accretion rate. For further discussion about X-ray flares and their optical counterparts, see Chapter 4.

1.2.2 The Early Optical Afterglow

In contrast to the evidence of a generic X-ray afterglow light curve, the evolution of optical afterglows shows large diversity during its early phase. This may be partly the result of an observational bias. While the XRT detects an afterglow for essentially all GRBs, the efficiency of UVOT and ground-based, small aperture sized, robotic telescopes limits the information that can be obtained for the early optical afterglow to around 1/3 of all detected GRBs (Roming et al., 2009).

Theoretically, the early optical afterglow is thought to be a superposition of the reverse shock (RS) traveling into the ejecta and the forward shock (FS) propagating into the circumburst medium (e.g., Zhang et al., 2003a). While the FS is expected to be long-lasting and the source of the late afterglow emission, the RS is thought to be brief, and appearing around the typical deceleration time. A RS can be easily identified in the light curve as it should produce a characteristic signature of a bright optical flash declining with $F_\nu(t) \propto t^{-2}$ (Nakar & Piran, 2004).

Probably the best studied examples of early afterglows are GRBs 990123 (Akerlof et al., 1999), 041219A (Vestrand et al., 2005; Blake et al., 2005) and 080319B (Racusin et al., 2008; Bloom et al., 2009). While there seems to be a correlation between prompt γ-rays and early optical photons for GRB 041219A, and the optical flash is interpreted as the low energy tail of the Band function from the prompt emission, this correlation is absent for GRB 990123 (see Fig. 1.12). Its optical flash is rather interpreted as the signature of a reverse shock component. The extremely bright optical afterglow of GRB 080319B finally showed both components before the generic afterglow forward shock: correlated optical and γ-ray emission and a reverse shock contribution. It must be noted though, that in this case the optical emission is magnitudes brighter than expected from a simple extrapolation of the γ-ray spectrum. Different types of emission mechanisms must be responsible for the different photons, where physically reasonable ones are synchrotron emission for the optical bands, and synchrotron self-Compton for the prompt γ-rays (Racusin et al., 2008), but see Piran et al. (2009).

However, only a minor fraction of all well-localized bursts show either of the two effects (Roming et al., 2006). While the spectral shape of the prompt emission and its extrapolation to the optical bands naturally provide a convincing argument for the (non)-detection of correlated optical emission, it is not immediately clear why some bursts do have prominent reverse shocks while the majority does not (Roming et al., 2006).

The relative luminosities in the optical band between FS and RS is given by the degree of magnetization of the outflow, the relative energies between the two components and whether the

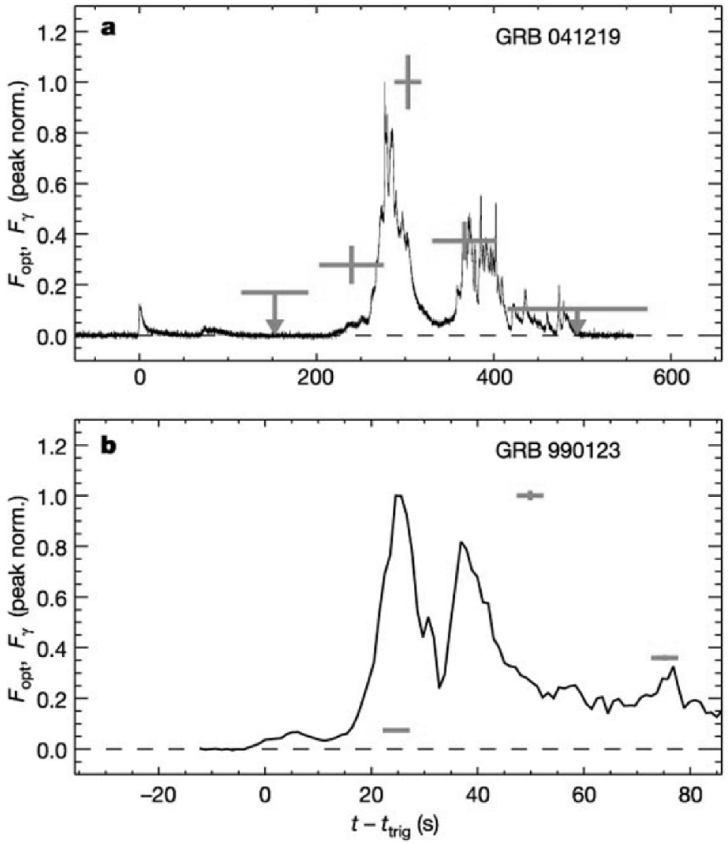

Figure 1.12 Early optical detections for GRB 041219 and GRB 990123. While there seems to be a correlation between γ-rays and optical photons in the case of GRB 041219, this correlation is absent for GRB 990123. For details about the physical implication, please see text. The figure is adapted from Vestrand et al. (2005).

RS is relativistic or Newtonian. In particular, only when the RS is highly relativistic, most of the emission is released in the optical bands. If the conditions are such, that the RS is only mildly relativistic or Newtonian, the typical emission frequency shifts towards, but not reaching the radio band (Nakar & Piran, 2004). Furthermore, the RS might be completely absent if the ejecta are totally or not at all magnetized (Zhang & Kobayashi, 2005). Consequently, the specific conditions in the ejecta, which are dependent on the exact type of progenitor, are expected to populate a large region of different physical properties and only in the minor fraction the degree of baryon loading, circumburst medium density and magnetization supports the formation of a prominent RS emitting in the optical wavelength range. Only in these cases, the luminosity released in the RS is compatible to the FS and fast-slewing, small robotic telescopes are able to detect a characteristic RS signature in the optical afterglow light curve.

1.2.3 Chromatic Breaks

The previously discussed breaks due to the angular distribution of the shock wave's kinetic energy (Section 1.1.3) and the cessation of an energy injection episode (Section 1.2.1) are achromatic by definition, and their signature should appear in all energy bands. However, with the extended coverage with X-ray and optical data in the *Swift* era, a significant fraction of bursts has light-curve breaks which are either only present in one band or not simultaneous as shown in Fig. 1.13. These chromatic breaks are in strong contrast to the expectations for an energy injection or jet break (Panaitescu et al., 2006a).

Furthermore, these breaks lack spectral evolution in the X-ray band, suggesting that the passage of the cooling frequency ν_c is not responsible for these kind of light-curve morphologies. In order to account for chromatic breaks different new models have been proposed, which either imply severe modifications of the standard model, or completely abandon the idea that the afterglow is caused by a forward shock propagating into the circumburst media. In the earlier case, a chromatic break requires a temporal evolution of the microphysical parameters ϵ_B and ϵ_e (Panaitescu, 2006). There is however, no obvious physical reason for varying conditions in the shock-wave, which might indicate that in the case of chromatic breaks the afterglow emission in the optical bands and X-rays arise from different outflows or regions in the ejecta (Panaitescu et al., 2006a). A more controversial explanation has been proposed by Genet et al. (2007), where the X-ray afterglow has an additional reverse shock contribution even at late times, which does not strongly affect the optical bands. This implies that the energy must only be transferred to a very small electron population. Under very specific conditions, in particular a very low Γ of the material which is ejected at late stages of central engine activity, the X-ray afterglow might be explained by a long lasting reverse shock component. There is, however, still no consensus, how to interpret chromatic breaks and all proposed models need further investigation in the light of an increasing sample of well monitored multi-wavelength afterglow light curves.

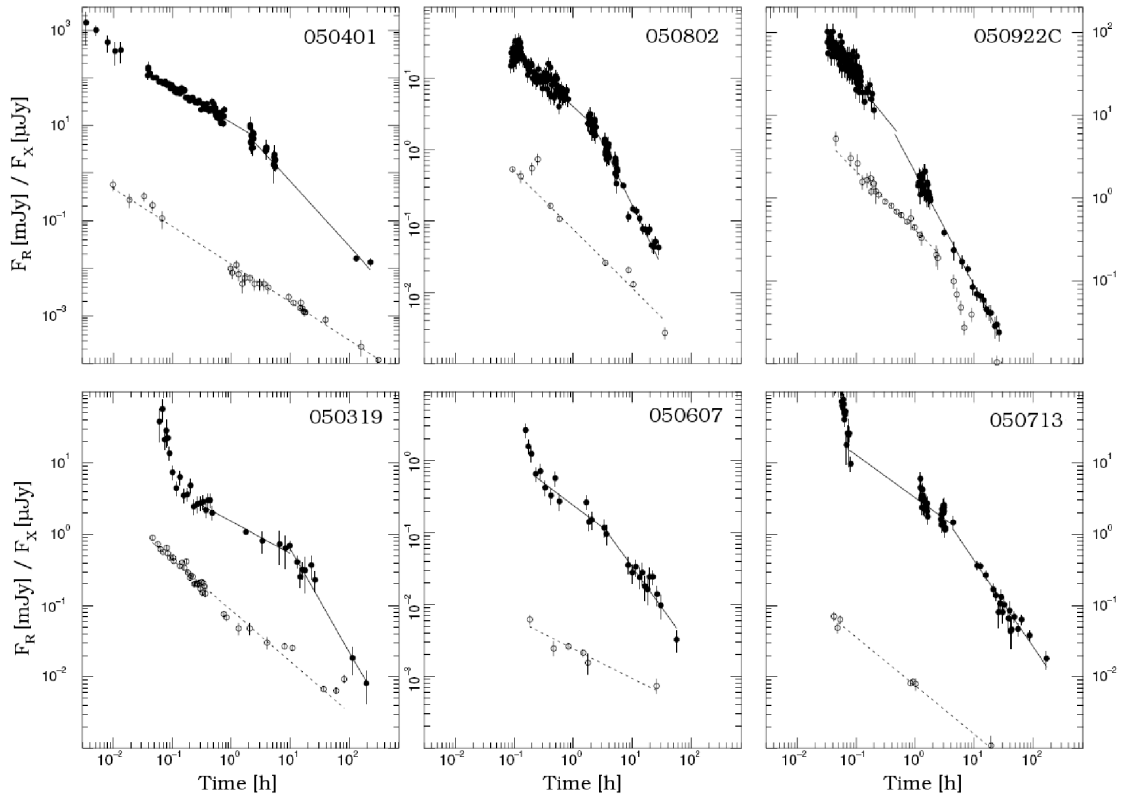

Figure 1.13 A sample of *Swift* bursts with chromatic breaks. Shown are X-ray data in black and R band optical data in open circles. The data are fitted by a single or broken power law (dashed and solid lines). The apparent break is either absent in one of the X-ray or optical bands, or not simultaneous. Adapted from Panaitescu et al. (2006a).

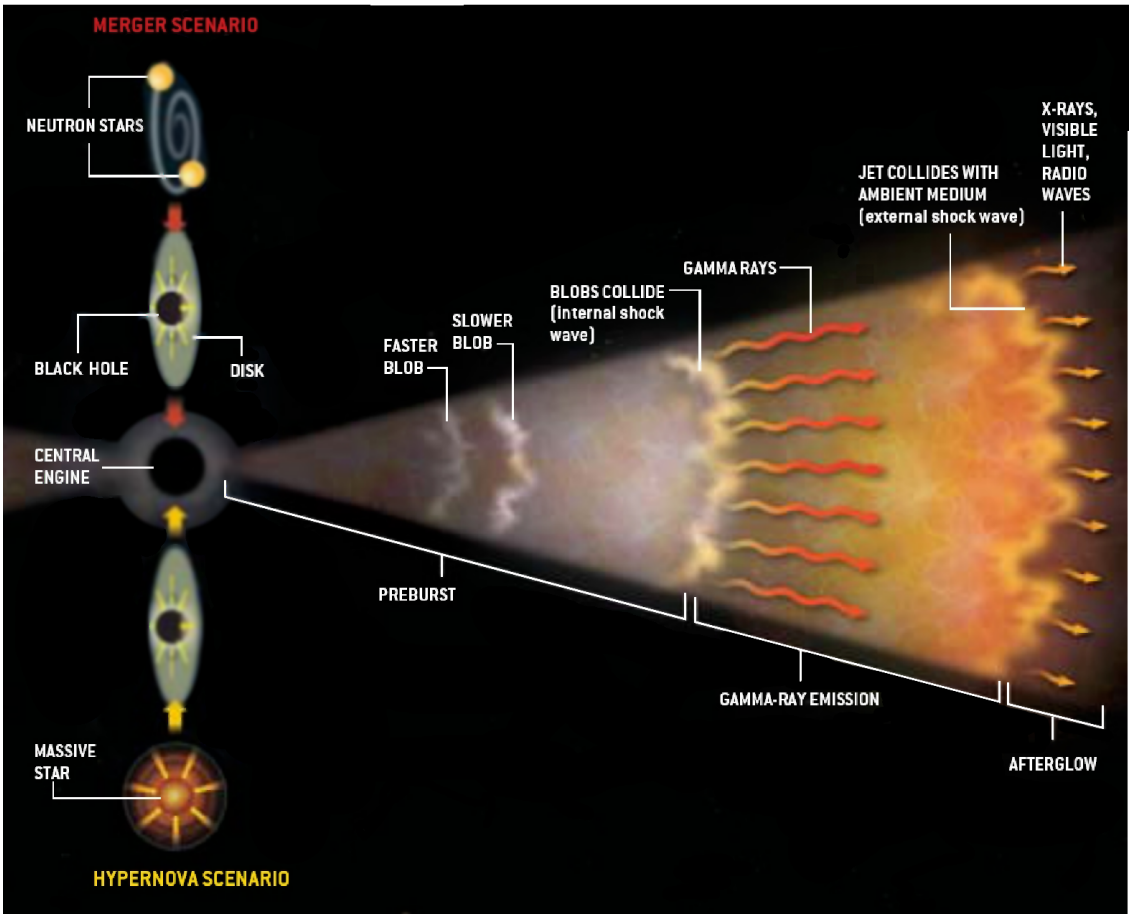

Figure 1.14 Illustration of the two most popular GRB progenitor models and the internal - external shock scenario. The formation of a GRB could begin either with the merger of two neutron stars or with the collapse of a fast rotating massive star. While the earlier scenario is thought to result in a short GRB, there is firm evidence that long GRBs are caused by the latter one. Both of these events create a black hole with a rotating disk of material around it. The black hole - accretion disk system launches a highly relativistic jet along the polar axis of the system. Internal shocks between shells of different velocity produce the GRB, and external shocks with the circumburst medium the afterglow. Adapted from Gehrels et al. (2007).

1.3 Progenitor Models

As discussed in the previous section, a physically reasonable progenitor model must be able to account for a huge energy release in photons of $10^{50} - 10^{52}$ erg on very short time scales, beamed emission with opening angles of 1° to 20° and ultra-relativistic outflows with $\Gamma_0 > 100$. This all strongly suggests the role of newborn compact objects with high angular momentum and an accretion disk as central engine. One of the key questions is then, how to form these accretion systems from stars or binaries at the end of their lifetime. A schematic view of the two most popular progenitor models for long and short bursts is shown in Fig. 1.14 and discussed below.

1.3.1 The Collapsar Model

A collapsar is defined as a very massive, fast-rotating Wolf-Rayet star, which iron core collapses directly to a black hole at the final stage of its stellar evolution (Woosley, 1993). The accretion disk formed around the newborn black hole has typical masses of several tenths of a solar mass, and is fed by the collapse of the outer regions of the progenitor star on time scales of several ten to hundred seconds. A fireball is created by neutrino annihilation above the polar axes, just providing the right amount of energy necessary for GRBs (Woosley, 1993). One crucial stage in the evolution of the progenitor is the loss of its hydrogen and possibly helium envelope due to stellar winds (MacFadyen & Woosley, 1999), which strongly relates the collapsar model to type Ic supernova explosions. A fast rotation is also necessary to achieve a matter free region along the polar axis, which then supports the formation of a jet and an expanding blastwave (e.g., Fryer et al., 1999). The jet is focused by density and pressure gradients, and naturally maintains a collimation of the order of 10° in these simulations (MacFadyen & Woosley, 1999).

Further simulations (e.g., Aloy et al., 2000; MacFadyen et al., 2001; Zhang et al., 2003b, 2004), studied the subsequent evolution after the jet is formed and its breakout through the stellar atmosphere (Fig. 1.15). These simulations predict a further collimation and sporadic decelerations and mixing of the flow along its edges with the stationary stellar material. These variations in the baryonic load lead to different velocities in different regions of the jet - a crucial condition to form internal shocks. Furthermore, a small amount of material is significantly decelerated because of friction and escapes at large angles. The observed morphology and energetics of GRBs are thus strongly dependent on the viewing angle of the observer. Hence, these simulations support a universal model, where the observed spread in GRB prompt emission spectra, i.e. a varying $E_{\rm peak}$ of the Band function between several keV to MeV, can be attributed to different offsets of the observer with respect to the jet's symmetry axis.

By now, there is strong observational evidence through observations of optical spectra which links long GRBs to the death of massive stars. One of the most convincing ones is the GRB-Supernova (SN) connection. In the error box of GRB 980425 (Galama et al., 1998), simultaneous within a day, a nearby SN was located (SN1998bw), which had remarkable brightness. Although the chance coincidence was very low ($\sim 10^{-4}$), the missing afterglow signature and extremely low energy emitted in γ-rays of order 10^{48} erg raised questions whether this might not be a very unusual type of GRB. The textbook example, which unambiguously connected GRBs to type Ic SNe was GRB 030329, i.e. SN 2003dh (Hjorth et al., 2003; Stanek et al., 2003) at a redshift of $z = 0.1685$ (Greiner et al., 2003b). Here, the typical afterglow spectrum of a power-law continuum evolves towards a spectrum very similar to SN1998bw as the relative brightness of afterglow and SN component vary. This provided direct spectroscopic evidence of an emerging SN at later times. Further evidence supporting the collapsar model comes from light-curve modelling of a larger sample of pre-*Swift* afterglows. The signature of an underlying SN is clearly detected in the afterglow of nearby ($z<0.7$) GRBs as an extra emission component at later times, superimposed to the typical afterglow power-law decay (Zeh et al., 2004).

However, difficulties remain, especially in the light of the two recent GRBs 060505 and 060614 (Fynbo et al., 2006; Gal-Yam et al., 2006; Gehrels et al., 2006; McBreen et al., 2008). Located

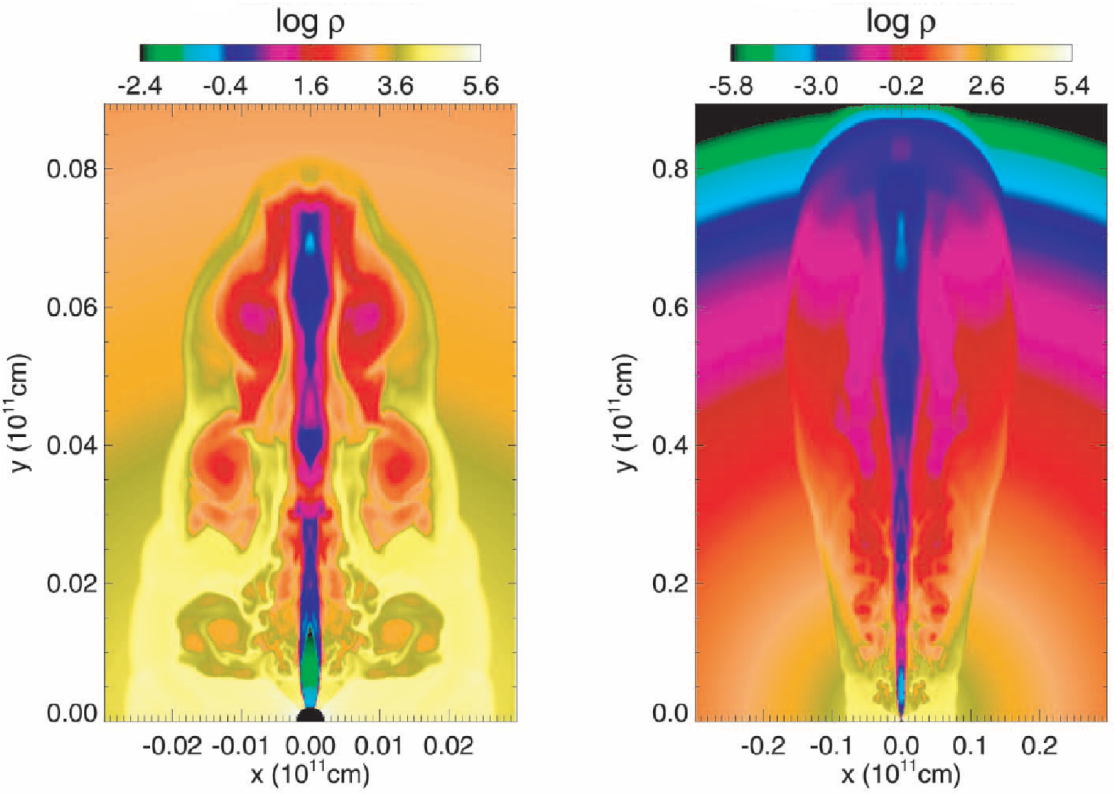

Figure 1.15 Propagation of the jet in the local rest-frame through the stellar atmosphere. Screenshots of numerical calculation in the collapsar model at 2 s and 7 s after the jet is formed are shown. In the left image only the central region of the star with a radius $y = 0.8 \times 10^{10}$ cm is shown. From Zhang et al. (2003b).

at redshift 0.089 and 0.125, their underlying SN signature would have been detected if present at similar level as observed for previous GRBs. Deep optical observations suggest that the SN component for these bursts must have been several hundred times fainter than SN1998bw, and fainter than any type Ic SN ever observed (Richardson et al., 2006). These two bursts represent a significant fraction of nearby ($z < 0.2$) *Swift* GRBs, so that the total fraction of supernova-faint bursts is also expected to be substantial. The luminosity of a SN is related to the amount of synthesized radioactive ^{56}Ni, which needs to be smaller than $1/100\ M_{\odot}$ for the SN non-detections in GRBs 060505 and 060614.

A possible explanation for a missing or very sub luminous SN might be the failed supernovae scenario (Woosley, 1993), where the black hole is not formed directly after the collapse, but only delayed due to fall-back onto the proto-compact object (Fryer et al., 2006). In this case the SN would produce a much lesser amount of ^{56}Ni and its light curve is no longer dominated by its radioactive decay, but rather by the energy deposited in the SN shock. These calculations suggest, that a fall-back GRB might be responsible for the apparent lack of associated SNe in some GRBs (Fryer et al., 2007).

1.3.2 The Merger Scenario

While there is strong evidence linking long bursts to the death of massive stars and the collapsar model, the situation is somewhat different for short bursts. Typically short bursts are less energetic, nearby ($z \lesssim 1$) and their afterglows are orders of magnitudes fainter than for long bursts (e.g., Fox et al., 2005; Levan et al., 2006; Nakar, 2007). A direct spectroscopic measurement of the redshift of a short burst afterglow is thus observationally very difficult, and redshifts for short bursts are generally obtained via host galaxy associations. Contrary to the hosts of long bursts, which are most commonly blue, star-forming, small galaxies (e.g., Le Floc'h et al., 2003; Savaglio et al., 2009), the morphology of short duration burst hosts is diverse (e.g., Berger et al., 2007; Berger, 2009). A significant fraction of these hosts are evolved elliptical galaxies with old stellar populations. Therefore, the most frequently discussed model for the progenitor of short bursts is a merger of two compact objects, either a neutron star - neutron star or neutron star - black hole binary, schematically shown in Fig 1.14. This model is supported by the lack of SN features in the light curves of short burst afterglows. Similar to the collapsar model, a spinning black hole with an accretion disk is also formed in a binary merger, representing a large reservoir of gravitational energy. Naturally, there is a distinct baryon free region along the spin axis of the merging binary. However, the small number of well sampled afterglow light curves and the observational bias in the host galaxies towards brighter, and thus more nearby hosts, makes a distinct identification of the progenitor types for short bursts impossible at the current stage. Although binary mergers have the potential of explaining the short burst phenomenon, more data is needed to securely associate short bursts with mergers. One interesting possibility might be the detection of gravitational waves contemporaneous with a short burst. Berger et al. (2007), for example, estimated the detection rate of the signature of a binary merger for the upcoming generation of gravitational wave detectors to 2-6 per year.

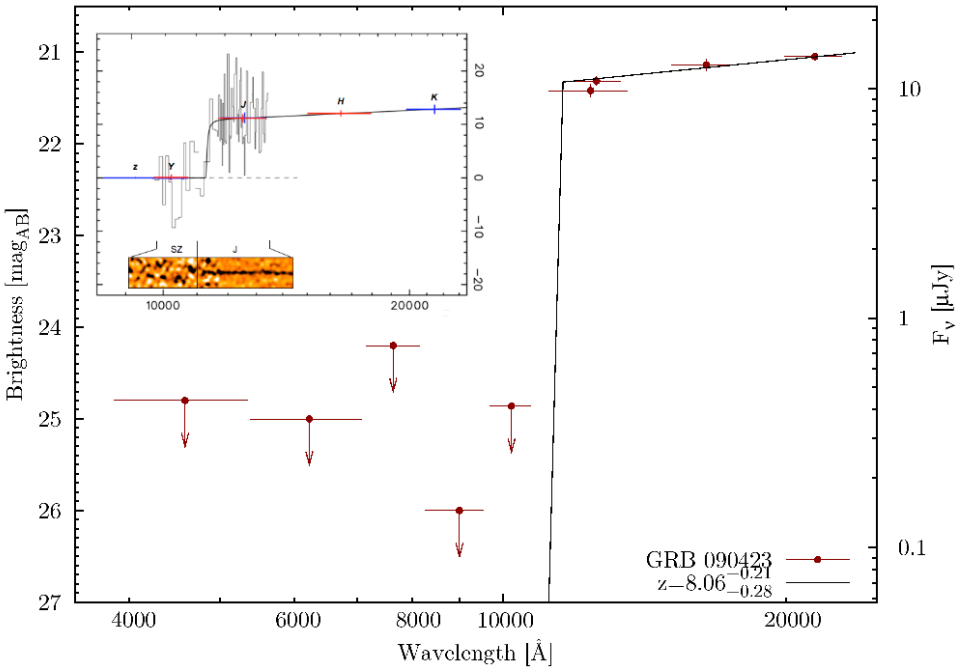

Figure 1.16 Photometric ($8.06^{+0.21}_{-0.28}$) and spectroscopic ($8.26^{+0.07}_{-0.08}$) redshift of GRB 090423. The photometric data has been obtained by GROND, VLT/HAWKI and the Gemini South telescope, analyzed and modeled by the tools described in Chapter 2. The inset shows the spectroscopic observations performed with ISAAC at the VLT, fully consistent with the photometric data. Adapted from Tanvir et al. (2009).

1.4 GRBs as Tools

Two recent discoveries of GRBs at very high redshift, GRB 080913 at redshift 6.7 (Greiner et al., 2009b) and GRB 090423 at redshift 8.3 (see Fig. 1.16, and also Tanvir et al. (2009)), clearly demonstrate the potential of GRBs as cosmological probes (see also Chapters 2 and 3). Theoretically, *Swift* is able to detect GRBs at redshift of 10 and beyond (see Fig. 1.17), which given only modest brightness can be followed up and detected by state of the art instruments as GROND (see Fig. 1.16, Chapter 2, also Greiner et al. (2009b)).

Although the direct cosmological use of GRBs as standard candles (e.g., Ghirlanda et al., 2004; Firmani et al., 2005), analog to SN Ia explosions is still highly debated (e.g., Nakar & Piran, 2005; Butler et al., 2007), the enormous energy release and brightness of the afterglow, which can outshine even the brightest quasar by a factor of 10^5 at a similar redshift, makes GRBs ideal light sources to study the very early Universe (Bromm & Loeb, 2002). In the very most pragmatic way, GRBs are considered just as a source of radiation, which is then used to investigate the metal enrichment of the Universe and the epoch of reionization (Lamb & Reichart, 2000; Loeb & Barkana, 2001). Furthermore, using the association of GRBs with the death of massive stars, the star formation history of the Universe can be directly constrained out to very high redshifts as shown in Fig. 1.18 (Yüksel et al., 2008). Although number statistics are still low, GRBs already provide significant constraints on the star formation rate (SFR) at redshifts above $z \sim 6$, a region which is not easily accessible with other sources so far. The SFR rate as derived with GRBs can exceed the critical

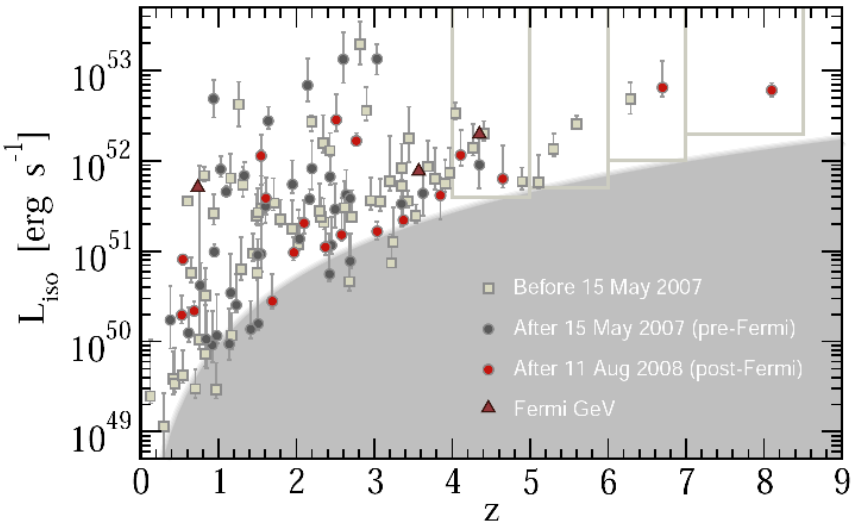

Figure 1.17 The luminosity - redshift distribution of 119 *Swift* bursts determined by Butler et al. (2007). The shaded region approximates an effective threshold for detections with the Burst Alert Telescope (BAT) onboard *Swift*, and clearly shows that the somewhat brighter bursts can be detected by BAT to redshifts of above 9. Demarcated in grey boxes are the GRB sub sample used to estimate the cosmic star formation rate in Fig. 1.18. Adapted from Kistler et al. (2009).

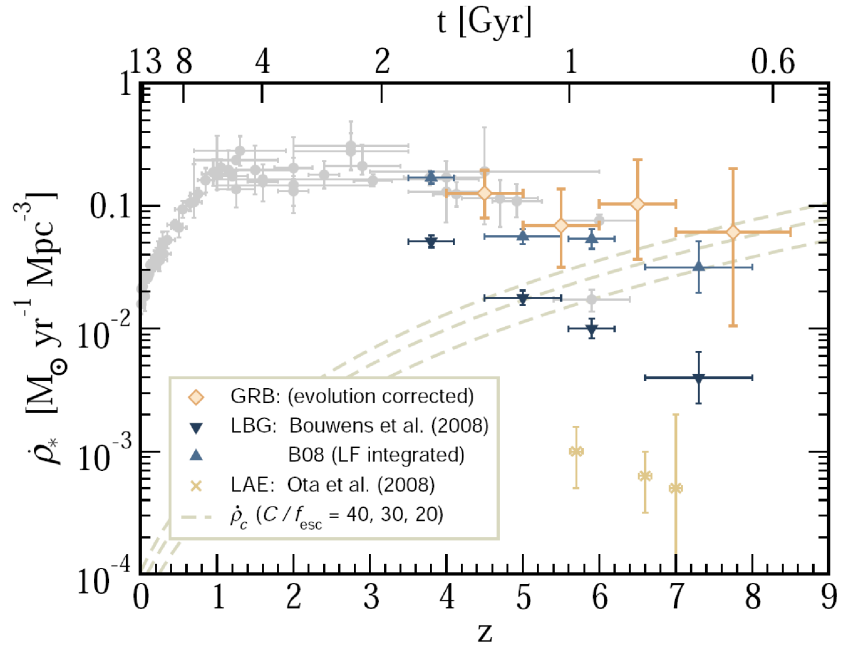

Figure 1.18 The cosmic star formation rate density $\dot{\rho}_*$ in solar mass per year and volume as derived with GRBs and other methods in dependence on the redshift (lower x axis) and the age of the Universe (upper x axis) assuming concordance cosmology. After correcting for evolutionary effects, straight forward number counts of GRBs can be used to measure the SFR. Shown are the data compiled in Hopkins & Beacom (2006) in grey light circles, Lyman Break Galaxies (LBG) from Bouwens et al. (2008) in blue triangles, and Lyman-α emitters (LAE) from Ota et al. (2008). In dashed lines the critical SFR $\dot{\rho}_c$ which is needed to balance recombination. $\dot{\rho}_c$ is depending on the clumpiness C of the intergalactic medium (IGM) and the escape fraction of photons in their host galaxy $f_{\rm esc}$. Adapted from Kistler et al. (2009).

SFR $\dot{\rho}_c$ which is needed to balance the recombination of ionized Hydrogen even at redshift above 8. Thus, it seems plausible that the level of star formation was high enough even at this very early times to reionize the Universe (Kistler et al., 2009).

Apart from their intrinsic brightness, GRBs have several advantages over Quasars as probes of the early Universe. As the source of the explosion is stellar, GRBs do not disturb or ionize the intergalactic medium (IGM). After the afterglow had faded, the host galaxies of high-redshift GRBs can be observed in their characteristic physical state. GRBs thus serve as signposts of the very first or even proto galaxies, which will be observationally accessible to the upcoming telescopes of the 30-40 m class or the James Webb Space Telescope, the successor of HST.

In addition, their spectrum is a very simple power law, making fast photometric redshifts reliable, and a detailed, unambiguous investigation of hydrogen and metal absorption in their spectra possible. However, the transient nature of GRBs and their afterglows require rapid identification and follow-up observations, preferentially within the first hours post burst. It is from primary importance to measure the spectral energy distribution of the afterglow in the near-infrared regime, as any optical follow-up is determined to miss the afterglow of GRBs above redshifts of $z \sim 7$.

Chapter 2

The GROND Instrument

The primary goal of the Gamma-Ray Burst Optical/Near-infrared Detector (GROND, Greiner et al., 2007b, 2008) is to identify GRB afterglows and measure their photometric redshift as rapid after the trigger as possible. Therefore, the instrument is designed for simultaneous imaging in 7 different photometric bands: four optical CCDs in filters $g'r'i'z'$ and three near-infrared (NIR) detectors in JHK_S. These filters cover the wavelength range from 380 nm to 2400 nm, and GROND can thus identify GRB afterglows up to $z \sim 20$ and measure their redshifts in a range from $z \sim 3$ to $z \sim 13$. A schematic view of the optical layout is shown in Fig. 2.1.

GROND was designed and built by the Max-Planck-Institut für extraterrestrische Physik (MPE) in collaboration with the Thüringer Landessternwarte Tautenburg (TLS) and is permanently mounted at the 2.2 m MPG/ESO Ritchey-Cretien telescope at LaSilla observatory, Chile and operational since spring 2007. A movable mirror (M3) reflects light coming from the telescope's primary (M1) and secondary (M2) mirror towards the GROND vessel in a Coudé-like focus. Both the instrument and the telescope are controlled semi-robotically, which yields a typical reaction time of $200 - 400$ s to GRB triggers. Most of the delay is due to the limited slewing speed of the conventional telescope and dome. The medium-sized aperture of the telescope and relatively fast response is crucial for an effective observation of GRB afterglows. A typical afterglow fades by ≈ 3 magnitudes during its first 10 minutes after the trigger, and another 3 magnitudes in the following two hours. The unique optical design with NIR coverage, medium-sized telescope aperture and rapid response yields unprecedented detection efficiency for GRB afterglows. If the visibility of the optical transient associated with a GRB is such, that GROND can observe within 10 minutes, an afterglow is detected with a probability in the high 90% region (cp. other robotic telescopes in the $\sim 30 - 80\%$ region e.g., Roming et al., 2009; Cenko et al., 2009; Rykoff et al., 2009; Klotz et al., 2009), or in 62% of all ~ 100 bursts observed with GROND until June 2009. These numbers are significantly higher than any GRB follow up program has reported so far. A subset of GROND afterglow light curves is shown in Fig. 2.2.

Utilizing the high detection rate of the early afterglow observations, its now possible for the first time to address open questions in GRB physics with a sample which is unbiased in intrinsic brightness, extinction and redshift. A complete sample will allow to probe the rates of highly

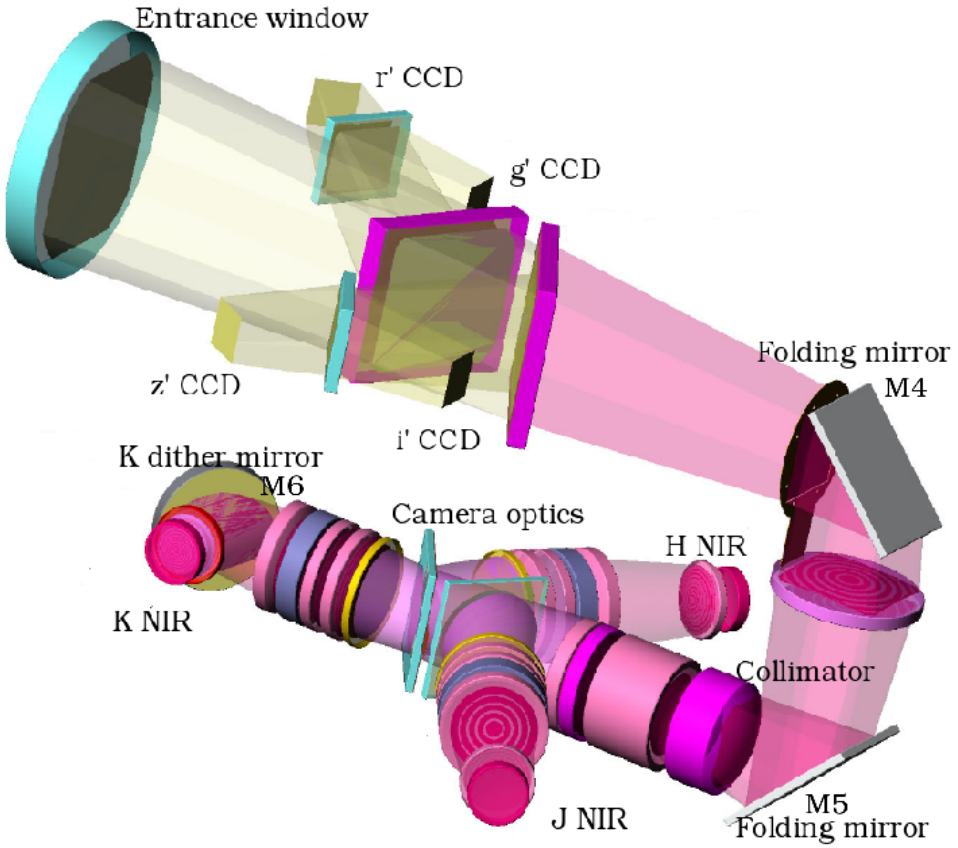

Figure 2.1 Schematic optical layout of the GROND instrument. The light is split by a total of six dichroics into the seven different channels. Each single detector is optimized in efficiency for its respective wavelength range. The detector chips are conventional 2k × 2k CCDs in $g'r'i'z'$ and 1k × 1k Hawaii chips in the NIR. The field of view in the optical channels is $5.4' \times 5.4'$. To obtain a sufficiently large field of view in the NIR, the telescope's plate scale is enlarged by a focal reducer. The combination of 5 lens collimator and 6 lens camera ensures a field of view of $10' \times 10'$. Adapted from Greiner et al. (2008).

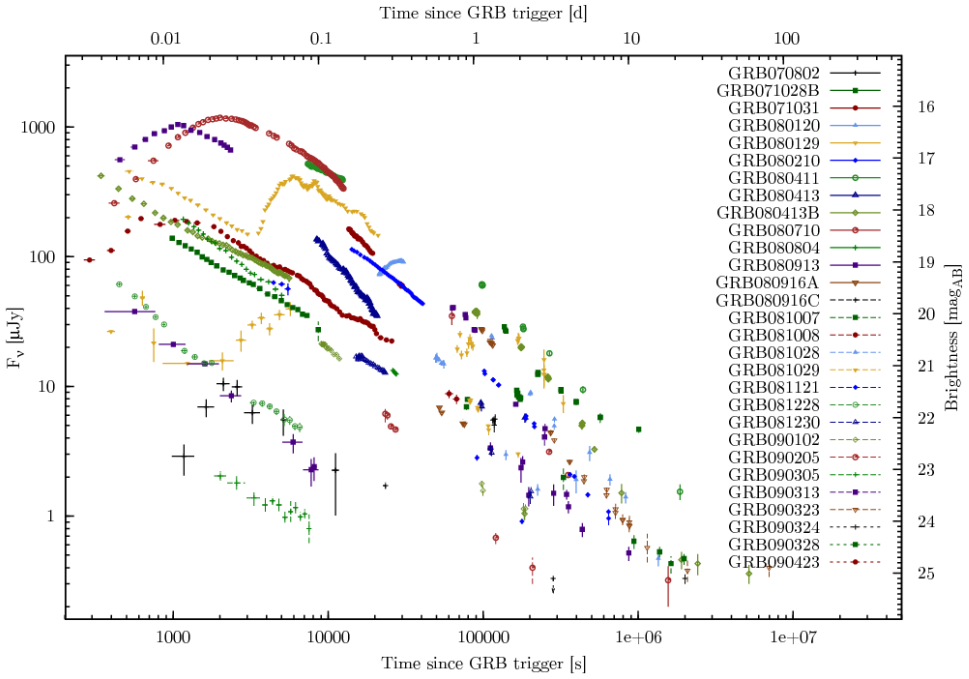

Figure 2.2 Subset of r'-band light curves of GRB afterglows as observed with GROND. For cases where the redshift was $z \geq 5$ (GRBs 080913 and 090423) the J-band light curve is shown. This sample clearly shows the variety and variability of early afterglow light curves. While conventional instruments provide spectral information only on a longer time scale due to filter cycling, GROND measures the spectral energy distribution (SED) in a broad range at each point of each single light curve. Effects of a changing spectrum or intrinsic extinction can thus be measured with high confidence, independent on the light curve morphology.

extincted, highly redshifted and intrinsically faint GRB afterglows, eventually reaching stringent conclusion about the nature of so-called dark bursts (Groot et al., 1998), where the ratio of X-ray to optical flux indicates a suppression of the optical afterglow.

Because of its simultaneous imaging, GROND has the key advantage that it obtains information about the spectral energy distribution at each point during the evolution of the afterglow. In particular in the early stages of optical afterglows, effects of a changing spectrum or a highly variable light curve can be unambiguously disentangled, which has been proven to be crucial in the interpretation of the light curves of, e.g., GRB 071031 (Krühler et al., 2009) or GRB 080129 (Greiner et al., 2009a).

2.1 Filter System

GROND uses dichroics, which transmit the lower- and reflect the higher-energy photons to split the incoming light into its seven channels. To define the final shape of the total response curve of each wavelength band in GROND, there is also an additional filter which cuts off regions of high sky background in the NIR and reduces spurious reflections from the backside of the dichroics. Additional optical components in the instrument/telescope system are the aluminum coated M1 and M2 of the 2.2 m telescope, GROND's silver coated M3, M4, M5 and M6 (see Fig. 2.1) and the

focal reduction system in the NIR. Together with the transmission of the entrance window and the quantum efficiency of the detectors, these define the GROND filter bands as shown in Fig. 2.3. The reflection and transmission of all optical components was measured at their operating temperature of 80 K inside the GROND vessel, yielding highly accurate response curves down to systematic errors of typically $2-4\%$. A more detailed description of the filter curves including characteristic filter parameters is given in Krühler (2006).

2.2 GROND Observation Scheme

The bright and variable NIR sky background limits the individual exposure times in the NIR to around 10 s. Hence, a dithering pattern on the sky must be performed for an efficient sky subtraction. These ditherings should be faster than the typical time scale of sky variation which is of the order of several minutes for J, H and K_S. A typical GROND observation thus consists of several observation blocks, each with four, six or eight telescope pointings. These pointings are offset by roughly 10 arcseconds and contain one or several images in the $g'r'i'z'$ channels with a typical integration time between 30 s and six minutes, and a series of 10 s exposures in the NIR. In addition, there is a K_S-band dither mirror, which performs internal dithering in the K_S band to ensure an appropriate dither pattern for this band. The exposures in $g'r'i'z'JHK_S$ are synchronized, so that no band sits idle with as little overhead as possible. The detailed GROND observation scheme is described in Krühler (2006).

2.3 Reduction Software

The mechanical and optical design of a multi-channel imager operating in the optical and NIR regime requires sophisticated observation scheduling and requires an advanced layout of the automated data reduction scheme. In particular, the GROND Pipeline (GP) must be able to deal with both, optical data and NIR frames. The whole code is implemented in *python*[1], utilizing *pyraf*[2], a wrapper for the standard software for astronomical image processing, the *Image Reduction and Analysis Facility* (IRAF, Tody, 1993). In addition, the object oriented *python* language provides the substructure and possibility to utilize spawned processes and fork different tasks to child processes within a single framework. Consequentially, a complete reduction of GROND raw data until final photometry products can be handled in a single program. For a technical description of the GP concepts and basics, see Küpcü-Yoldaş (2006). Based on the existing pipeline layout, a user friendly and stable code for data reduction has been developed in the context of this thesis, which is described in detail below.

[1] http://www.python.org/
[2] http://www.stsci.edu/resources/software_hardware/pyraf

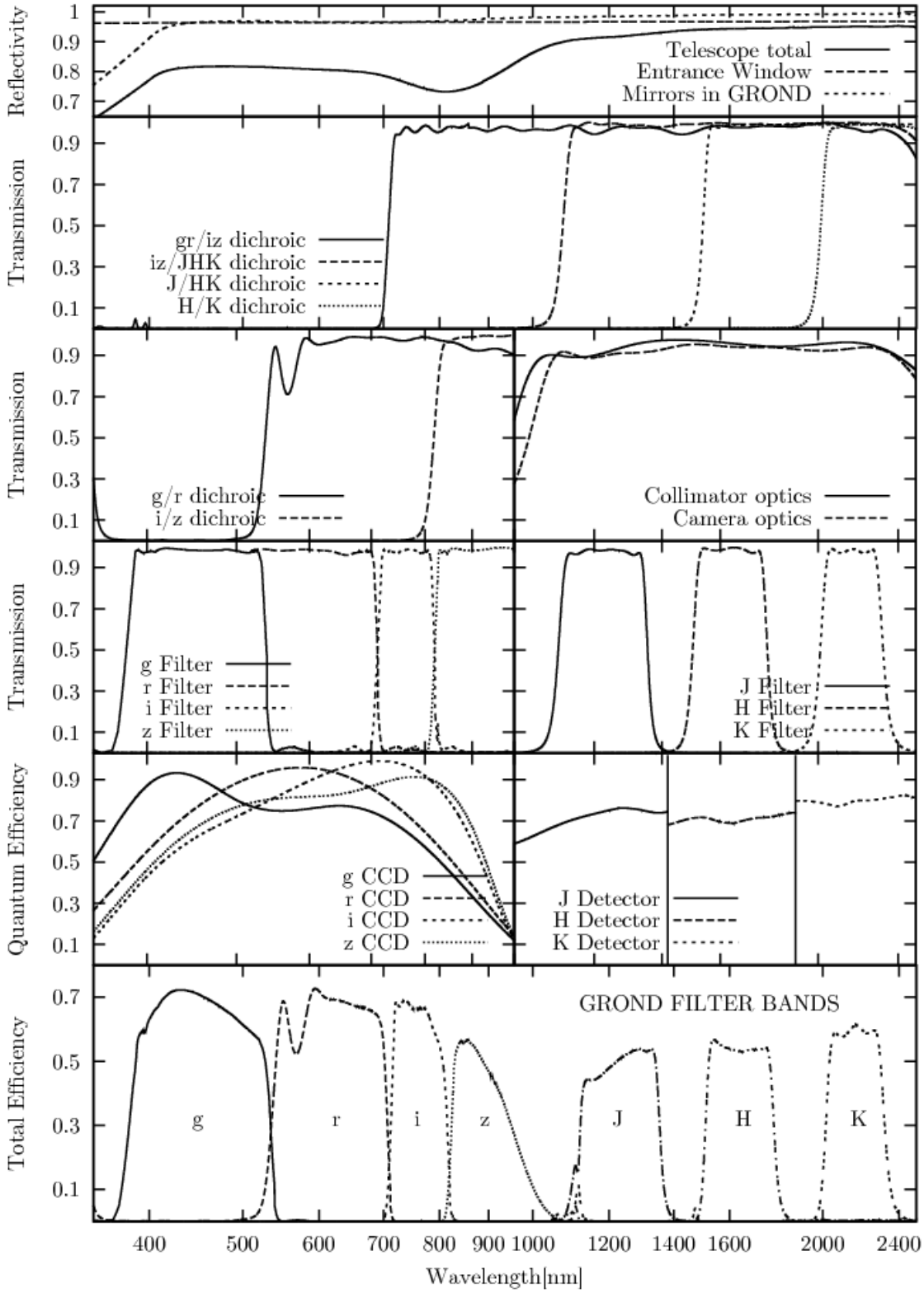

Figure 2.3 Efficiency of the GROND instrument at the 2.2 m telescope: Top panel: telescope and GROND-internal mirrors. Panels 2 and 3 from top: transmission of the dichroics and the NIR lens systems. Panel 4: Transmission of the filters. Panel 5: Detector quantum efficiencies. Bottom panel: Total efficiency in each of the seven GROND bands. All losses are included, except the obstruction of M1 by M2. Except for the telescope (M1, M2) data, all curves represent measured data at their operating temperatures, i.e. all transmission values for the lenses, dichroic and anti-reflection coatings refer to 80 K.

2.3.1 Reduction, Dithering and Sky Subtraction

Although the reduction code is customized and optimized to GROND data, the complete software layout aims on being as generic as feasible, which makes the program also suitable for imaging data from different telescope/instrument combinations. A set of photometric data can thus be analyzed consistently in a single software framework. Starting from raw frames, as they are produced by the instrument, the data-reduction pipeline performs the following tasks which are split into different modules.

`preprocess` **module:** This module performs the necessary steps to extract the single-band image from the raw data. In particular, all four CCD frames come stacked into one multi-extension fits image, while the NIR data from three 1k x 1k detectors are stored in a single 1k x 3k fits image with a single header.

`reduction` **module:** After initial pre- and overscan clipping and bias correction, the image is flatfielded with the most recent master flat. A defringing step is applied when necessary, but only long exposures ($\gtrsim$ 3 min) suffer from detectable fringing in the z' band. NIR data are corrected for the odd/even effect of the Hawaii chips. Optional, there can be a background estimation using either a one-dimensional line-by-line fit, or a two-dimensional plane fit. In particular, if the sky conditions or brightness are changing on a time scale faster than the observations, this step is necessary to obtain adequate results.

`stacking` **module:** The individual 10 s NIR images, which are obtained on the same position of the sky in the NIR channels are combined to obtain a higher signal-to-noise ratio.

`distortion correction` **module:** The stacked images are corrected for the image distortion which is a result of the focal reducer in the NIR channels. The theoretical image distortion depending on the location of the object in the focal plane and the dithering position has been calculated, stored in a database and is applied onto the image.

`dithering` **module:** The sky background estimation and shift-and-add of frames which have been obtained on different telescope dither positions can be done using either IRAF or *jitter*[3], a compilation of NIR data reduction algorithms from the European Southern Observatory (ESO). The offset search is performed using cross-correlation techniques, which are very reliable and result in sub-pixel accuracy of the image registration. To enhance the computation speed an initial guess of the image shift depending on the dither pattern can be provided.

2.3.2 Astrometry and Photometry

The final product of the previous steps, a single image for a single observation block per band is then pushed to the astrometry and photometry task. After source detection, an astrometric solution is derived against automatically parsed USNO-B1 (Monet et al., 2003) and Two Micron All Sky Survey (2MASS, Skrutskie et al., 2006) catalogs or the Sloan Digital Sky Survey (SDSS, Adelman-McCarthy et al., 2008), if available. The full width half maximum (FWHM) of the

[3] http://www.eso.org/projects/dfs/papers/jitter99/

stellar point spread function (PSF) is derived for each image in each band separately by *sextractor* (Bertin & Arnouts, 1996). Final products of a successful analysis include aperture and PSF fitting photometry from *daophot* (Stetson, 1987) of all detected field sources, auxiliary photometry from *sextractor*, calibrated magnitudes against the downloaded catalogs, and the accuracy of the absolute photometry and of the astrometric solution. The brightness of an object is measured in magnitudes (mag) in the AB system (Oke & Gunn, 1983), where the AB magnitude is related to the respective flux density F_ν via (e.g., Fukugita et al., 1996):

$$F_\nu[\mu\mathrm{Jy}] = 10^{(23.9-\mathrm{mag_{AB}})/2.5}$$

2.3.3 Photmetric Accuracy

The native GROND photometric system is based on the SDSS $g'r'i'z'$ and 2MASS JHK_S filters. In most cases, however, the burst field is not covered by the SDSS, which is a photometric and spectroscopic survey of the northern sky. In that case, secondary field stars are calibrated against the primary equatorial SDSS standards, or a nearby SDSS field under photometric conditions. As the filter bands are nearly identical to the Sloan and 2MASS filters, the absolute photometric accuracy reachable with GROND is in the range of 0.03 mag for $g'r'i'z'$ and 0.05 mag for JHK_S. Typical limiting magnitudes in the AB system for a 1 h exposure at zenith, and seeing 1" at new moon are 25.0 (g'), 25.0(r'), 24.3 (i'), 24.0 (z'), 22.9 (J), 22.4 (H) and 21.8 (K_S).

The limiting magnitudes of the NIR channels are strongly dependent on the NIR sky background, which shows large seasonal variations depending on temperature, humidity and sky conditions. Under a bright NIR sky, the JHK_S limiting magnitudes can be up to 1.5 mag higher. A detailed description of the photometric calibration will be given in Clemens (2009, in preparation).

2.4 Light Curve Fitting

One key information about GRB afterglows that can be obtained by continuous monitoring is the dependence of the flux density on time, i.e. $F_\nu(t)$, as shown in Fig. 2.2. Consistent with the expectations from theory (see Section 1.1) and observed in a large sample of light curves (Zeh et al., 2006), the late optical afterglow is typically well described with two power-law segments, smoothly connected at a break time t_{break} and a possible constant host or SN contribution. However, the early afterglow can be highly variable, with early rising components and chromatic flares (see Fig. 2.2 and Chapters 3, 4 and 5). A crucial task is then to model the diversity of early afterglows, which makes it possible to draw conclusions about the GRBs inner engine and the nature of the afterglow, in particular the conditions in the ejecta, the geometry of the outflow and the circumburst medium. Therefore, the constraints on a multi-color light-curve fitting program can be summarized as follows:

Multi Dimensionality: The program should be able to combine various input data obtained in different energy ranges from radio over optical/NIR to X-ray. In particular a typical GROND

afterglow light curve consists of 7 different energy bands from 380 nm to 2400 nm (0.5 eV to 3.2 eV). In most cases this information is complemented with X-ray data in the 0.3 keV to 10 keV range. Best possible constraints from the available data can only be obtained when analyzing the entire data set simultaneously.

Parameter Handling: Model parameters must be able to be frozen, thawed and constrained to specific ranges with upper and/or lower limits.

Model Definition and User Interface: User defined models should be easy to code, and easy to implement for further extension of the light-curve fitting program. The user interface must be easy to learn and (re-)run, and scriptable for automated analysis.

Error Estimation: The code should automatically perform a reliable estimate of the errors attributed to the best-fit parameters.

Speed: The software should be able to obtain results and reliable errors on a typical personal computer in less than a minute, even for large data sets ($>$ 2000 unique measurements) and complex models ($>$ 20 free parameters).

Open Source: The program must not be based on commercial packages which require a license or purchase.

From particular importance is a thorough error analysis, so that observational parameters can be confidentially compared with expectations from theory. The light-curve fitting program which was designed and developed as part of this thesis is based on the *python* interface[4] to the *root*[5] framework (Brun & Rademakers, 1997), which has proven to be stable and reliable in numerous application, preferentially in particle physics, but also astrophysics. Given the stability and reliability of the *root* substructure and an easy readable and expandable code and user interface in *python*, the program then complies with all predefined constraints. In particular, it is able to account for a simultaneous fit with an unlimited set of input data. Each filter band (e.g., the GROND $g'r'i'z'JHK_S$) and/or energy range (optical + X-ray) is linked via shared parameters, while a subset of parameters is exclusively accessible to a subset of the specific input data. The earlier typically include power-law slopes and break times, while the latter describe the overall flux normalization and/or the color change of the afterglow in flares, or in the host dominated regime. All parameters can be tied, thawed, frozen or linked according to the specific needs of the user. Technically, this is performed via a virtual multi-dimensional fit, where the shared parameters represent the first, and all unique parameters the higher dimensions of the fit.

As predefined empirical model functions a number of equations, describing a typical afterglow light curve have been pre-coded. These include (amongst others):

Single Power Law (PL)

$$F_\nu(t) = F_0 \cdot (t/t_0)^{-\alpha}(+H)$$

[4] http://www.scipy.org/PyRoot
[5] http://www.root.cern.ch

with the flux normalization F_0 at fixed t_0 and the power-law slope α and a possible host component H.

Broken Power Law (BRPL)

$$F_\nu(t) = F_0 \cdot \left(\left(\frac{t}{t_b} \right)^{-s\cdot\alpha_1} + \left(\frac{t}{t_b} \right)^{-s\cdot\alpha_2} \right)^{-1/s} (+H)$$

with two power-law slopes α_1 and α_2 smoothly connected at a time $t_{\rm break}$. The smoothness is described by s, where a small $|s|$ is a very smooth break, and a positive s describes a break with $\alpha_1 < \alpha_2$, whereas a negative s stands for $\alpha_1 > \alpha_2$. The time of the break $\rm t_{break}$ is related to $\rm t_b$ via $\rm t_{break}$=$\rm t_b(-\alpha_1/\alpha_2)^{1/(s(\alpha_1-\alpha_2))}$

Double Broken Power Law (DBPL)

$$F^1_\nu(t) = F_0 \cdot \left(\left(\frac{t}{t_{b,1}} \right)^{-s_1\cdot\alpha_1} + \left(\frac{t}{t_{b,1}} \right)^{-s_1\cdot\alpha_2} \right)^{-1/s_1}$$

$$F^2_\nu(t) = F_0 \cdot \left(\left(\frac{t_{b,2}}{t_{b,1}} \right)^{-s_1\cdot\alpha_1} + \left(\frac{t_{b,2}}{t_{b,1}} \right)^{-s_1\cdot\alpha_2} \right)^{-1/s_1} \left(\frac{t}{t_{b,2}} \right)^{\alpha_3}$$

$$F_\nu(t) = \left(F^1_\nu(t)^{-s_2} + F^2_\nu(t)^{-s_2} \right)^{-1/s_2} (+H)$$

with three power-law slopes α_1, α_2, α_3 at two break times $t_{b,1}$, $t_{b,2}$ and two different smoothness parameters s_1, s_2 similar to the broken power law.

Gaussian Flare Components (F)

$$F_\nu(t) = F \cdot \exp\left[-1/2 \cdot \left(\frac{t - t_{\rm mid}}{\sigma_{\rm t}} \right)^2 \right]$$

with time and width of the flare $t_{\rm mid}$ and $\sigma_{\rm t}$ respectively. Flares are generally superimposed to one of the previous model components. The flare color, defined as the ratio between different single band normalizations F can be significantly different than in the standard power-law afterglow as shown in Chapter 4.

Shared parameters are labeled with small letters, and parameters unique for a single band in capital letters. In addition, superpositions of these functions are available, e.g., to account for two-component jets, with or without a host (H) or superimposed flare (F) component. A recent example of the light-curve modelling is shown in Fig. 2.4.

The complete data set is analyzed in the *Minuit* framework (James & Roos, 1975), so that the global χ^2 of all data against the model is minimized. The estimation of the errors on the best-fit parameters are returned in two ways. First, errors from the Hesse-matrix, i.e. the second derivatives of the χ^2 of the model function are calculated. Here χ^2, as in the common case of a least-squares fit, is defined as:

$$\chi^2(\xi) = \sum_{i=1}^{n} \frac{(f(x_i, \xi) - e_i)^2}{\sigma_i^2}$$

where ξ is the vector of the free fit parameters and e_i are the individual measurements with uncertainties σ_i. These are symmetric 1σ errors and take all parameter correlations but not the non-linearities into account. The Hesse-matrix analysis thus results in symmetric errors and in an appropriate error estimation as long as the $\chi^2(\xi)$-function can be approximated as a quadratic function in the local minimum of the parameter space. If the problem is highly non-linear, this procedure will significantly underestimate the errors, and hence a second run of error estimation is performed by default. Here, the algorithm to estimate the parameter error is defined such, that the parameter is varied and the fit function is subsequently minimized with respect to all other variable parameters. Hence, the value of the fit parameter where the $\Delta\chi^2$ represents a 1σ error is obtained numerically with respect to the minimum of all other free parameters. The resulting errors are then generally asymmetric and relatively expensive to calculate, but return a reliable estimate on the parameter errors in all cases.

Finally it must be noted, that even the most sophisticated error analysis strongly relies on a correct determination of the errors attributed to the experiment. While the fit and the best-fit parameters may still be physically reasonable in the case of under- or overestimated measurement errors, the error bars on the fit parameters are certainly not. Special care must thus be taken to account for all statistic and systematic errors in the measurement, and a correct error propagation.

2.5 Spectral Energy Distribution Modelling

Apart from the light-curve information, GROND obtains the spectral energy distribution of the afterglow, i.e. information on $F_\nu(\nu)$ over a large frequency domain. The typical afterglow spectrum is a simple power law which is modified by dust and gas along the sight line towards the GRB. From special interest here is the dust attenuation law, and the absorption of light by neutral hydrogen in the GRB environment bluewards of Lyman-α (Ly-α) at $121.6(1+z)$ nm in the observers frame. The host of GRBs and the circumburst environment is generally gas rich, and thus has a very high neutral hydrogen column density of $N_{\rm H} \sim 10^{21}{\rm cm}^{-2}$ and above. Systems with $\log N_{\rm H} \geq 20.2$ are named Damped Lyman-α Absorbers (DLAs). The afterglow flux is further suppressed by intervening absorbers at redshifts between the bursts and the observer, the so called Lyman-α forest. By modelling the effects of dust and gas along the sight line towards the afterglow, the redshift of the burst, as well as the dust content in its immediate environment can be studied (e.g., Fig. 2.5, or Chapter 3). Above redshifts of $z \sim 3$, the Ly-α edge is well within GROND's sensitivity limits and results in a redshift dependent absorption at the blue side of the afterglow spectrum. Details on the specific software used, the physical effects of gas and dust absorption, and photometric redshifts and their accuracy are given in the following sections.

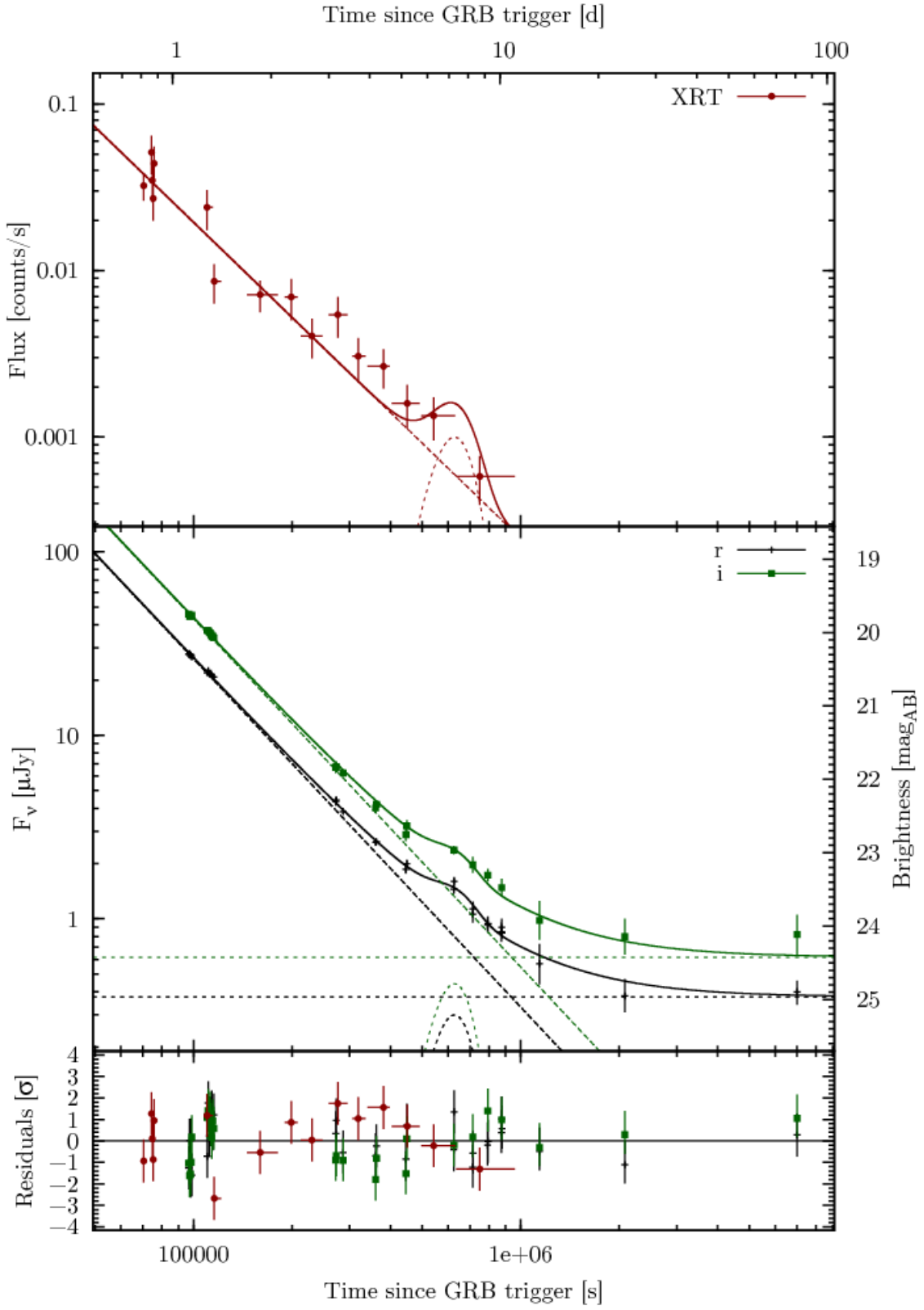

Figure 2.4 The panchromatic light curve of the afterglow of GRB 090323 as obtained with GROND in r' and i' filters and the XRT in the 0.3 to 10 keV range as an example of the light-curve fitting procedure. The model consists of a power law plus a flare and host component, shown in dashed lines. All bands share the same power-law index, flare time and width. The normalization for the power law, flare and host flux are unique for each band. The remaining GROND bands $g'z'JHK_S$ are omitted to enhance clarity.

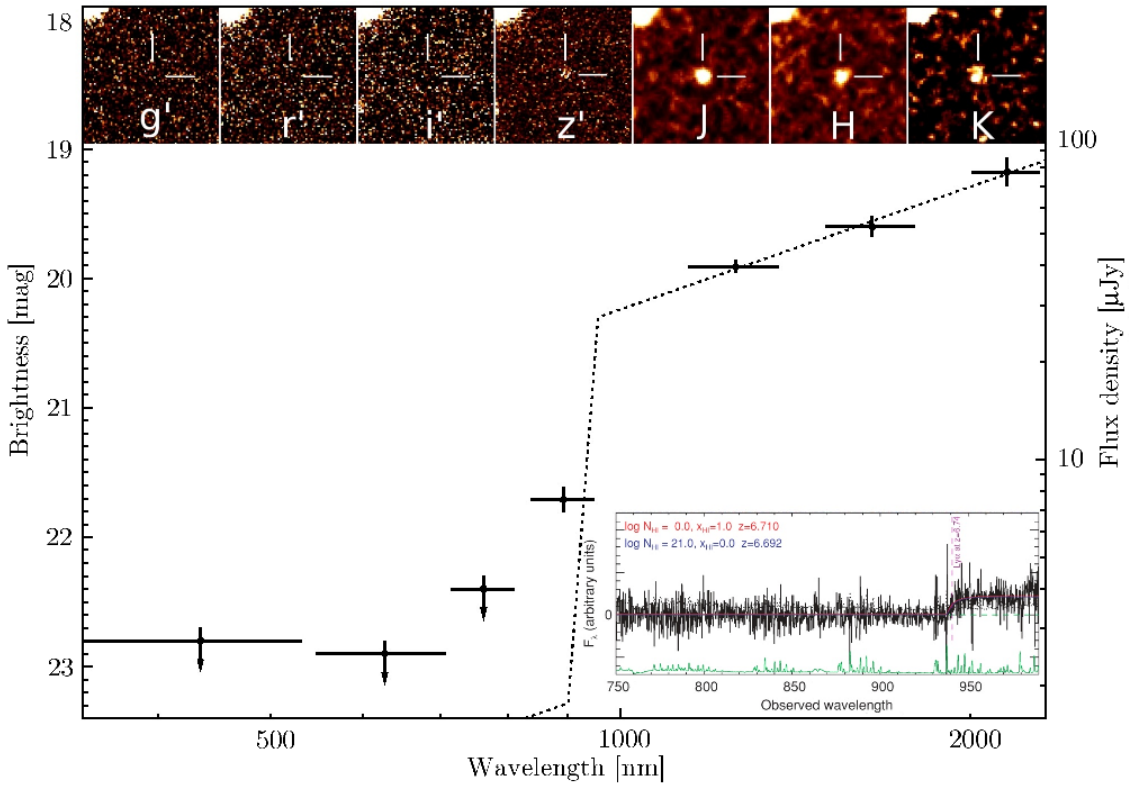

Figure 2.5 GROND photometric redshift of 6.44±0.30 for GRB 080913. The inset shows the afterglow spectrum obtained with FORS at the VLT, which resulted in a redshift measurement of $z = 6.7$ via spectroscopy, fully consistent with the GROND photo-z. The upper panel shows GROND images in the different filters. The afterglow is clearly detected in J and redder, very faint in z', whereas the i' band and bluer only yield upper limits. Adapted from Greiner et al. (2009b).

2.5.1 Photometric Redshifts with GROND

The software used for the measurement of the photometric redshift (photo-z) of GRBs and the amount of dust in their environment is based on the publicly available *hyperZ* code (Bolzonella et al., 2000). In addition to the existing treatment of the Lyman-α absorption according to Madau (1995) and default reddening templates from local galaxies, the code is complemented by several additions to fit it to the need of GRB science. In particular, power-law spectral templates with the possibility to constrain the spectral index and an additional reddening law according to Maiolino et al. (2004) were added. The program also includes the measured total GROND filter response, including all components in the optical pathway from the primary mirror of the telescope to the quantum efficiency of the detectors (Fig. 2.3). Special care was taken for a correct treatment of the filter curves: The total efficiency curve is calculated from its single components measured at their operating temperature inside the GROND vessel. The latter are actively controlled by a set of ten heaters and control loops, to ensure constant conditions during all observations.

Typical results are similar to the standard outputs of the original *hyperZ* version, including the photometric redshift, error bars or contours of the three main parameters redshift, spectral index and intrinsic reddening at arbitrary confidence levels and the statistical probability associated with the derived redshifts and secondary solutions if existent.

2.5.2 Simulating the Spectral Energy Distribution of GRB Afterglows

To test for the accuracy of the photometric redshift measurement with GROND, a sample of GRB afterglow spectra was simulated. The continuum spectrum of an afterglow in the optical/NIR range is a power law:

$$F_\nu(\lambda) = F_0(\lambda/\lambda_0)^{-\beta}$$

where F_0 is the normalization at $\lambda_0 = 1000$ nm. F_0 was chosen to be in the range of a standard afterglow as observed with GROND and shown in Fig. 2.2. The brightness of the afterglow and the observing conditions define the signal-to-noise ratio of the measurement and the image quality. The average accuracy for GROND with standard absolute flux calibration is 0.04 mag in $g'r'i'z'$ and 0.06 mag in JHK_S filters. These values were chosen as the minimum errors, where additionally a statistical error proportional to F_0 was added quadratically. The latter one is typically dominating in the range of faint bursts with an r'-band magnitude of 25 to 23.5 mag.

The Effect of Intrinsic Extinction

To model the effect of intrinsic reddening due to dust in the circumburst medium or the host galaxy, different dust attenuation laws $\eta(\lambda) = A_\lambda(\lambda)/A_V$ as shown in Fig. 2.6 were used. A_V is the dust extinction in the V band, typically centered at 550 nm. The optical thickness τ in the rest-frame of the host is then:

$$\tau_{\rm dust}(\lambda) = 0.92 A_V \eta(\lambda)$$

so that the model spectrum is reddened via:

$$F_\nu(\lambda) = F_0(\lambda/\lambda_0)^{-\beta} \exp[-\tau_{\rm dust}(\lambda/(1+z))]$$

The dust extinction laws of Milky Way (MW), Small and Large Magellanic Cloud (SMC, LMC) are parameterized according to Pei (1992). They strongly differ in their absolute UV absorption, which is decreasing in strength from SMC, over LMC to MW. The most prominent extinction features in the local extinction curves is the 2175 Å bump, which is generally attributed to absorption by graphite grains. While the feature is highly significant in MW and LMC models, it is absent in the SMC dust attenuation law (Fig. 2.6).

However, there is no physical reason to assume that the extinction law in the environment of a GRB from the early Universe necessarily has to comply with what is known from local galaxies. In particular, the dust content, constitution, element abundances and grain sizes can be significantly different and thus the specific intrinsic extinction. Therefore, a more generic approach is used to obtain a broader range of reasonable dust extinction laws by utilizing the Drude model proposed in Li et al. (2008) and Liang & Li (2009).

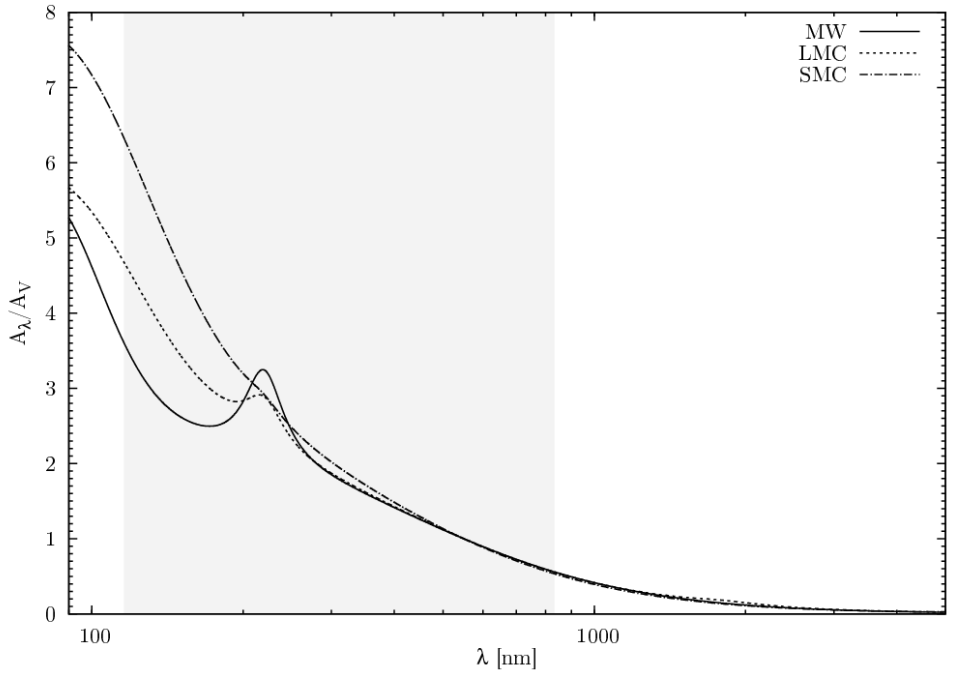

Figure 2.6 Dust attenuation laws in the local Universe. The gray shaded area represents the GROND filter range for a GRB at a redshift of $z = 2$. For a typical redshift of a *Swift* GRB (Jakobsson et al., 2006; Fynbo et al., 2009), GROND is very sensitive to broad features in the dust attenuation law (see Chapter 3) as well as the shape of the rest-frame UV extinction.

Here, $A_\lambda(\lambda)/A_V$ is described as a superposition of three components with:

$$A_\lambda/A_V(\lambda) = \frac{c_1}{(\lambda/80)^{c_2} + (80/\lambda)^{c_2} + c_3}$$
$$+ \frac{233[1 - c_1/(6.88^{c_2} + 0.145^{c_2} + c_3) - c_4/4.60]}{(\lambda/46)^2 + (46/\lambda)^2 + 90}$$
$$+ \frac{c_4}{(\lambda/217.5)^2 + (217.5/\lambda)^2 - 1.95}$$

where the four parameters c_1 to c_4 define the extinction curve. The MW dust attenuation law, for example, can be reproduced with $c_1 = 14.3$, $c_2 = 6.49$, $c_3 = 2.02$ and $c_4 = 0.0514$ (Li et al., 2008). By varying c_1 to c_4 in a reasonable parameter space, artificial extinction curves can be produced with a different strength of the UV extinction and the 2175 Å bump. Previous samples, however, show that the dust extinction law in the GRB environment is typically well reproduced with an SMC-type reddening (Kann et al., 2006). The statistical priors are thus set such, that 70% of all simulated GRB spectra are reddened with SMC-type and each 10% have MW-, LMC- or Drude-like extinction curves. The latter then represent a subset with artificial $A_\lambda(\lambda)/A_V$ dependencies.

Effects of Damped Lyman-α Systems

A large number of optical afterglow spectra show the clear presence of a Damped Lyman-α Absorber (DLA) (e.g., Watson et al., 2006). To quantify the effects of strong neutral hydrogen absorption associated with the GRB, the standard approach of DLA modelling (e.g., Vreeswijk et al., 2004) is used. Following the description of Totani et al. (2006) and references therein, the optical depth $\tau_{\rm DLA}$ of the DLA is defined as:

$$\tau_{\rm DLA}(\nu_{obs}) = N_{\rm HI}\sigma_\alpha[\nu_{\rm obs}(1+z_{\rm DLA})]$$

where σ_α is the Ly-α cross section with

$$\sigma_\alpha(\nu) = \frac{3\lambda_\alpha^2 f_\alpha \Lambda_{{\rm cl},\alpha}}{8\pi} \frac{\Lambda_\alpha(\nu/\nu_\alpha)^4}{4\pi^2(\nu-\nu_\alpha)^2 + \Lambda_\alpha^2(\nu/\nu_\alpha)^6/4}$$

f_α=0.4162 is the absorption oscillator strength and Λ_α is the damping constant of the Ly-α resonance with $\Lambda_\alpha = 3(g_{\rm l}/g_{\rm u})f_\alpha\Lambda_{{\rm cl},\alpha}$. The g-factors are the statistical weights of the first and second electronic niveau of hydrogen, and thus $g_l = 1$ and $g_u = 3$. The classical damping constant $\Lambda_{{\rm cl},\alpha}$ is given as $\Lambda_{{\rm cl},\alpha} = 8(\pi q_{\rm e})^2/(3m_{\rm e}c\lambda_\alpha^2)$ with the mass and charge of the electron $m_{\rm e}$ and $q_{\rm e}$ and the wavelength $\lambda_\alpha = 121.6$ nm of the Ly-α transition. The redshift of the DLA $z_{\rm DLA}$ is always set to the redshift of the burst in the following.

The reddened afterglow spectrum together with the effects of a DLA at the burst's redshift then becomes:

$$F_\nu(\lambda) = F_0(\lambda/\lambda_0)^{-\beta}\exp[-\tau_{\rm dust}(\lambda/(1+z))]\exp[-\tau_{\rm DLA}(\lambda/(1+z))]$$

Absorption lines due to metals in the GRB environment are omitted, as their effect on the integrated magnitude in broad-band filters as the GROND $g'r'i'z'JHK_S$ is negligible.

Effective Lyman-α Forest Opacity

Bluewards of the DLA centered at the redshifted λ_α, i.e. at $121.6(1+z)$ nm in the observers frame, the afterglow flux is further suppressed by the Lyα forest: intervening absorbers between the burst site and the observer. To model the effect of the Ly-α forest, the average opacity depending on the redshift is calculated. According to Faucher-Giguère et al. (2008), the effective optical depth $\tau_{\rm eff}$ of the Ly-α forest, can be described as:

$$\tau_{\rm eff} = 1.8\cdot 10^{-3}(1+z)^{3.92}$$

To compute the wavelength-averaged attenuation of the afterglow continuum due to line blanketing (Madau, 1995), averaged over different sight lines, the observed flux deficits $\langle D_{\rm A}\rangle$ between Ly-α

and Ly-β in the GRB rest-frame is calculated according to:

$$\langle D_{\rm A} \rangle = 1 - \Delta\lambda_{\alpha-\beta} \int_{\lambda_\beta(1+z)}^{\lambda_\alpha(1+z)} \exp[-\tau_{\rm eff}] d\lambda_{\rm obs}$$

and similarly for Ly-β, Ly-γ and Ly-δ and higher orders, e.g., for Ly-β:

$$\langle D_{\rm B} \rangle = 1 - \Delta\lambda_{\beta-\gamma} \int_{\lambda_\gamma(1+z)}^{\lambda_\beta(1+z)} \exp[-\tau_{\rm eff}^{\beta}] d\lambda_{\rm obs}$$

The most prominent contribution however, is Ly-α, and including higher order hydrogen absorption does not significantly change the average effective Ly-α forest opacity. To account for different measurements, measurement errors and specific sight lines, the observed flux deficits are allowed to vary according to the errors given in Faucher-Giguère et al. (2008). In particular, it is taken into account that the uncertainty is increasing with redshift. Consequently, the afterglow spectrum becomes:

$$F_\nu(\lambda) = \langle D_{\rm A} \rangle F_0 (\lambda/\lambda_0)^{-\beta} \exp[-\tau_{\rm dust}(\lambda/(1+z))] \exp[-\tau_{\rm DLA}(\lambda/(1+z))]$$

for $\lambda_\beta(1+z) < \lambda_{\rm obs} < \lambda_\alpha(1+z)$ and similar for $\langle D_{\rm B} \rangle$ and higher order absorptions. Below the Lyman limit of $\sim 90.7(1+z)$ nm, the observed flux is fully attenuated by the circumburst neutral hydrogen, and hence $F_\nu(\lambda) = 0$. Fig. 2.7 shows examples of ideal afterglow spectra in dependency of the relevant parameters.

Synthetic AB magnitudes of the afterglow spectrum in the different filters i are then derived via:

$$\mathrm{mag}^{\rm i}_{\rm AB} = -2.5 \log \frac{\int \mathrm{F}_\nu(\lambda) \mathrm{T}^{\rm i}(\lambda) \mathrm{d}\lambda}{\int \mathrm{T}^{\rm i}(\lambda) \mathrm{d}\lambda} + 23.9 \text{ mag}$$

where $T(\lambda)$ are the specific filter curves shown in Fig. 2.3. These magnitudes are then varied according to an associated error, which depends on the filter and overall normalization of the spectrum F_0, where F_0 was initially chosen to be in a reasonable range of previously observed GROND GRB afterglows. If the integrated flux over the bandpass is lower than the typical sensitivity limit of a one hour GROND exposure, the obtained magnitudes are converted into upper limits.

2.5.3 Redshift Accuracy

To investigate how accurate photometry can reproduce the redshift of a GRB, a mock set of ~ 1500 GRB spectra was simulated using the procedure described in Section 2.5.2. The properties of the simulations are shown in Fig. 2.8. Several priors have been set, to efficiently sample the region of specific interest. These priors are chosen such, that they resemble the information known about GRB afterglow spectra, and probe a parameter space which is accessible to the GROND instrument.

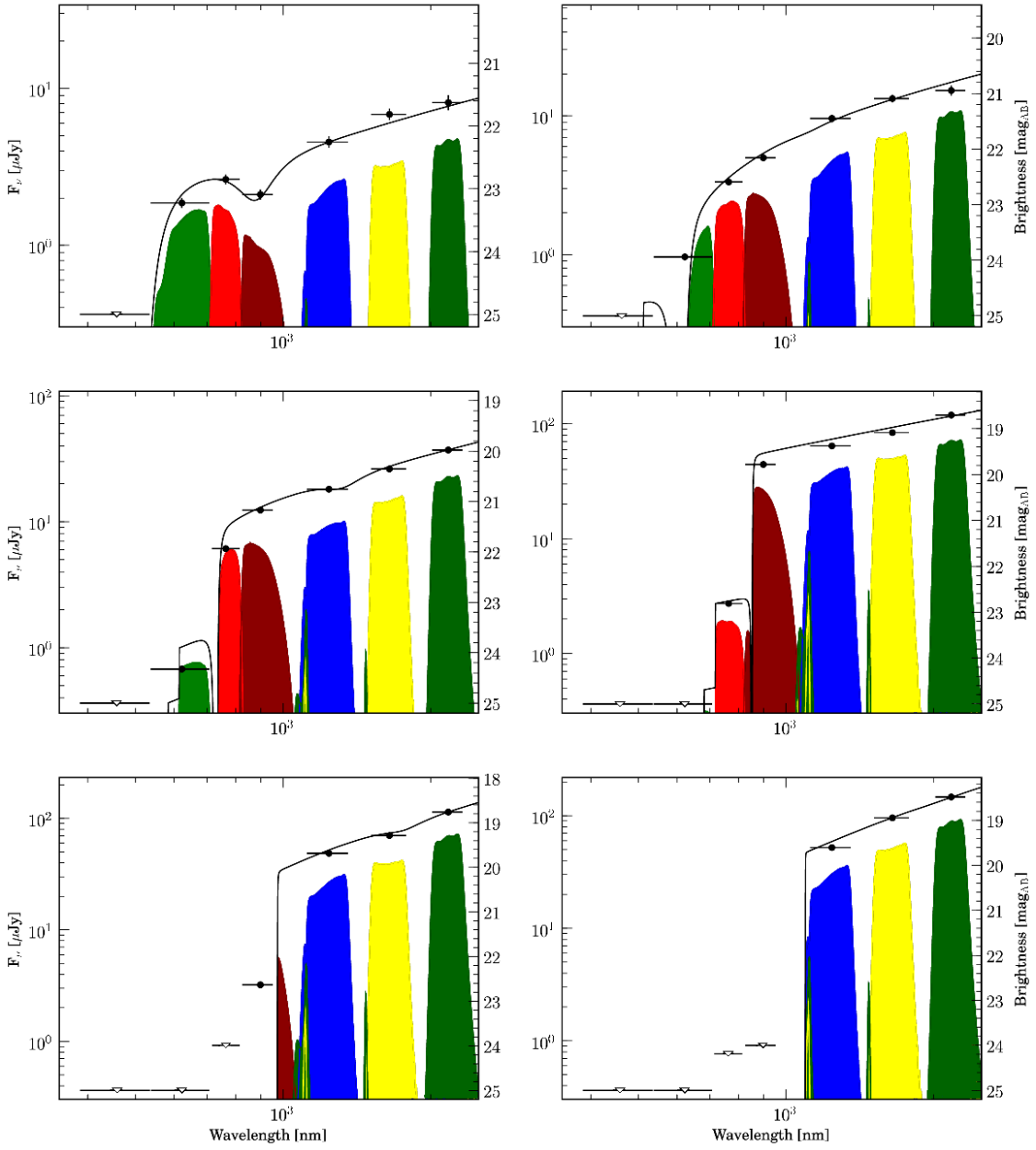

Figure 2.7 Simulated GROND SEDs for different input parameters. From top left to right bottom: redshift z = 3, 4, 5, 6, 7 and 8, extinction A_V = 0.6, 0.4, 0.3, 0.0, 0.2, 0,1, $\log(N_{\rm H})$ = 24, 23, 22, 21, 20, 19 and power-law index β = 0.2, 0.4, 0.6, 0.8, 1.0 and 1.2. Filled circles mark simulated detections, while open triangles upper limits. The vertical error bars on the measurement is a function of magnitude with respect to GROND's sensitivity. The horizontal error bars mark the 50% range of maximum throughput for each filter. The colored areas represent the flux transmission in the individual filters. Note the different extinction laws (i.e. a MW-type extinction with a 2175 Å feature in the upper left panel), and the blue leak of the H and K_S filters.

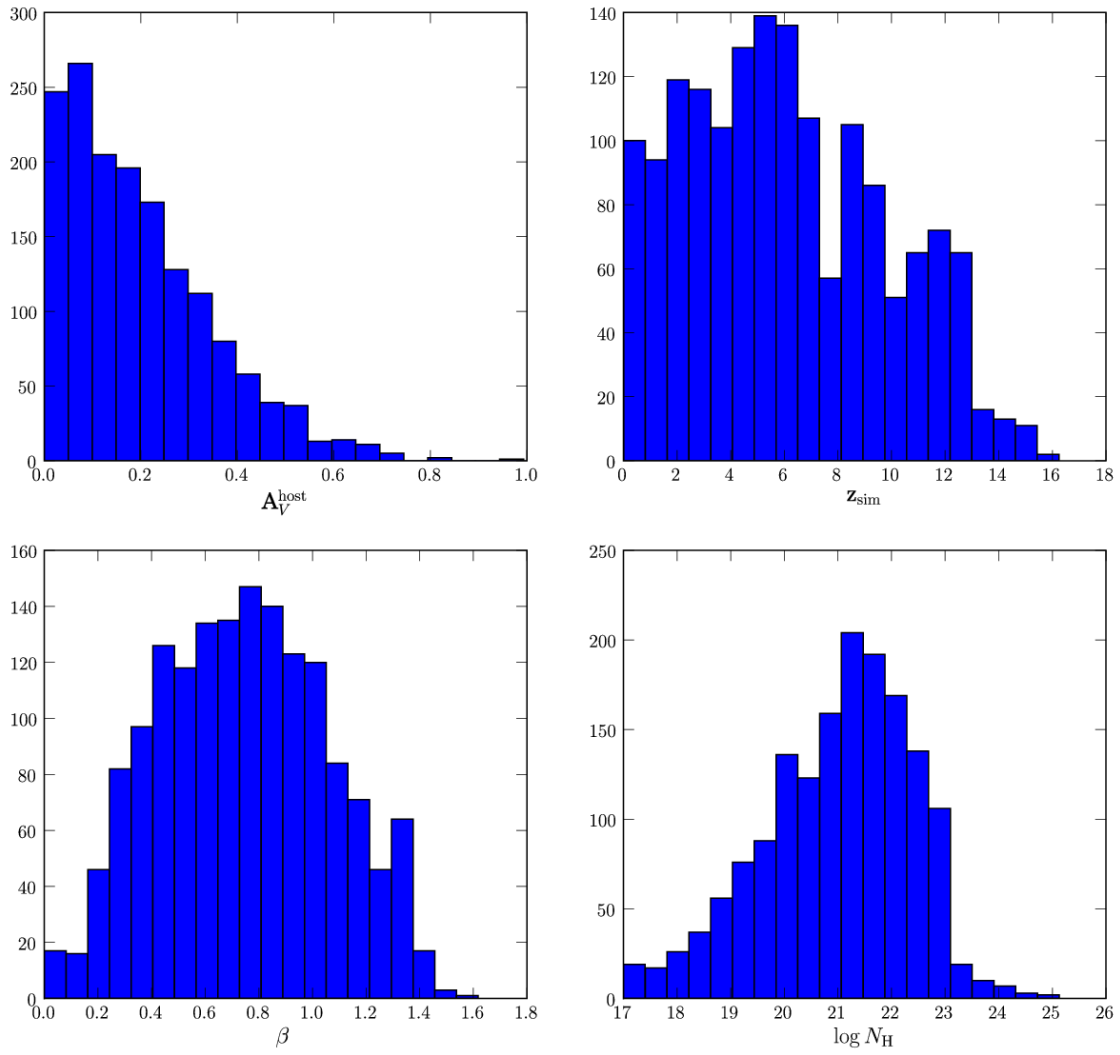

Figure 2.8 Histogram of the sample properties of ∼1500 simulated GROND SEDs depending on different input parameters. From top left to right bottom: intrinsic extinction A_V, simulated redshift z_{sim} , power-law slope β and hydrogen column densities $\log(N_H)$.

Still, the sample size is large enough with number statistics of ~ 300, to draw conclusions in extreme parts of the afterglow properties, e.g., $z \geq 8$, or $\log(N_H) \geq 22.5$.

The results of the simulation are summarized in Fig. 2.9. Theoretically, the lower limit of GROND photometric redshift measurements begins at $z \sim 2.4$. At this redshift the blue edge of the g' band starts to be significantly affected by absorption of the Ly-α forest or by the DLA associated with the GRB. However, the error in the photometric redshift in the range from 2.4 to 2.9 is still large, as the flux depression due to Ly-α is somewhat degenerate to intrinsic dust extinction in the burst environment. The associated average photo-z error Δz in this range is around ± 0.6 (lowest panel of Fig. 2.9) with a significant chance of misinterpreting dust reddening as Ly-α absorption (second panel of Fig. 2.9). This degeneracy is broken with increasing redshift, as Ly-α moves more and more into the g' band, reaching the r' band at a redshift of $z \sim 3.4$. The resulting drop in flux measured in g' is then too steep to be produced by dust. The average error due to different strengths of the DLA and Ly-α forest opacities at different sight lines is

± 0.4 in this range. Larger errors are only obtained with a very high DLA hydrogen column with $\log(N_{\rm H}) \geq 23$ or significant dust ($A_V \geq 0.5$). With further increasing redshift above ~ 3.4, Ly-α is in the r' band, with significant flux being still detected bluewards due to the transmissivity of the Ly-α forest. Consequently, two bands then show flux lower than the extrapolation of the power law, which results in a very accurate and robust redshift estimate with an average error $\Delta z = \pm 0.2$, with negligible chance of misidentification (see Fig. 2.7). At redshifts above 7, Ly$-\alpha$ is redwards of 973 nm, and only very little or no flux reaches the reddest optical band z'. As the spacing between z' and J is relatively large, the photometric redshift is rather loosely constrained, increasing from $\Delta z \sim 0.2$ at $z = 6.5$ to $\Delta z \sim 0.8$ at a redshift of 8.2. In this region, the flux decrease in J could be mimicked by some amount of intrinsic extinction and a lower redshift down to around 7. Above a redshift of $z \sim 9.5$, where bursts are expected to be relatively faint the transmitted flux in J is on average below the GROND sensitivity limit. With detections in only H and K_S, the problem is totally degenerate between the spectral power-law slope β and redshift, and only constraints on the power-law index from the previously measured range or from the X-ray spectrum allow a photometric redshift determination. Consequentially, the typical photo-z error reaches $\Delta z = \pm$ 2 at redshifts of 11 and above. The upper limit for a reliable photo-z estimate for GROND is $z \sim 13.5$.

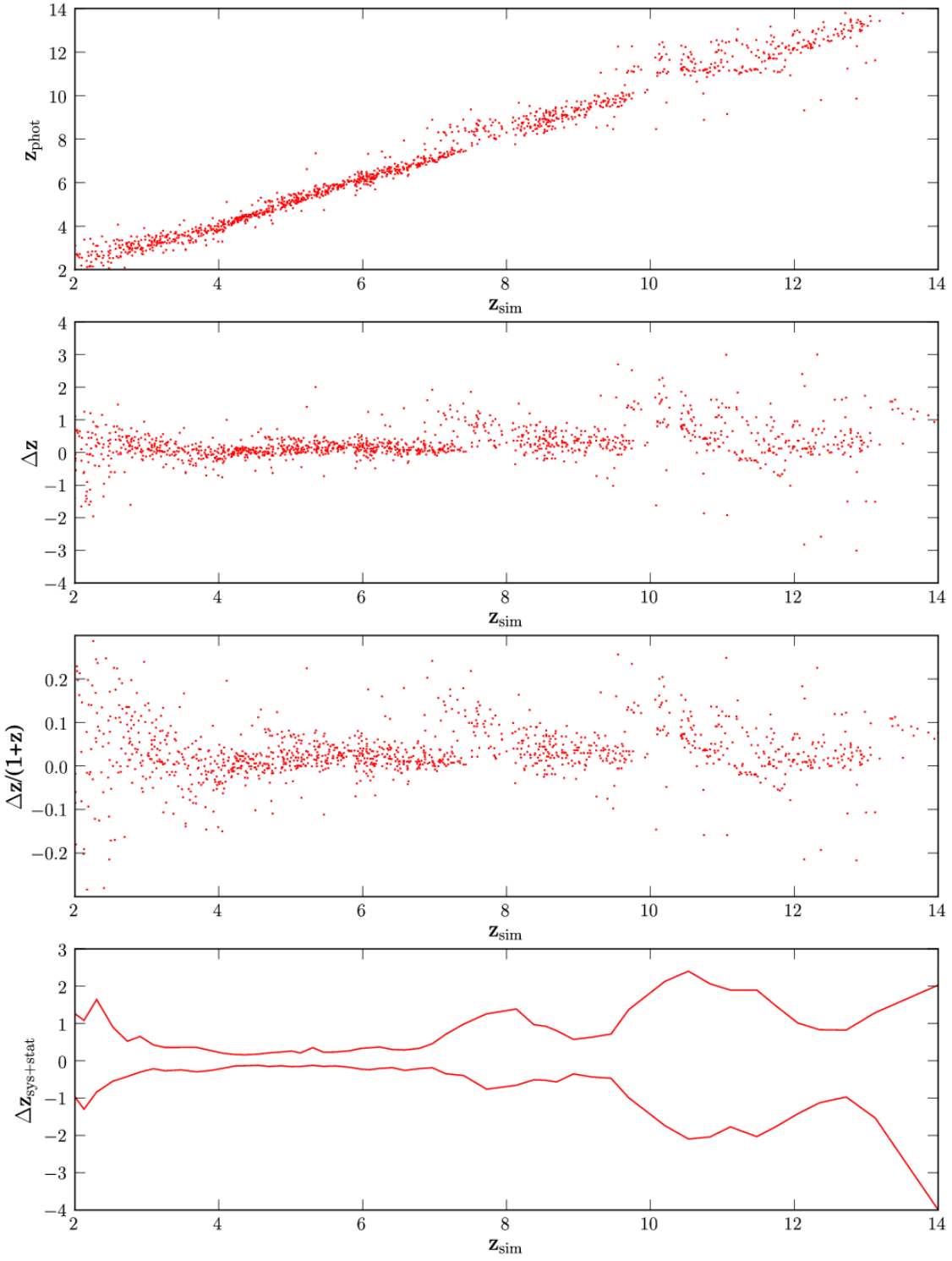

Figure 2.9 Results of the simulation of GRB afterglow spectra and photometric redshift measurement. From top to bottom: Photometric redshift $z_{\rm phot}$, absolute difference $\Delta z = z_{\rm phot} - z_{\rm sim}$, relative difference $\Delta z/(1+z)$ and total, i.e. quadratically added systematic and statistical error $\Delta z_{\rm sys+stat}$ versus simulated, i.e. input redshift $z_{\rm sim}$

Chapter 3

The 2175 Å Dust Feature in a Gamma-ray Burst at Redshift 2.45 [1]

ABSTRACT

We present optical and near-infrared photometry of the afterglow of the long Gamma-ray Burst GRB 070802 at redshift 2.45 obtained with the ESO/MPI 2.2 m telescope equipped with the multi-channel imager GROND. Follow-up observations in $g'r'i'z'$ and JHK_S bands started at ~ 17 minutes and extended up to 28 hr post burst. We find an increase in the brightness of the afterglow at early times, which can be explained by the superposition of reverse and forward shock (FS) emission or the onset of the afterglow FS. In addition, we detect a strong broad absorption feature in the i' band, which we interpret as extinction from the redshifted 2175 Å bump in the GRB host galaxy. This is one of the first and clearest detections of the 2175 Å feature at high redshift. It is strong evidence for a carbon rich environment, indicating that Milky Way- or Large Magellanic Cloud- like dust was already formed in substantial amounts in a galaxy at $z = 2.45$.

3.1 Introduction

Gamma-ray Bursts (GRBs) are intense extragalactic flashes of γ-rays with durations between several tenths to hundreds of seconds (e.g. Fishman et al., 1994; Mészáros, 2006). They cluster in two different categories of duration and spectral hardness: short-hard bursts versus long-soft bursts (Kouveliotou et al., 1993). GRBs are followed by longer lasting afterglows in radio to X-rays (e.g. Katz, 1994; Mészáros & Rees, 1997; Zhang, 2007). The enormous energy release in γ-rays is unaffected by dust or gas absorption, so GRBs are detectable out to very high redshifts (e.g. Lamb & Reichart, 2000; Kawai et al., 2006). These characteristics make GRBs potential tools to constrain the history of star formation (Bromm & Loeb, 2002) and chemical evolution in the universe (Savaglio, 2006; Fynbo et al., 2006; Berger et al., 2006).

[1] T. Krühler, A. Küpcü Yoldaş, J. Greiner, C. Clemens, S. McBreen N. Primak, S. Savaglio, A. Yoldaş, G. P. Szokoly and S. Klose (2008), *Astrophysical Journal*, 685, 376

The GRB-SN connection (e.g. Zeh et al., 2004; Woosley & Bloom, 2006) strongly supports the association of long GRBs with the core-collapse of very massive stars, and therefore with regions of high-mass star formation in the host galaxies (Paczynski, 1998). High-mass star-forming regions show signatures of significant dust and gas absorption in ultra-violet and optical spectra of bright GRB afterglows (Savaglio, 2006; Berger et al., 2006; Fynbo et al., 2007). In fact, a large number of bursts do not show optical afterglows despite rapid and deep optical follow-up observations (e.g. Stratta et al., 2004; Rol et al., 2005). Natural explanations for "optically dark bursts" (Groot et al., 1998) include dust extinction in the host galaxy (e.g. Fynbo et al., 2001; Klose et al., 2003) and high redshift (e.g. Groot et al., 1998), both efficiently suppressing any flux in the observed optical bands (Roming et al., 2006). Several bursts with moderate dust absorption have been detected (e.g. Kann et al., 2006), which may represent only the lower end of the host extinction distribution (Schady et al., 2007). The detection of significant reddening in a host is strongly instrumentally biased due to the lack of rapid near-infrared follow-up observations with large-aperture telescopes. In particular, one of the biggest shortcomings of all multi-color monitoring of afterglows so far was the lack of a simultaneous coverage of the optical to near-infrared (NIR) bands.

The Gamma-Ray Burst Optical/Near-infrared Detector (GROND) is a seven-channel imager primarily designed for fast follow-up observations of GRB afterglows (Greiner et al., 2007b, 2008). It enables the detection and identification of GRB afterglows in a broad wavelength range (380-2400 nm). Due to the use of dichroic beam splitters it is capable of simultaneous imaging in seven bands, $g'r'i'z'$ (similar to the Sloan system) and JHK_S. GROND has been mounted on the 2.2 m ESO/MPI telescope on LaSilla/Chile since April 2007. The instrument is operated robotically and is capable of monitoring the light curve of the transient starting from a minimum of a few minutes after burst alert. The field of view of the instrument is $10' \times 10'$ in the NIR and $5.4' \times 5.4'$ for the optical bands (Greiner et al., 2008). The fast response, medium-sized telescope aperture, NIR capabilities, and unique optical design makes GROND an ideal tool for follow-up observations of GRBs.

Here we report on first GROND follow-up observations of GRB 070802 (Section 3.2) and derive constraints on the GRB ejecta and its circumburst properties (Section 3.3).

3.2 Observations

3.2.1 *Swift* Observations

The BAT (Burst Alert Telescope) instrument (Barthelmy et al., 2005) onboard the *Swift* satellite (Gehrels et al., 2004) triggered on the long-soft GRB 070802 at $T_0 = 07:07:25$ UTC and immediately slewed to the burst (Barthelmy et al., 2007). The BAT light curve shows a single peak starting at $T_0 + 5$ s and ending at $T_0 + 50$ s. There is evidence at the 3σ level for a precursor at $T_0 - 150$ s (Cummings et al., 2007). The T_{90} for GRB 070802 is 16.1 ± 1.0 s and the fluence in the 15-150 keV band is $(2.8 \pm 0.5) \times 10^{-7}$ erg cm^{-2} (Cummings et al., 2007).

The X-Ray Telescope (XRT; Burrows et al., 2005b) began follow-up observations of the burst

field 138 s after the trigger and detected an uncatalogued fading X-ray source at a position of R.A.(J2000.0)=02^h 27^{min} $35^s.76$, decl.(J2000.0)=-55° 31′ 38.″4 with a refined 90% coincidence error of 2.″1 (Mangano et al., 2007). The XRT light curve decays with a slope of $\alpha \sim -2$ until $T_0 + 500$ s and then remains flat until ~ 4 ks. Afterwards the light curve decays with a power-law index of ~ -1 until it fades below the XRT sensitivity limits (Mangano et al., 2007). No bright flares are detected in the XRT light curve.

The third instrument onboard *Swift*, the Ultra-Violet Optical Telescope (UVOT, Roming et al., 2005) started observations at $T_0 + 100$ s and did not find any transient sources inside the XRT error circle down to 19.5 mag (u filter), 21.3 mag (b filter) and 21.2 mag ($uvw2$ filter) (Immler et al., 2007).

3.2.2 GROND Optical and Near-infrared Observations

GROND responded to the *Swift* GRB alert and initiated automated observations on the 2007 August 2 at 07:24:09 UTC, starting 7 minutes 16 s after the *Swift* trigger and 16 minutes 44 s after the onset of the burst. A predefined sequence of exposures with successively increasing exposure times were executed, acquiring images in all seven photometric bands simultaneously. The observations continued for two nights, after which the afterglow had faded below the GROND sensitivity limits. A variable point source in the NIR bands (Greiner et al., 2007a) inside the *Swift* XRT error circle was identified by the GROND data reduction pipeline (Küpcü-Yoldaş et al., 2008). The transient is shown in Fig. 3.1 and its absolute position is calculated to be R.A.(J2000.0)=02^h 27^m 35.68^s, decl.(2000.0)=-55° 31′ 38.9″ with an uncertainty of 0.3″ compared to 2MASS reference field stars. The afterglow was also observed and detected by the Magellan telescope at Las Campanas Observatory (LCO, Berger & Murphy, 2007) and the Very Large Telescope (VLT), the latter yielding a spectroscopic redshift of $z = 2.45$ (Prochaska et al., 2007).

In total, 2036 NIR images with an integration time of 10 s each and 56 CCD optical frames were obtained with GROND. The CCD integration times scaled with the brightness of the transient from 45 s at early times to 10 minutes when the source had faded. Sky conditions were clear with a mean seeing around 1.2″. All GROND data were obtained at airmasses between 1.35 and 1.12.

Optical and NIR image reduction and photometry was performed using standard IRAF tasks (Tody, 1993). A general model for the point-spread function (PSF) of each image was constructed using bright field stars and fitted to the afterglow. In addition, aperture photometry was carried out, and the results were consistent with the reported PSF photometry. Photometric calibration was performed relative to secondary standards in the GRB field. During photometric conditions, two spectrophotometric standard stars, SA114-750 and SA114-656, both primary Sloan standards (Smith et al., 2002), were observed with GROND. Observations of the GRB field followed within 4 minutes. The magnitudes of SA114-750 and SA114-656 were transformed to the GROND filter system using their spectra and the GROND filter curves (Greiner et al., 2008). The obtained zeropoints were corrected for atmospheric extinction differences and used to calibrate stars in the GRB field, shown in Fig. 3.1. The apparent magnitudes of the afterglow were measured with respect to the secondary standards reported in Table 3.1.

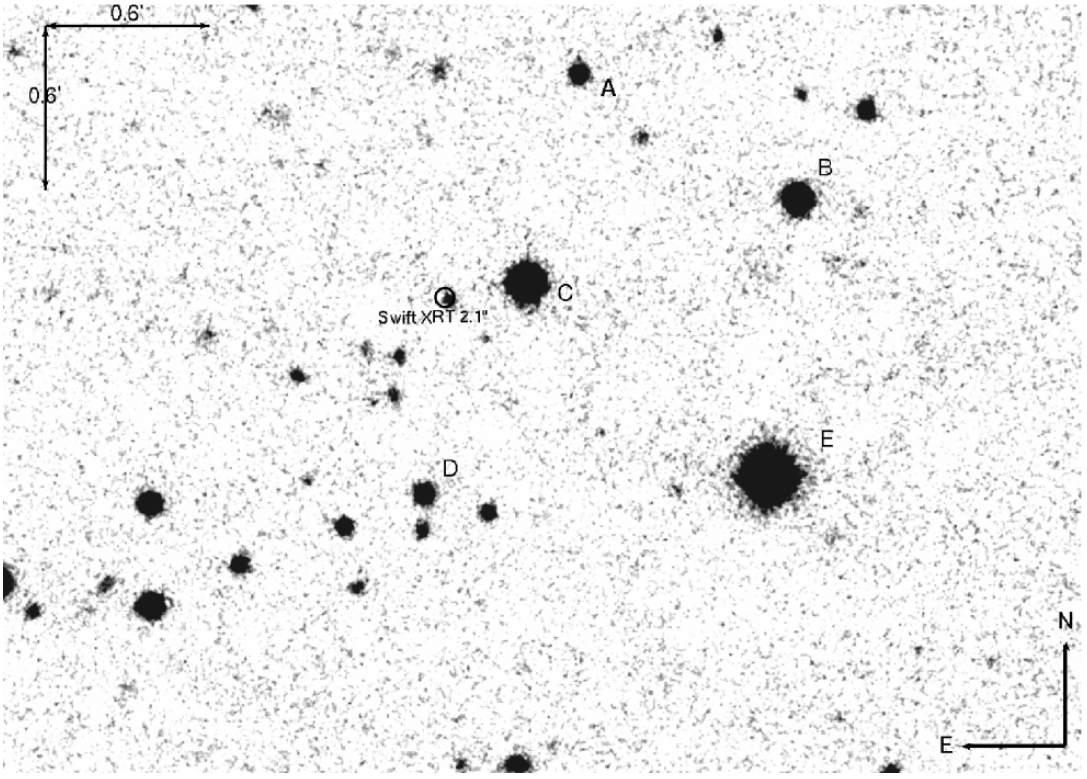

Figure 3.1 NIR afterglow of GRB 070802 in the J band at $t = 3.4 \pm 0.3$ ks post burst, including the Swift XRT error circle. Only a $\sim 3' \times 2.5'$ segment of the original $10' \times 10'$ image is shown. The GROND NIR images have a pixel scale of $0\farcs6$/px each. The image is a combination of 48 stacked 10 s exposures and also shows the secondary standards used for calibration, marked as A, B, C, D and E.

Vega magnitudes have been transformed to the AB system using transformation factors for the GROND filter system as $\delta g' = 0.01$ mag, $\delta r' = 0.15$ mag, $\delta i' = 0.39$ mag, $\delta z' = 0.52$ mag, $\delta J = 0.91$ mag, $\delta H = 1.38$ mag and $\delta K_S = 1.80$ mag. All reported afterglow magnitudes are corrected for Galactic foreground reddening ($E_{B-V} = 0.026$ mag, Schlegel et al., 1998). Assuming $R_V = 3.1$ for the Milky Way, this leads to $A_K = 0.01$ mag, $A_H = 0.02$ mag, $A_J = 0.03$ mag, $A_z = 0.04$ mag, $A_i = 0.05$ mag, $A_r = 0.07$ mag and $A_g = 0.10$ mag for the GROND filter bands.

The afterglow is detected in all seven GROND bands, however, it was too dim to construct a light-curve with reasonable time resolution in the filter bands g' and i'. The light-curves obtained in the $r'z'JHK_S$ bands are presented in Fig. 3.2. The light-curve behavior is dominated by an early rise in brightness, after which it declines with a bump superimposed onto the overall decay. The observed variations occur in all five GROND bands, and the generic light-curve shape is achromatic within the measurement uncertainties.

3.3 Analysis

3.3.1 The Early Light Curve of the Afterglow of GRB 070802

According to the fireball model (e.g. Wijers et al., 1997; Sari & Piran, 1999; Piran, 2005; Mészáros, 2006), GRBs produce their prompt emission in γ-rays from internal shocks of an ultra-relativistic outflow from a compact source and long-wavelength afterglows from the interaction of the ejecta with the circumburst medium. After the prompt internal shock phase, the optical afterglow light curve is composed of a superposition of two different emission components: the reverse shock (RS) propagating into the ejecta and the forward shock (FS) traveling into the surrounding medium (Zhang et al., 2003a). Rapid optical observations of the early transition phase between prompt and afterglow emission can constrain the nature of the outflow (Nakar & Piran, 2004). While baryonic ejecta are expected to produce an optical flash, that can be associated with a RS, a Poynting flux dominated afterglow should preferentially show the FS emission. The hydrodynamical calculations from the fireball model have succeeded in describing the generic afterglow of GRBs from several minutes to days post burst. However, the majority of bursts do not show bright optical flashes and apparently lack a strong RS emission component (Roming et al., 2006). This fact provides observational support that the strength of the optical emission from the RS may be weaker than previously calculated (Beloborodov, 2005).

A baryonic shell expanding into a homogeneous medium is fully described by the shell isotropic equivalent energy E, its width Δ, the initial Lorentz factor Γ_0 and the ISM density n (Nakar & Piran, 2004). In the thick shell case, the initial Lorentz factor is large, and the swept up circumburst medium decelerates the ejecta efficiently (Kobayashi & Sari, 2000). Here, the RS becomes relativistic in the rest frame of the unshocked ejecta. The critical Lorentz factor Γ_c discriminating between the relativistic thick ($\Gamma_0 > \Gamma_c$) and Newtonian thin shell ($\Gamma_0 < \Gamma_c$) cases

is given by (Zhang et al., 2003a).

$$\Gamma_c \cong 125 E_{52}^{1/8} n^{-1/8} T_2^{-3/8} \left(\frac{1+z}{2}\right)^{3/8} \tag{3.1}$$

where E_{52} is the isotropic energy equivalent in units of 10^{52} erg and T_2 is the burst duration in units of 100 s. For the thin shell case the Lorentz factor at the crossing time t_x of reverse and forward shock is $\Gamma_x = \Gamma_0$. By measuring the peak of the RS, one can directly derive Γ_0 for the thin shell case:

$$\Gamma_x = \Gamma_c (T/t_x)^{3/8} \tag{3.2}$$

with only a weak dependence on E_{52}/n.

The light curve shown in Fig. 3.2 displays a behavior consistent with the above theoretical predictions. It rises achromatically at early times and reaches a first peak at ∼2 ks. Afterwards the light curve declines with a power-law index of ~ -2 until ~ 3 ks. Between 3 and 10 ks post burst our data are not conclusive. There may be a plateau phase, although a power-law decline with the late time index cannot be ruled out. At late epochs the afterglow follows the canonical power-law decay. The data are compatible with a constant power-law spectrum at all times, although there is an indication for chromatic changes at peak brightness. There is no evidence for a jet break in the GROND data out to 90 ks post burst.

We used two different approaches to analyze the light curve quantitatively. First, a physical model combining the forward and reverse shock component (RS-FS model), and second a forward shock model alone (FS model).

Within the framework of the combined RS-FS model, the first peak can be interpreted as the peak of the reverse shock, whereas the possible rebrightening phase around 4 ks is related to the FS peak. A complete parametrization of the RS is given by a broken power law (Beuermann et al., 1999; Nakar & Piran, 2004):

$$F_\nu^r(t) = F_0^r \left[\left(\frac{t}{t_1}\right)^{-s^r \alpha_1^r} + \left(\frac{t}{t_1}\right)^{-s^r \alpha_2^r} \right]^{-1/s^r} \tag{3.3}$$

with power-law indices of rise ($\alpha_1^r \geq 0$) and decline ($\alpha_2^r \sim 2$), a peak time $t_{\rm peak} = t_1(\alpha_1^r/-\alpha_2^r)^{1/(s^r(\alpha_1^r-\alpha_2^r))}$, normalization F_0^r, and the sharpness of the break s^r.

The FS parametrization used for the light curve analysis is similar to the RS:

$$F_\nu^f(t) = F_0^f \left[\left(\frac{t}{t_2}\right)^{-s^f \alpha_1^f} + \left(\frac{t}{t_2}\right)^{-s^f \alpha_2^f} \right]^{-1/s^f} \tag{3.4}$$

According to theoretical calculations (Sari et al., 1998), a power-law index of the FS with $\alpha_1^f \approx 1/2$ is expected for the forward shock rise, followed by a shallow decline $\alpha_2^f \approx 3/4 - 3/4p$. Here p is the power-law index of the energy distribution of the shocked electrons (Sari et al., 1998; van Paradijs et al., 2000). The power-law indices for both forward and reverse rise and decline, as well as the peak time, have been fitted using the complete multi-color data set. The flux normalizations result

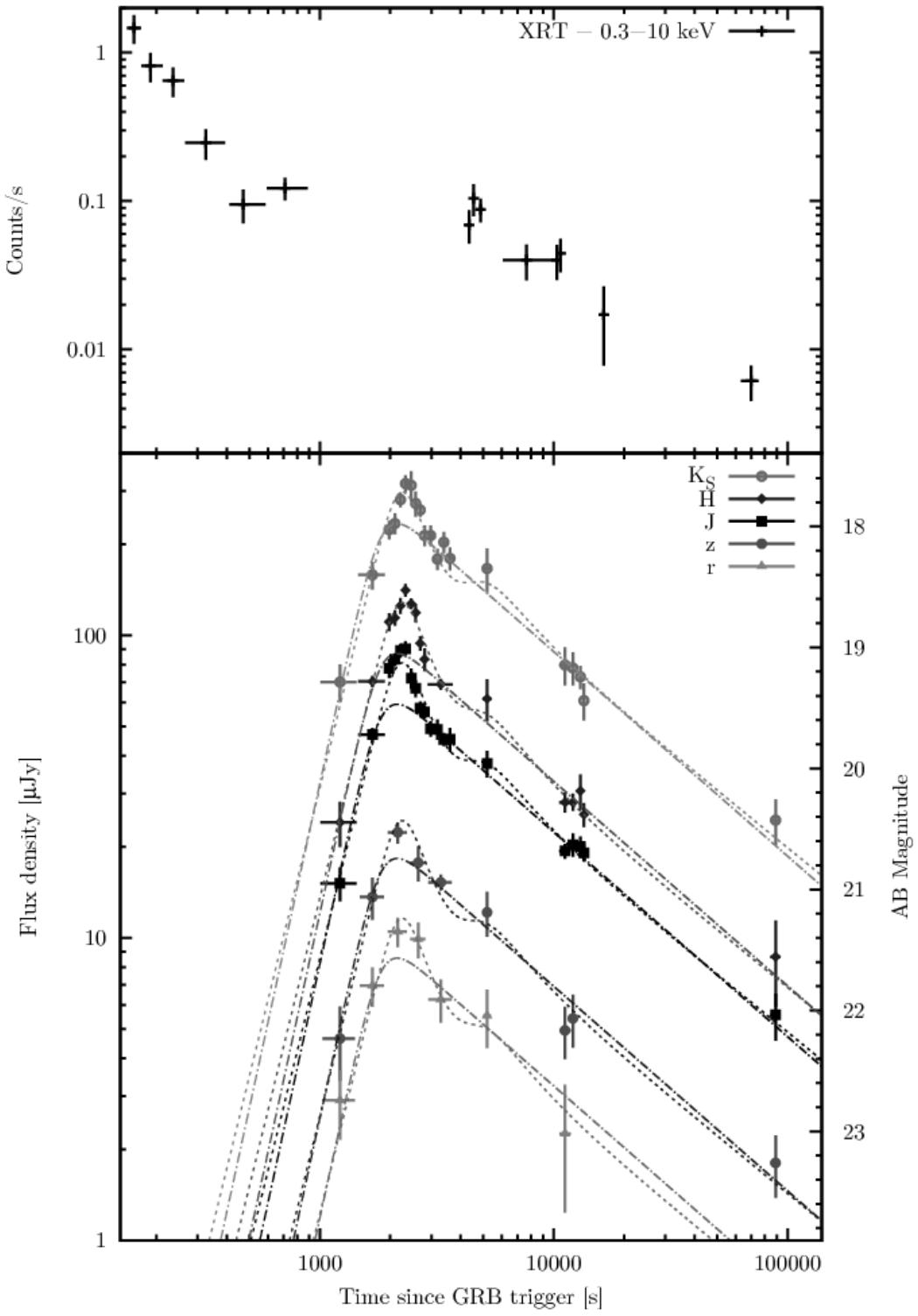

Figure 3.2 X-ray and optical/NIR light curve of the afterglow GRB 070802. The X-ray light curve in the upper panel was obtained from the *Swift* XRT light-curve repository (Evans et al., 2007). The afterglow light curve in the GROND bands r', z', J, H and K_S is shown in the lower panel. In the g' and i' bands the afterglow was too dim to construct a light curve. Also shown are the best-fit models in dotted lines for the RS plus FS model and in dashed-dotted lines for the FS model. The simple model of an exclusive FS emission cannot explain the light-curve shape around peak brightness and requires an extra emission component superimposed to the overall rise and decay.

from single-band fits. The result of the combined fit of the RS and FS are consistent with the expected power-law decline of the RS with a power-law index ~ -2 (Tables 3.2 and 3.3).

To constrain the RS/FS fit, the sharpness parameter of the power-law transition (s^r) and the time of the putative FS (t_2) had to be fixed to 2.5 and 4.5 ks, respectively. However, this affects mainly the late time properties of the afterglow, whereas our analysis is concentrated on the early epoch dominated by the rise of the light curve. Specifically, the peak of the light curve is unaffected by the fixed parameters.

We also fit the data with the FS broken power law alone. In this case the early rise of the afterglow is interpreted as the onset of the afterglow. The single FS component fit is consistent with a power-law rise index ~ 3, as expected for an ISM profile and results in fit parameters as reported in Tables 3.2 and 3.3. This simple model alone cannot explain the steep decay of the initial peak. A further emission component at ~ 2.5 ks superimposed on the overall power-law rise and decay is required to explain the observed light curve features. Rebrightening episodes and variabilities in the optical afterglow light curve have been observed in a number of previous burst, e.g. GRB 021004 (e.g. Fox et al., 2003), GRB 030329 (e.g. Lipkin et al., 2004), GRB 050502A (Guidorzi et al., 2005), GRB 061126 (Perley et al., 2008b) and GRB 070125 (Updike et al., 2008). Possible explanations include inhomogeneities in the density profile of the circumburst medium (e.g. Wang & Loeb, 2000; Lazzati et al., 2002), in the angular distribution of the outflow (i.e. the patchy shell model, Kumar & Piran 2000) or late energy injection by refreshed shocks (e.g. Rees & Mészáros, 1998). Nakar & Granot (2007) find that sharp rebrightenings in the optical light curve are very unlikely to be caused by density jumps in general and favor the refreshed shock (GRB 030329) or patchy shell model (GRB 021004). Points in the afterglow light curve of GRB 070802 which are attributed to the superimposed component at ~ 2.5 ks have been excluded from the generic light curve fit of the exclusive FS model.

The peak times of both parametrizations can then be used to constrain the initial conditions in the ejecta. Due to the lack of sufficient time resolution between 3 and 10 ks, the two models cannot be clearly discriminated.

Within the interpretation of the early brightening of the afterglow of GRB 070802 as the RS, a wind-shaped circumburst medium and Poynting flux dominated models are implicitly ruled out. In both cases a RS would not cause a t^{-2} decay and it is very unlikely to be imitated by other phenomena (Nakar & Piran, 2004).

Although the profile of the light curve of the optical/NIR afterglow shows evidence for a reverse shock in an ISM circumburst medium, there is still a problem with its timing relative to the burst. The putative RS peak at ~ 2 ks is highly delayed with respect to the duration of the burst (16.4 ± 1.0 s), which is possible for a very thin shell only. As a consequence, the initial Lorentz factor of the outflow, which is estimated to be $\Gamma_0 \approx 40(E_{52}/n)^{1/8}$, is quite small compared to the expected distribution of the Lorentz factors above 100 (Piran, 2000) and previous bursts (Molinari et al., 2007; Pe'er et al., 2007; Ferrero et al., 2009). A possible solution within the context of the RS scenario would be an extremely low density environment.

Alternatively, the initial increase in brightness might be related to the onset of the forward shock

of the afterglow itself (Panaitescu & Kumar, 2000), as suggested for GRB 060418 and GRB 060607A (Molinari et al., 2007). In this case, a RS component might be hidden under the dominating FS emission or have occurred even before the GROND observations. A possible explanation for the superimposed component occurring at the light curve peak would then be e.g. multiple energy injections by refreshed shocks (e.g. de Ugarte Postigo et al., 2005) or dense clumps in the circumburst medium (e.g. Guidorzi et al., 2005). Flares and rebrightenings are frequently observed in X-ray afterglow light curves (O'Brien et al., 2006; Zhang et al., 2006). The fact that the length of the flare ($\sim$ 1200 s) is compatible with the start time of the flare ($\sim$ 1800 s post burst) supports the refreshed shock scenario.

Using Sari & Piran (1999), Panaitescu & Kumar (2000), and Molinari et al. (2007), we estimate Γ_0 for the ISM case to $\Gamma_0 \approx 160 \left(\frac{E_{53}}{\eta_{0.2} n}\right)^{1/8}$, and for the wind shaped case to $\Gamma_0 \approx 80 \left(\frac{E_{53}}{\eta_{0.2} A^*}\right)^{1/4}$, both more in line with previous bursts and theoretical predictions. Here E_{53} is the isotropic-equivalent energy released in γ-rays in 10^{53} erg, $\eta_{0.2}$ the 0.2 normalized radiative transfer efficiency, n the ISM density in cm^{-3} and A^* the normalized wind density. The steep rise of the light curve with a power-law index of 3.56 ± 0.36 favors the homogeneous circumburst environment (Panaitescu & Kumar, 2000).

3.3.2 The Spectral Energy Distribution

The Intrinsic Extinction in Previous GRB Host Galaxies

The GRB/SN connection hints strongly at the progenitors of GRBs, which are supposedly very massive, fast rotating Wolf-Rayet stars (e.g. Woosley & Bloom, 2006). In this collapsar model (MacFadyen & Woosley, 1999) one would expect long GRBs preferentially in regions with a high star formation rate (SFR) with significant amount of dust and gas in the host along the GRB sight line. However, most previous bursts show only a moderate or low reddening (Galama & Wijers, 2001; Kann et al., 2006, 2008), contrary to the observed high column densities of heavy elements and strong depletion of refractory elements (Savaglio & Fall, 2004) .

The main feature discriminating between the extinction curves in the Large Magellanic Cloud (LMC), Milky Way (MW), Small Magellanic Cloud (SMC), and starburst galaxies is the presence and intensity of an absorption feature at 2175 Å rest-wavelength. This feature is generally associated with the absorption of graphite grains, whose abundance and sizes changes between the different models (Draine, 2003). The feature is most prominent from the MW to the LMC, whereas it is practically absent in the SMC (Cardelli et al., 1989) and starburst galaxies (Calzetti, 2001). SMC and starburst models have a much larger amount of far ultraviolet (FUV) extinction. Previous bursts strongly favored SMC like dust host galaxies (Schady et al., 2007; Stamatikos et al., 2007; Kann et al., 2008), and only for a very few of them does a MW model provide a better fit. In addition, the host extinction shows a trend of lower extinction at higher redshift (Kann et al., 2006). However, with increasing redshift, both the FUV absorption and the 2175 Å bump significantly decrease the detection efficiency for optical follow-up observations, so the present extinction distribution and its dependence on the bursts redshift might be strongly instrumentally biased.

The SED of the Afterglow of GRB 070802

In the present analysis we used MW-, LMC- and SMC-like extinction models (Seaton, 1979; Fitzpatrick & Massa, 1986; Fitzpatrick, 1986; Prevot et al., 1984) as templates to fit our multi-band data. All of the GROND optical and NIR data were obtained simultaneously at the time epoch between 1.5 and 3.6 ks post burst. As the generic shape of the early light curve is achromatic, we can exclude large effects from an evolving spectrum. The data were fit by a power law and extinction templates from the LMC, SMC, and MW in *hyperZ* (Bolzonella et al., 2000). The amount of dust, power-law slope and normalization were free parameters in the fit. The redshift was fixed to the spectroscopic redshift of 2.45 obtained by the VLT (Prochaska et al., 2007).

The GROND SED is shown in Fig. 3.3 and was well fit by the LMC (reduced $\chi^2 = 0.67$ for 4 d.o.f) and the MW (reduced $\chi^2 = 1.96$ for 4 d.o.f.) extinction models, while the fit was considerably worse for SMC-like extinction (reduced $\chi^2 = 4.57$ for 4 d.o.f.). The large χ^2 difference between LMC and MW models is mostly due to the g' band magnitude, where the error in the GROND data is relatively large. The dust extinction in the GRB host in the best fit model is $A_V^{\rm host} = 0.9 \pm 0.3$ mag for MW and $A_V^{\rm host} = 1.8 \pm 0.3$ mag for LMC models. We caution that these values are derived using local extinction curves for a galaxy at a redshift of 2.45. The extinction curve and thus the amount of dust reddening could be significantly different. In addition, intervening absorbers could contribute to the observed dust extinction, which is only resolved by the spectrum (Fynbo et al., 2007).

We detect a strong absorption feature in the GROND i' band. GROND i' is slightly narrower than the SDSS i' band and is located at 7630±537 Å. The 2175 Å bump at redshift 2.45 (i.e. at $\sim$ 7500 Å in the observers frame) provides the ideal and obvious candidate for this broad absorption feature. The 2175 Å bump is the dominating spectral signature of dust in the interstellar medium (ISM) in the Milky Way and is often attributed to small graphite grains processed by star formation (Gordon et al., 1997; Draine, 2003; Duley & Lazarev, 2004). However, the nature of the bump is not totally clear. Its strength varies along different sight lines in the Milky Way (Cardelli et al., 1989). Different size distributions or different chemical compositions could be the origin of this variation (Natta & Panagia, 1984).

At high redshift, the search for the 2175 Å feature has always been very difficult. It was never clearly detected in single objects, for instance, in damped Ly-α systems (DLAs) along quasar (QSO) sight lines. The presence of the bump was excluded from a composite spectrum of 37 Ca II and Mg II absorbers from Sloan Digital Sky Survey (SDSS) QSOs (Wild et al., 2006), but detected in a combined spectrum of 18 galaxies at $1 \leq z \leq 1.5$ with intermediate-age stellar populations (Noll et al., 2007). Further detections outside the Local Group have been suggested e.g. for GRB 050802 (Schady et al., 2007) at $z = 1.71$ (Fynbo et al., 2005) and a galaxy at $z = 0.83$ (Motta et al., 2002). Despite the presence of strong metal absorption (Savaglio & Fall, 2004; Berger et al., 2006; Fynbo et al., 2006) and the depletion of refractory elements (Savaglio, 2006) it has not been detected in spectra of previous bursts. The afterglow of GRB 070802 shows the clearest presence of the 2175 Å dust feature at a high redshift so far, where it is detected with GROND broad-band photometry and VLT spectroscopy as shown in Fig. 5 in Fynbo et al. (2007) and Eliasdottir et al. (in preparation).

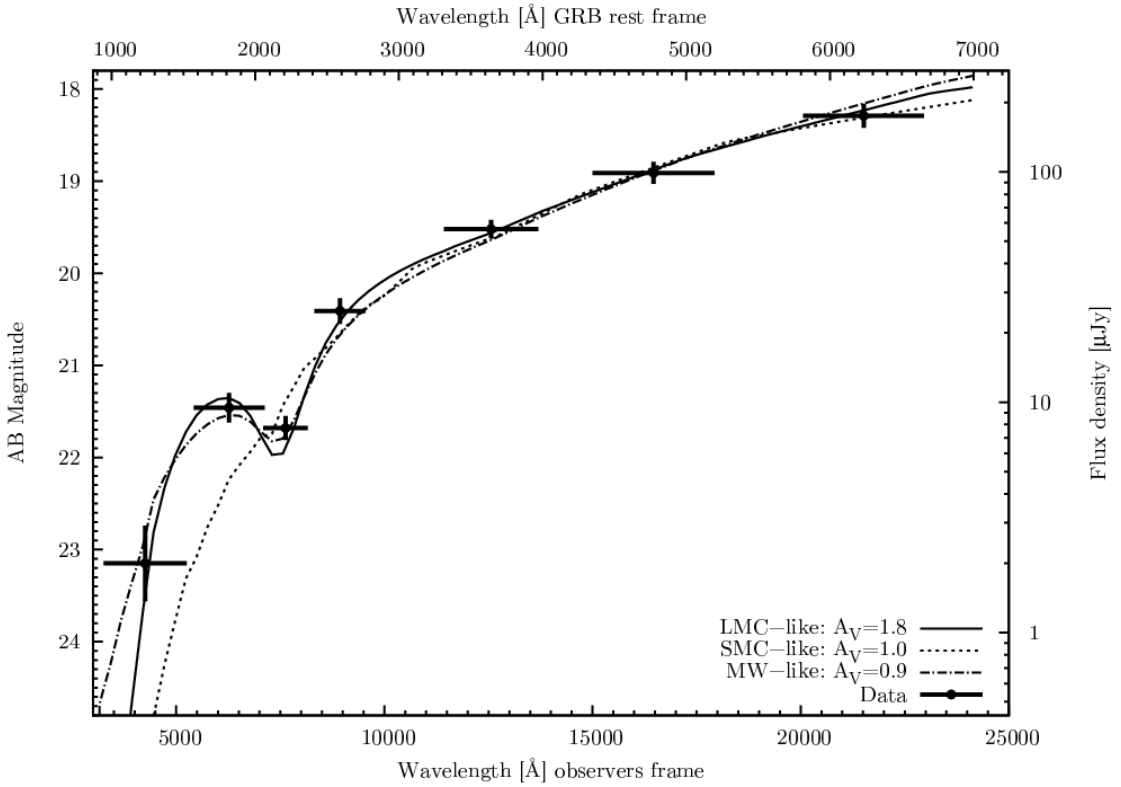

Figure 3.3 Spectral Energy Distribution of the afterglow of GRB 070802 in the GROND filter bands. The data were obtained simultaneously in all colors between $T_0 + 1.5$ ks and $T_0 + 3.6$ ks post burst. The shape of the SED can be well reproduced by LMC and MW extinction models. A broad extinction feature is detected in the GROND i' band at 7630 Å central wavelength, which we relate to the 2175 Å dust feature in the host at redshift 2.45. Depending on the used model, the best fit extinction varies between $A_V^{\rm host} = 0.9$ mag (MW) and 1.8 mag (LMC).

We can estimate the column density of different metals along the sight line for GRB 070802, following the approach described in Savaglio (2006). The $A_V^{\rm host}$ is directly proportional to the dust column density. The dust column density is also proportional to the total metal column density. For instance, in a galaxy with MW- or LMC-like visual extinction, $A_V^{\rm host} = 0.5$ mag or 0.4 mag is expected for a column density of oxygen of $\log(N_{\rm O}) = 17.7$ or 17.1, respectively. Assuming a constant dust-to-metals ratio, our $A_V^{\rm host} = 0.9$ mag for MW or 1.8 mag for LMC gives $\log(N_{\rm O}) = 18.0$ and 17.8. This is the oxygen column density in gas form, i.e. assuming that the amount of oxygen locked into dust grains is marginal. In the Galactic ISM, oxygen in dust grains is negligible, but is up to about 40% in the cool gas (Savage & Sembach, 1996). If we assume this kind of dust depletion, then the total oxygen column density is $\log(N_{\rm O}) = 18.4$ or 18.2, for MW or LMC, respectively. Using the standard nomenclature for hydrogen absorption at X-ray energies and assuming solar metallicity, we conclude that the column density of hydrogen $\log(N_{\rm H})$ is about 21.7 or 21.5, for MW or LMC dust, respectively.

Combined Optical/NIR and X-ray Analysis

The XRT spectrum including all data from 150 s to 405 ks post burst with a total exposure time of 56 ks is compatible with an absorbed power law with a photon index $\Gamma = 2.1 \pm 0.3$ (reduced $\chi^2 = 0.7$ for 15 d.o.f.). The foreground hydrogen column density was frozen at the Galactic value of 3×10^{20} cm^{-2} (Dickey & Lockman, 1990). The best fit for $N_{\rm H}$ at $z = 2.45$ is $1.60^{+1.20}_{-1.10} \times 10^{22}$ cm^{-2}, which corresponds to a total gas plus dust oxygen column density of $N_{\rm O} = 7.2^{+5.4}_{-5.0} \times 10^{18}$ cm^{-2}. Given the large uncertainties, this is consistent with the values estimated in the previous section.

The GROND optical/NIR and XRT X-ray data can be fit together to constrain the broadband afterglow spectrum. We fit the data using a power law with absorption in the X-ray regime and extinction in the optical/NIR regime using the XSPEC package (Arnaud, 1996). Unfortunately, there is no simultaneous early coverage by XRT and GROND, as there is a gap in the XRT coverage of GRB 070802 from 911 s to 4.2 ks (Fig. 3.2). Therefore XRT data from 460 s to 5 ks with a total exposure time of 1.3 ks and GROND data from 1.5 to 3.6 ks after trigger were selected for the joint fit. These intervals were chosen because they are the closest in time while the source is still bright and do not include the steep decay in the early XRT light curve, see Fig. 3.2 and Immler et al. (2007).

The XRT spectrum alone from 460 s to 5 ks post burst is compatible with the total spectrum with a power-law photon index of 1.9 ± 0.4, although $N_{\rm H}$ is no longer well constrained due to poorer statistics.

The combined GROND and XRT SED from 2.2 μm K_S to $\sim$4 keV was fit by a single power law with reddening E_{B-V} and $N_{\rm H}$ Galactic foreground values from Schlegel et al. (1998) and Dickey & Lockman (1990) (0.026 and 3×10^{20} cm^{-2}, respectively) and by extinction in the host at $z = 2.45$. There were insufficient statistics above 4 keV in the XRT band to extend the fit to higher energies. The optical/NIR data were modelled using the *zdust* XSPEC model, where the extinction in the host is obtained using MW, LMC and SMC reddening laws with values of R_V of 3.08, 3.18 and 2.93 respectively, where $A_V = E_{B-V} \times R_V$ (Pei, 1992). As shown in Fig. 3.3, the GROND data

alone is well described by MW and LMC models. The additional absorption in the soft X-ray band was modelled by an absorbing column at $z = 2.45$.

In the broadband fits we are mainly interested in the power-law index between the GROND and XRT bands. The combined optical/NIR and X-ray data are well described by a single power law with a photon index of 1.91 ± 0.04 (reduced χ^2 of 1.36 for 12 d.o.f.) using the MW extinction model with E_{B-V} of 0.35 ± 0.04. The $N_{\rm H}$ at $z = 2.45$ is not well constrained by the fit. Similar values of the power-law index and E_{B-V} are achieved using the LMC and SMC extinction curves. The results of the zdust and single power-law models are presented in Table 3.4 with the MW yielding the best fit.

To test for a cooling break, a broken power law with extinction and soft X-ray absorption was also fit to the data. Here the high energy photon index Γ_2 was linked to Γ_1 via $\Gamma_2 = \Gamma_1 + 0.5$ as expected in the fireball model. The value of the break energy was constrained to lie between the optical and X-ray bands and the best fit photon indices for the low and high energies were $\Gamma_1 = 1.61 \pm 0.05$ and $\Gamma_2 = 2.11$ respectively. The reduced χ^2 for this fit is 1.47 for 11 d.o.f for the MW extinction curve, 2.40 for 11 d.o.f for LMC and 3.5 for 11 d.o.f for SMC. The fit parameters E_{B-V} and the low energy power-law index are presented in Table 3.4.

The broadband model without a break provides a better fit to the data, however the difference in the reduced χ^2 parameters of the fits is not conclusive. The single power law implies that the cooling break is redwards the GROND bands at this time, which would be surprisingly early after the explosion. We caution that the GROND and XRT data are not simultaneous.

We also fit a late time SED using the XRT data 50 to 196 ks post burst with the GROND data obtained in the JHK_S band from 86 to 96 ks. The best fit model has a power-law slope of 2.0 ± 0.2, so the data are still compatible with the early time single power-law model, but we are not able to distinguish between a single and broken power-law fit. We do not find evidence for a cooling break between the NIR and X-ray data.

3.4 Conclusions

The optical/NIR afterglow light curve of GRB 070802 can be explained using two models: a combined reverse - forward shock model, and a single forward shock model with a superimposed emission component at peak brightness. Due to the fact that the afterglow peak is heavily delayed compared to the duration of the burst, it is very likely that the increase in brightness in the early light curve is related to the onset of the afterglow as proposed for GRB 060418 and GRB 060607A (Molinari et al., 2007). Using an analogue analysis for GRB 070802, we derive an initial bulk Lorentz factor in the jet of around $\Gamma_0 \approx 160 \left(\frac{E_{53}}{\eta_{0.2} n}\right)^{1/8}$ for an ISM environment. The steep rise of the early light curve favors an homogeneous over a wind-shaped circumburst medium. The ground-based observations of the optical/NIR afterglow of GRB 070802 were fast enough to detect an early brightening of the afterglow. Further rapid follow-up campaigns may establish whether this rapid rise is a generic feature of GRB afterglow light curves.

Table 3.1. Secondary standards in the GRB field in the GROND filter bands used during the calibration

Identifier	g' mag	r' mag	i' mag	z' mag	J mag	H mag	K_S mag
A	22.42 ± 0.05	20.71 ± 0.04	19.26 ± 0.04	18.50 ± 0.04	16.98 ± 0.06	16.55 ± 0.06	16.09 ± 0.08
B	16.33 ± 0.07	15.89 ± 0.03	15.78 ± 0.03	15.65 ± 0.03	14.81 ± 0.05	14.59 ± 0.05	14.42 ± 0.06
C	15.47 ± 0.05	14.98 ± 0.03	14.86 ± 0.03	14.72 ± 0.03	13.87 ± 0.05	13.61 ± 0.05	13.43 ± 0.06
D	20.07 ± 0.06	18.76 ± 0.04	18.23 ± 0.04	17.92 ± 0.04	16.72 ± 0.07	16.19 ± 0.07	15.74 ± 0.09
E	15.70 ± 0.05	14.62 ± 0.03	14.17 ± 0.03	13.87 ± 0.03	12.71 ± 0.05	12.61 ± 0.05	11.99 ± 0.06

Table 3.2. Parameters of the generic light curve fit to the $r'z'JHK$ band

Model	α_1^r RS rise index	α_2^r RS decline index	α_1^f FS rise index	α_2^f FS decline index	t_1 [s]	s^f Break sharpness
Combined RS + FS	3.16 ± 0.33	-2.66 ± 0.96	3.12 ± 1.49	-0.63 ± 0.14	2181 ± 107	3.15 ± 2.16
Single FS	—	—	3.56 ± 0.36	-0.68 ± 0.04	1830 ± 51.9	2.48 ± 0.72

A broadband fit of GROND and XRT data is compatible with a single power-law spectrum with photon index 1.91 ± 0.04, suggesting the cooling break being redwards of the GROND bands at the start of the observations at ∼1.2 ks post burst. The late-time photon index from NIR to X-rays is still comparable with the early time power law, indicating no time evolution of the spectrum during our observations.

The observed SED from g' to the K_S band can be well reproduced with LMC and MW extinction models. A broadband absorption feature in the GROND i' band with a central wavelength of 7630 Å is unquestionably required to explain the observed SED. The redshifted 2175 Å feature in the host galaxy of the burst at $z = 2.45$ known from MW and LMC extinction models provides the ideal candidate. Depending on the model the best fit extinction ranges from $A_V^{host} = 0.9$ mag for MW-like dust absorption to $A_V^{host} = 1.8$ mag for LMC dust. The amount of extinction is significantly larger than estimated for previous bursts (Kann et al., 2006; Schady et al., 2007; Kann et al., 2008). Pre-*Swift* bursts have shown a correlation of decreasing extinction with increasing redshift (Kann et al., 2008). However, there might be a strong instrumental bias, as fast and simultaneous optical-to-NIR follow-up observations for a large GRB sample are missing. The GROND instrument, with its unique optical and NIR capabilities, is a powerful tool which might remove this bias. GRB 070802 was the first burst for GROND occurring during nighttime and revealed significant amount of dust in its host galaxy, indicating that at least a good fraction of the UVOT dark burst is due to intrinsic extinction in the GRB host galaxy. Future observations will help to quantify the amount of highly extinguished bursts and may help to solve the mystery of dark bursts.

Table 3.3. Parameters of the individual fits to the $r'z'JHK$ bands.

Model	Parameter	r'	z'	J	H	K_S
Combined RS + FS	F_r^0 [μJ]	14.7 ± 0.7	30.9 ± 1.6	102 ± 2.5	163 ± 3.1	365 ± 11.0
Combined RS + FS	F_f^0 [μJ]	4.3 ± 0.7	9.7 ± 1.0	33.1 ± 1.6	46.5 ± 2.1	135 ± 10.9
Combined RS + FS	reduced χ^2/d.o.f.	0.64/5	0.98/7	1.80/18	1.10/15	1.53/18
Single FS	F_f^0 [μJ]	10.2 ± 0.6	21.8 ± 0.9	70.6 ± 1.0	104 ± 2.0	278 ± 7.6
Single FS	reduced χ^2/d.o.f.	0.62/3	0.66/5	0.98/7	0.67/7	0.80/7

Table 3.4. Broad band spectral fits to the GROND and XRT data using XSPEC.

Extinction Model	Power law	E(B-V)	Photon Index	χ^2/d.o.f
MW	Single	0.35±0.04	1.91±0.04	1.36/12
MW	Broken	0.41±0.04	1.61±0.05	1.47/11
LMC	Single	0.35±0.04	1.92±0.03	2.13/12
LMC	Broken	0.39±0.04	1.61±0.05	2.40/11
SMC	Single	$0.34^{+0.04}_{-0.03}$	$1.90^{+0.03}_{-0.04}$	3.2/12
SMC	Broken	$0.34^{+0.04}_{-0.02}$	1.61±0.03	3.5/11

Chapter 4

Correlated Optical and X-ray Flares in the Afterglow of XRF 071031 [1]

ABSTRACT

We present a densely sampled early light curve of the optical/near-infrared (NIR) afterglow of the X-ray Flash (XRF) 071031 at $z = 2.692$. Simultaneous and continuous observations in seven photometric bands from g' to K_S with GROND at the 2.2 m MPI/ESO telescope on LaSilla were performed between 4 minutes and 7 hours after the burst. The light curve consists of 547 individual points which allows us to study the early evolution of the optical transient associated with XRF 071031 in great detail. The optical/NIR light curve is dominated by an early increase in brightness which can be attributed to the apparent onset of the forward shock emission. There are several bumps which are superimposed onto the overall rise and decay. Significant flaring is also visible in the *Swift* X-Ray Telescope (XRT) light curve from early to late times. The availability of high-quality, broadband data enables detailed studies of the connection between the X-ray and optical/NIR afterglow and its color evolution during the first night post burst. We find evidence of spectral hardening in the optical bands contemporaneous with the emergence of the bumps from an underlying afterglow component. The bumps in the optical/NIR light curve can be associated with flares in the X-ray regime suggesting late central engine activity as the common origin.

4.1 Introduction

Major progress in the understanding of the X-ray and optical afterglow light curves of Gamma-ray Bursts (GRBs) and the softer X-ray Flashes (XRFs) has been made since the launch of the *Swift* satellite (Gehrels et al., 2004) and the rapid follow-up data provided by the X-Ray Telescope (XRT, Burrows et al., 2005b) and Ultra-Violet Optical Telescope (UVOT, Roming et al., 2005). However, access to the longer wavelength afterglow is still somewhat limited to the brighter half of all detected

[1] T. Krühler, J. Greiner, S. McBreen, S. Klose, A. Rossi, P. Afonso, C. Clemens, R. Filgas, A. Küpcü Yoldaş, G. P. Szokoly and A. Yoldaş (2009), *Astrophysical Journal*, 697, 758

bursts. In contrast to the evidence of a generic X-ray afterglow light curve (Nousek et al., 2006), the few bursts with very early detected optical counterparts show a considerable variety. For instance GRBs 990123 (Akerlof et al., 1999) and 041219A (Blake et al., 2005; Vestrand et al., 2005; McBreen et al., 2006) have shown optical emission contemporaneous with the prompt phase of the burst. A significant delay in the apparent onset of the afterglow forward shock (FS) allowed ground-based optical/near infrared (NIR) telescopes to detect a rising component of the afterglows for, e.g., GRBs 030418 (Rykoff et al., 2004), 060418, 060607A (Molinari et al., 2007), 070802 (Krühler et al., 2008) and 071010A (Covino et al., 2008). A number of optical afterglows showed bumps superimposed onto the overall power-law decay in late epochs, which are generally interpreted as the signature of either inhomogeneities in the circumburst medium (e.g., GRB 050502A, Guidorzi et al., 2005) or late energy injections (e.g., GRB 021004, de Ugarte Postigo et al., 2005 or GRB 070311, Guidorzi et al., 2007).

The very early optical afterglow is of significant interest from a theoretical point of view and in particular how it relates to the flares and plateaus seen in many X-ray afterglow light curves (e.g. O'Brien et al., 2006). In the early phase, the color evolution is crucial to differentiate between different emission components. However, most of the rapid ground-based follow-up is obtained with robotic telescopes of small aperture size in white light or filter cycles. In both cases information about the spectral properties is absent or can only be obtained at relatively long times with respect to the dynamical time scale in the early evolution of GRB emission. The ambiguity between effects of a changing spectrum or a highly variable early light curve can only be addressed by systematic observations in different broadband filters as synchronous and rapid as possible. Comprehensive data sets of early optical afterglows were published, e.g., for GRB 021004 (Lazzati et al., 2002), GRB 030329 (Lipkin et al., 2004), GRB 061126 (Perley et al., 2008b), and the very bright GRB 080319B (e.g. Racusin et al., 2008) where the light curve is well sampled in time and frequency domains, suggesting that a standard jet break model alone cannot account for the increasing variety of features in a GRB or XRF afterglow.

Here we report on the optical follow-up of GRB 071031 at redshift 2.692 (Ledoux et al., 2007) using data obtained in seven broadband filters from g' to K_S with the multichannel imager GROND (Greiner et al., 2007a, 2008). Ground-based optical/NIR observations started at ~ 4 minutes after trigger, yielding one of the best sampled early optical light curves. In combination with the detailed X-ray observations provided by the XRT, this constitutes a multicolor light curve with spectral coverage from the NIR to the 10 keV XRT band.

4.2 Observations

4.2.1 *Swift*

The Burst Alert Telescope (BAT, Barthelmy et al., 2005) on-board the *Swift* satellite triggered on the long-soft GRB 071031 at T_0=01:06:36 UTC and immediately slewed to the burst (Stroh et al., 2007b). The BAT light curve shows a two-peaked structure starting at $T_0 - 10$ s and ending at T_0+180 s with a T_{90} of 180±10 s. The fluence in the 15 to 150 keV band is $(9.0\pm1.3)\times10^{-7}$ erg cm^{-2},

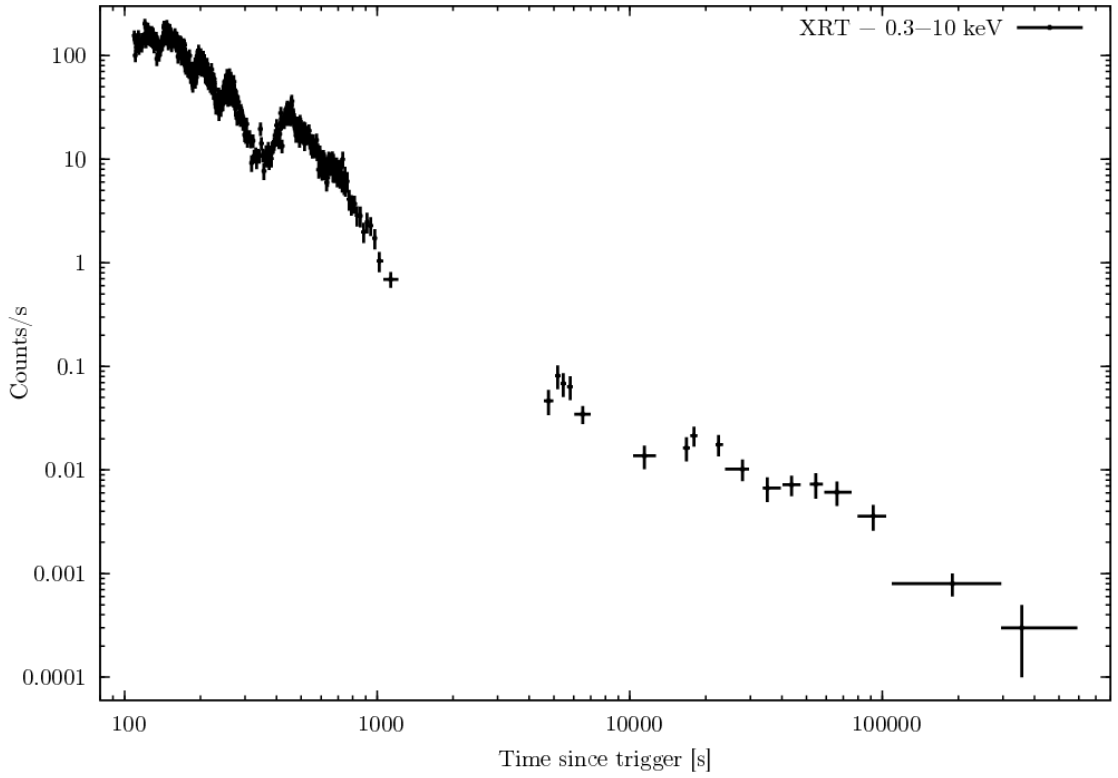

Figure 4.1 *Swift* XRT light curve of the X-ray afterglow of XRF 071031 obtained from the XRT light curve repository (Evans et al., 2007)

with a fluence ratio of 1.34 between the BAT 25-50 and 50-100 keV bands (Stamatikos et al., 2007). This is remarkably soft compared to conventional GRBs and qualifies GRB 071031 as an XRF according to the working definition of Sakamoto et al. (2008). The BAT spectrum of the first peak is well described with a single power law with a photon index of 2.26 ± 0.30 ($\chi^2 = 28.83$ for 36 degrees of freedom (d.o.f.)). This is well outside the normal range for the low energy index α but similar to the spectral index β above the break energy for a Band function (Band et al., 1993; Preece et al., 2000). The peak energy of the prompt emission spectrum must then be close to or below the BAT lower energy range of around 30 keV (see also McGlynn et al., 2005; Stamatikos et al., 2007). Therefore, GRB 071031 is designated as XRF 071031 hereafter.

The XRT began follow-up observations of the burst field 103 s after the trigger and detected an uncatalogued fading X-ray source at a position of R.A.(J2000)=$00^h\ 25^m\ 37^s.4$, decl.(J2000)=-58° 03′ 33″ with a refined 90% confidence error circle of 2.″0 radius (Stroh et al., 2007a). The early XRT light curve is dominated by significant amount of flaring with bright flares at around 120, 150, 200, 250 and 450 s. Also the late X-ray data exhibit rebrightenings at 5.5, 20 and 55 ks superimposed onto the overall power-law decay. The complete XRT light curve is shown in Fig. 4.1.

The X-ray spectra were obtained with the `xrtpipeline` tool using the latest calibration frames from the *Swift* CALDB and standard parameters. The spectra were fitted with the XSPEC package (Arnaud, 1996) and a foreground hydrogen column density at the Galactic value of $N_{\rm H} = 1.2 \times 10^{20}$ cm^{-2} (Kalberla et al., 2005).

The third instrument on-board *Swift*, UVOT started observations at $T_0 + 114$ s and found a transient source inside the XRT error circle in the white, v- and b-band filters. The UVOT data show an increase in the brightness of the afterglow of around 0.5 mag in the first few hundred seconds (Breeveld & Stroh, 2007).

4.2.2 GROND

GROND responded to the *Swift* GRB alert and initiated automated observations that started at 01:10:21 UTC, 3 minutes 45 s after the burst and continued until local Sunrise at 08:55:51 UTC. A predefined sequence of observations with successively increasing exposure times was executed and images were acquired in all seven photometric bands simultaneously. In total 84 individual frames in each $g'r'i'z'$ and 1510 images of 10 s exposures in JHK_S were obtained during the first night at airmasses between 1.1 and 2.4. The integration time of the CCD optical images scaled from 45 to 360 s according to the brightness of the optical afterglow. A variable point source was detected in all bands (Krühler et al., 2007) by the automated GROND pipeline (Küpcü-Yoldaş et al., 2008) and its absolute position is measured to R.A.(J2000)=$00^h\ 25^m\ 37^s.24$, decl.(J2000)=–58° 03′ 33.″6 compared to USNO-B reference field stars (Monet et al., 2003) with an astrometric uncertainty of 0.″3. Photometry and spectroscopy of the afterglow was also obtained by telescopes at Cerro Tololo Inter-American Observatory (CTIO Haislip et al., 2007; Cobb, 2007) and the Very Large Telescope (VLT), the latter yielding an UVES and FORS spectroscopic redshift of 2.692 (Ledoux et al., 2007; Fox et al., 2008).

Photometric calibration was performed relative to the magnitudes of 10 secondary standards in the field of XRF 071031, shown in Fig. 4.2 and Tab. 4.1. During photometric conditions, three spectrophotometric standard stars, SA114-750, SA114-656, and SA95-42, all primary Sloan standards (Smith et al., 2002), were observed with GROND. Observations of the GRB field followed within a few minutes. The magnitudes of the Sloan standards were transformed to the GROND filter system using their spectra and the GROND filter curves (Greiner et al., 2008). The obtained zeropoints were corrected for atmospheric extinction differences and used to calibrate the stars in the GRB field. An independent absolute calibration was obtained with respect to magnitudes of the SDSS and 2MASS stars within the standard fields obtained from the SDSS data release 6 (Adelman-McCarthy et al., 2008) and the 2MASS catalog (Skrutskie et al., 2006) with results consistent with the standard star calibration at the 0.03 mag level.

Optical and NIR image reduction and photometry were performed using standard IRAF tasks (Tody, 1993). For each frame a model of the point spread function (PSF) was constructed using brighter field stars, and fitted to the afterglow. The relatively large seeing between 2″ and 3″ together with the pixel scale of 0.″16 for $g'r'i'z'$ and 0.″60 for JHK_S resulted in an excellent spatial sampling of the PSF with statistical fit errors of the order of 0.2 % for $g'r'i'z'$ and 0.5 % for JHK_S . For consistency, we also performed standard aperture photometry with compatible results with respect to the reported PSF photometry. All data were corrected for a Galactic foreground reddening of $E_{B-V} = 0.012$ mag in the direction of the burst (Schlegel et al., 1998).

The stacking of individual images was done twice for different purposes. First, all available

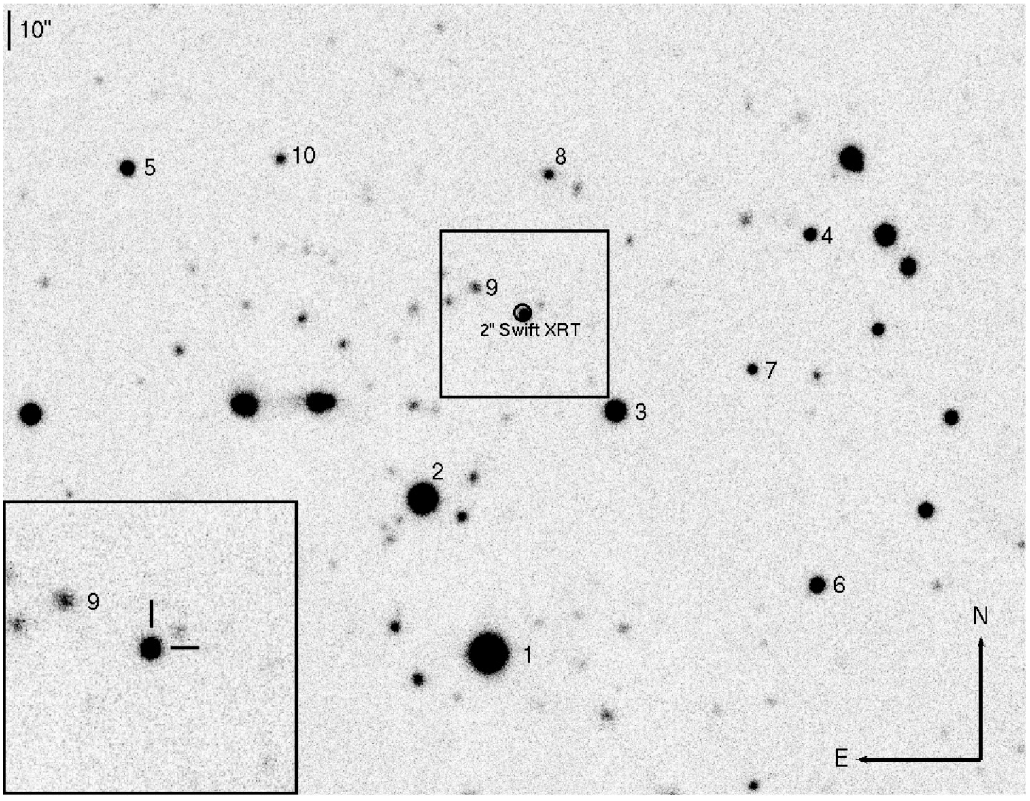

Figure 4.2 GROND r' band image showing the afterglow of XRF 071031 and the XRT error circle. The secondary standards used for calibration are labeled 1 to 10 and listed in Tab .4.1. The lower left corner shows a zoom in to the afterglow position.

data were used and individual frames were stacked until a statistical error in the PSF fit of around 0.1 mag was obtained. This resulted in 75 frames in each $g'r'i'$, 51 in z', 118 in J, and 76 in each H and K_S, yielding the multiwavelength light curve shown in Fig. 4.3. Second, only NIR data simultaneous to the optical integrations were selected, excluding the frames which were taken during the $g'r'i'z'$ CCD read out. The resulting NIR image stacks were used to derive the optical to NIR spectral energy distribution (SED).

4.3 Analysis

4.3.1 The Optical/NIR Light Curve

The multicolor light curve of XRF 071031 is complex and not described by smoothly connected power laws alone (Fig. 4.3). Evident in all colors is the initial increase in brightness up to ~ 1 ks, which smoothly turns over to a generic power-law decline with superimposed variations. In order to study small-scale irregularities at the highest possible signal-to-noise, a white-light curve was derived by combining all $g'r'i'z'$ CCD data (Fig. 4.4, upper panel), which are exactly synchronous by hardware setup. The NIR bands are excluded from this process due to the intrinsically larger photometric error which would serve only to increase the uncertainties in the summed data.

In order to better visualize the afterglow light curve, it is also presented differentiated in its native $\log - \log$ scale, i.e. $\delta(\log(F_\nu))/\delta(log(t))$, which directly represents the local power-law decay index $\alpha(t)$ (Fig. 4.4, lower panel). On a $\log - \log$ scale, the first derivative of a power law is a constant, so for a smoothly connected power-law rise and decay, one would expect a positive constant at early, turning into a negative at later times. Changes in the power-law index and deviations from the decay are clearly visible in this representation.

Without imposing an a priori model of the afterglow, Fig. 4.4 convincingly demonstrates that the overall trend of the light curve is well described by two smoothly connected power laws as introduced in Beuermann et al. (1999). In both panels of Fig. 4.4, however, the deviations from a Beuermann-like power-law rise and decay are clearly apparent. There are two features, which require either a superimposed component or a different parameterization of the intrinsic afterglow. The first and most obvious is the additional emission component in regions A,B,C,D shown in the upper panel of Fig. 4.4. This extra emission requires features intrinsic to the source or its environment to produce the observed flux excess with respect to the power law. The second is the steepening of the power-law decline after a rebrightening from region I over II to III in the lower panel of Fig. 4.4. However, there is so much variability within the light curve that the underlying afterglow cannot be established with high certainty.

The early rising component in the optical bands might be related to the deceleration of the FS by the circumburst medium, which happens when the swept up medium efficiently decelerate the ejecta. From the time of the light curve peak, the initial bulk Lorentz factor of the outflow Γ_0 can be constrained. Using the formalism outlined by Sari & Piran (1999), Panaitescu & Kumar (2000), and Molinari et al. (2007), Γ_0 is estimated to $\approx 90 \left(\frac{E_{53}}{\eta_{0.2} A^*}\right)^{1/4}$ in a wind shaped circumburst

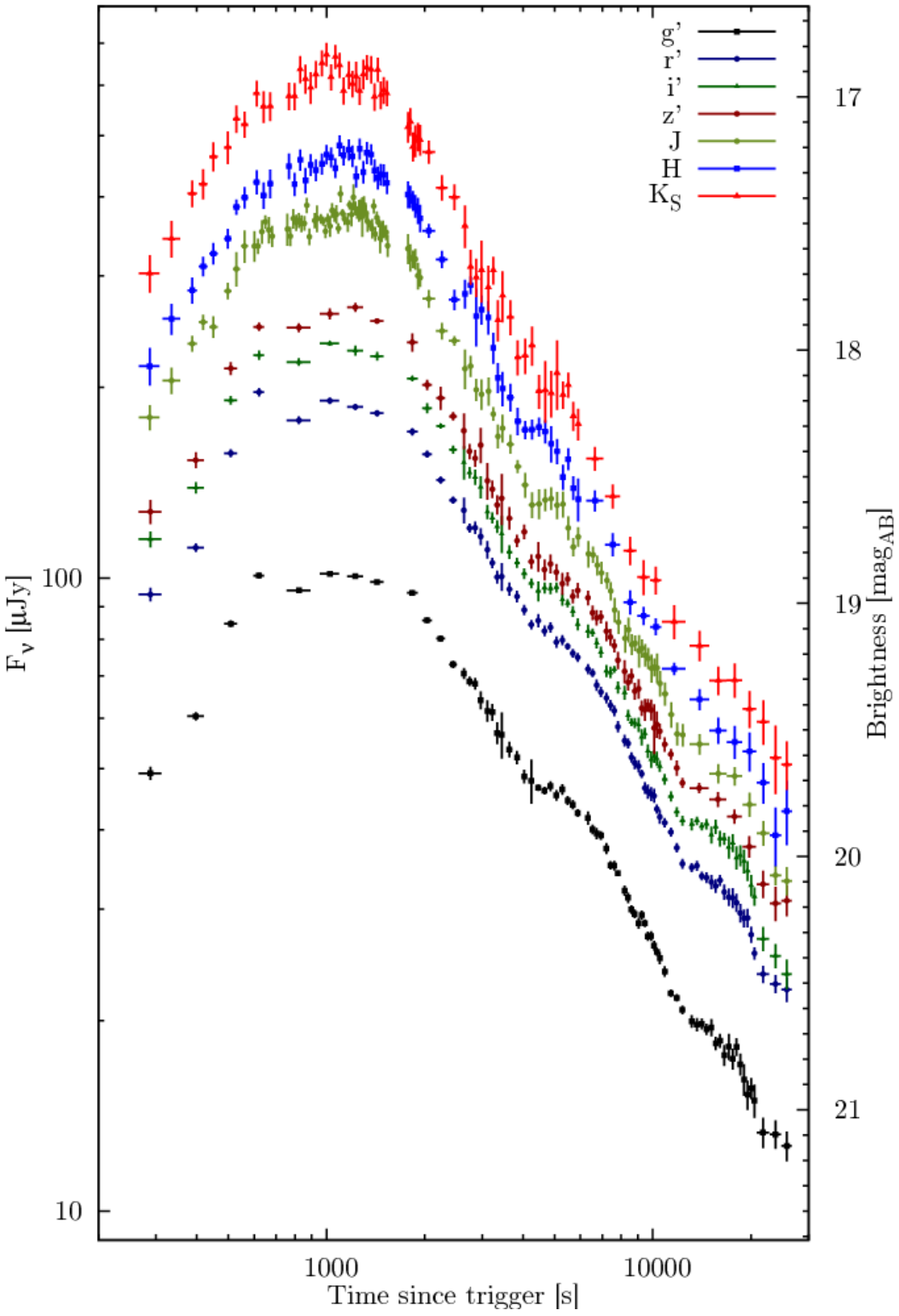

Figure 4.3 GROND optical and NIR light curve of the afterglow of XRF 071031 taken between ∼4 minutes and 7 hours after the trigger.

medium and to $\approx 200 \left(\frac{E_{53}}{\eta_{0.2} n}\right)^{1/8}$ for an ISM type environment, with a weak dependence on the uncertain parameters A^* being the normalized wind density, E_{53} the isotropic-equivalent energy released in γ-rays in 10^{53} erg, $\eta_{0.2}$ the radiative transfer efficiency normalized to 0.2 and n the ISM density in cm^{-3}. The slow rise with a power law index of $\sim$0.7 suggests a wind like environment, which would only be consistent with the closure relations for a very hard electron index (Dai & Cheng, 2001) of $p \sim$1.6 and $\nu_c < \nu$ using the spectral and temporal slopes in the late afterglow light curve $\alpha_{X,o} \sim 1$ and $\beta_X = 0.8 \pm 0.1$. The classical closure relations (e.g. Zhang & Mészáros, 2004), however, would favor an ISM environment in the slow cooling case with $\nu_m < \nu < \nu_c$ and a more canonical value of $p \sim 2.6$.

Alternatively, the initial rise could be the result of a structured outflow seen off-axis (e.g. Panaitescu et al., 1998). In the case of previous fast and slowly rising afterglow light curves, Panaitescu & Vestrand (2008) find an anticorrelation of peak flux in the R band $F_{\nu,R}$ and peak time t_p. K-correcting the afterglow to $z = 2$ to match the previous sample, we find that the optical/NIR light curve of XRF 071031 fits very well into this anticorrelation. In this interpretation, the slow rise would hint on a smooth angular structure of the outflow (Panaitescu & Vestrand, 2008).

Chromaticity around peak brightness was tested by comparing the optical/NIR SED before and after the total maximum. Apart from changes in the spectral index which can be attributed to the emergence of the bumps (see Sec. 4.3.4 and Fig. 4.7), there is no evidence for a change in the spectrum before and after the light curve peak. The time of the light curve maximum is not correlated with energy and all bands peak at a similar time within the measurement uncertainties. Such evolution would be expected if the main peak was caused by cooling of the ejecta after the prompt emission resulting in the shift of the characteristic synchrotron frequency $\nu_{\rm m}$ into the optical bands (e.g. Ziaeepour et al., 2008). In addition, a moving $\nu_{\rm m}$ through the optical bands is expected to cause a strong change from a positive to negative spectral index (e.g. Sari et al., 1998; Granot & Sari, 2002b). Neither effect is observed.

After correcting for Galactic foreground extinction, the SED from g$'$ to K_S was fit with a power law and dust reddening templates in the host at z=2.692. Using extinction templates from the Milky Way (MW), Large (LMC) and Small Magellanic Cloud (SMC) and supernovae-induced dust (Pei, 1992; Maiolino et al., 2004; Stratta et al., 2007) no signatures of dust extinction in the GRB host are evident down to 1σ confidence limits of $A_V^{\rm host} < 0.06$ mag (MW), $A_V^{\rm host} < 0.07$ mag (LMC), $A_V^{\rm host} < 0.05$ mag (SMC and SNe induced). Therefore, the effect of dust reddening is considered as negligible in the following analysis. The deviation from a power-law SED in the GROND g' band is consistent with Lyman-α absorption in the GRB host at $z = 2.692$.

4.3.2 The X-ray Afterglow Light Curve

In addition to the variable and densely sampled light curve in the GROND filter bands, the X-ray afterglow is bright and well covered by XRT observations. Similar to what is seen in the optical bands, the X-ray data show strong variability, and the underlying afterglow is poorly constrained. After excluding the very early data, where there are no GROND observations ($t - T_0 <$ 300 s), we fitted the remaining data using a similar procedure as used for the optical bands with a

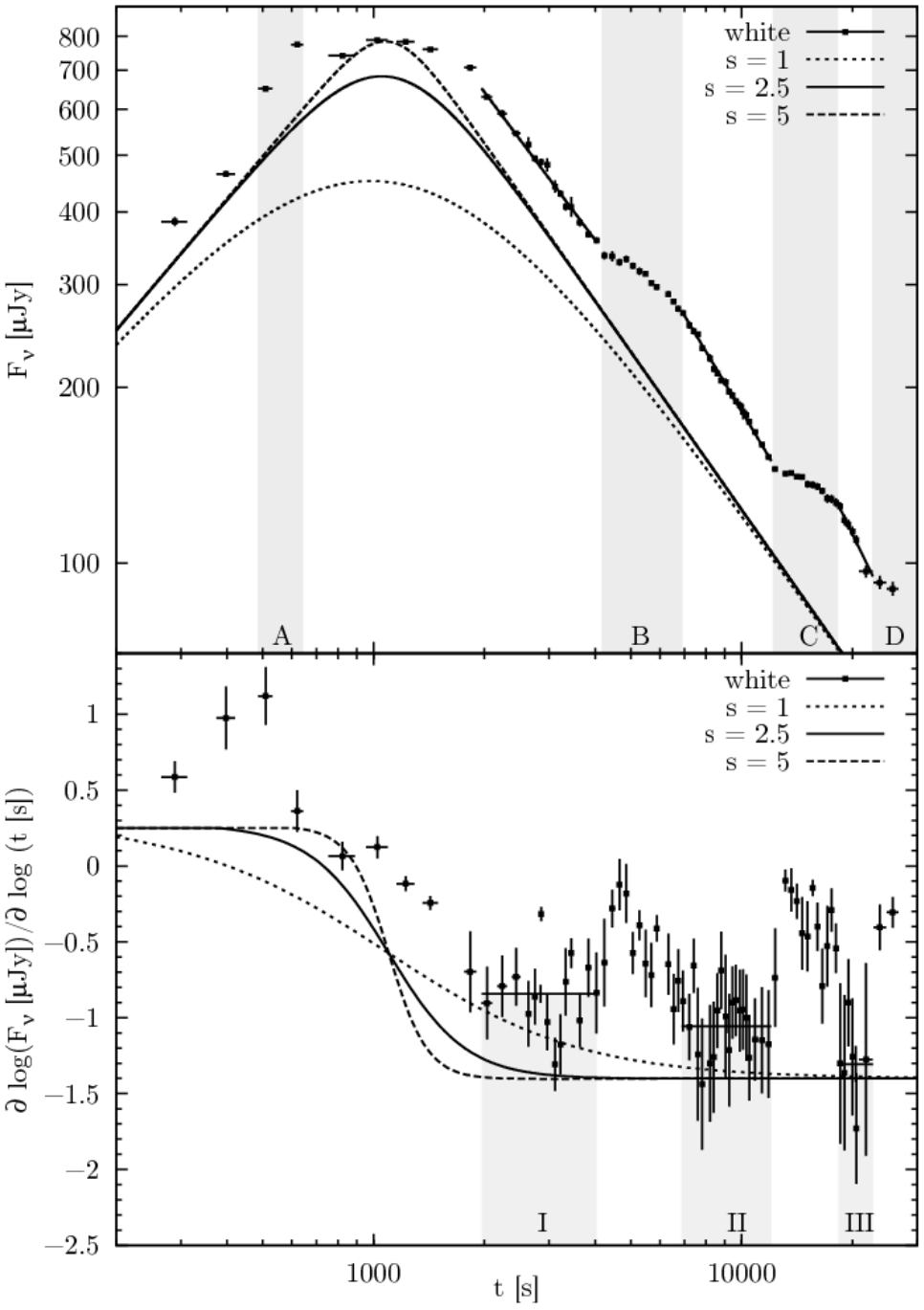

Figure 4.4 White light curve of the afterglow of XRF 071031 in the upper panel. A numerical differentiation of the data in the native log − log scale is shown in the lower panel. Regions of bumpiness are denoted with capital letters (upper panel), and the steeping of the power law in roman numbers (lower panel). The effect of a changing smoothness parameter s of the turnover is indicated by different lines in both panels.

combination of a smoothly connected power laws. Remarkably, the obtained late power-law index $\alpha_X = 0.99 \pm 0.12$ is compatible with the best fit from the GROND data $\alpha_o = 0.97 \pm 0.06$, providing additional evidence that the applied model fitting traces the underlying power-law decay of the afterglow reasonably well. The XRT light curve and the residuals to the power-law fits are shown in Fig. 4.5. After flaring episodes, the XRT light curve drops back to the power law, consistent with the rebrightenings observed in previous GRBs or XRFs (e.g. Burrows et al., 2005a; Romano et al., 2006b). All XRT light curve data have been obtained from the *Swift* XRT light curve online repository (Evans et al., 2007).

4.3.3 The Bumps

Both X-ray and optical/NIR data show significant variations from the typical power-law profiles at very early times. While this is observed in nearly 50% of all X-ray afterglows (e.g. Nousek et al., 2006), this is rarely seen so early in an optical light curve starting ∼400 s after the trigger.

We fitted the combined white light data with a canonical afterglow rise and decay with superimposed Gaussian profiles to account for the variations in the light curve. While this may not be the true physical model, it provides a good fit to the data, and represents the morphology of the bumps with adequate accuracy. For the very early optical data, where the time sampling of the light curve is naturally sparse, we used a cubic spline interpolation with equally spaced nodes in the native $\log - \log$ scale of the afterglow to constrain the fit. The data suggest the existence of three major and three small bumps: The three brighter ones, π_1 to π_3, which peak at 0.6, 6 and 18 ks, and three fainter ones, ξ_1 to ξ_3, all shown in the lower panel of Fig. 4.6. The first faint bump is only indicated by one data point and the last peak is not sampled by the observations due to the break of dawn. The fit shown in Fig. 4.6 has a $\chi^2_{red} = 1.05$ with 52 d.o.f.. The best fit parameters are presented in Tab. 4.2.

The typical time scale of variation for the optical bumps is $\langle \Delta T/T \rangle = 0.35 \pm 0.13$, where ΔT is calculated as the full width half maximum of the Gaussian, and have a relative flux increase with respect to the underlying afterglow of $\langle \Delta F/F \rangle = 0.29 \pm 0.18$. All bumps, which are reasonably sampled by our observations, have a change in the slope $\delta\alpha$ between 0.5 and 0.9, which can be directly deduced from the lower panel of Fig. 4.4.

Due to the faintness of the source, the late X-ray afterglow light curve is not equally well sampled as the optical and a detailed analysis is not possible in late epochs. There is, however, evidence for three X-ray flares ϕ_1 to ϕ_3 between 350 and 25000 s with synchronous optical coverage. To derive the morphology of the flares in the XRT light curve, we use a similar approach as for the optical bands for a direct comparison: an underlying continuum fitted with power laws and superimposed Gaussians to account for the evident flux excess which yields a reduced χ^2_{red} of 1.15 for 154 degrees of freedom. The best fit is shown in Fig. 4.5 and the corresponding parameters are reported in Tab. 4.3.

The X-ray flares are much stronger $\langle \Delta F/F \rangle = 1.28 \pm 0.28$ with respect to the underlying afterglow than the optical bumps. Comparing against a statistical sample of previous X-ray flares (Chincarini et al., 2007) shows that the flares observed in XRF 071031 populate a similar phase-

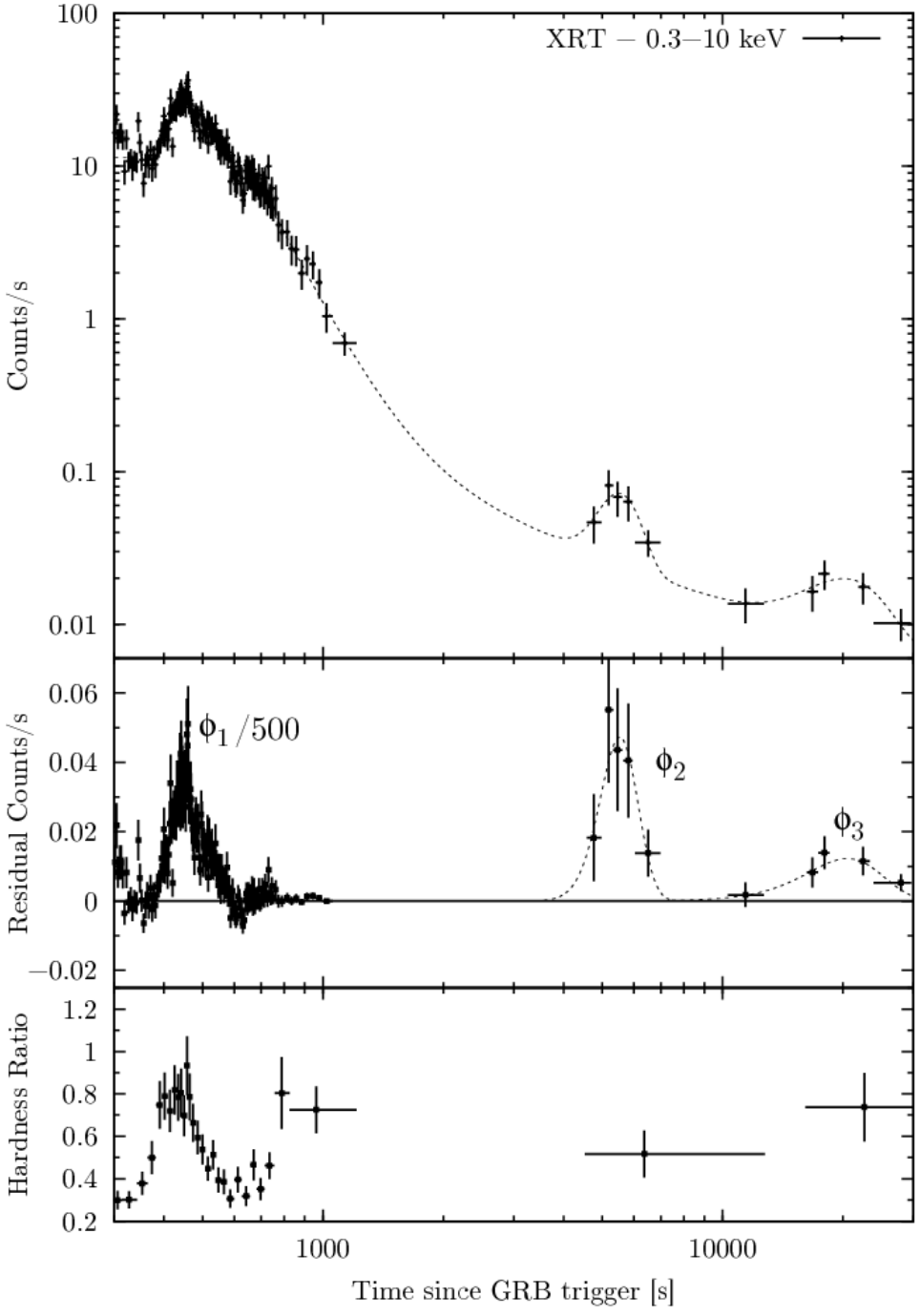

Figure 4.5 XRT light curve of the afterglow of XRF 071031 in the time domain simultaneous to the GROND data (top panel). The middle panel shows the residuals to the smoothly connected power-law fit, as well as their modeling using Gaussians. The residuals of the first flare have been scaled by 1/500. The bottom panel shows the hardness ratio of the 1.5-10 vs. 0.3-1.5 keV band.

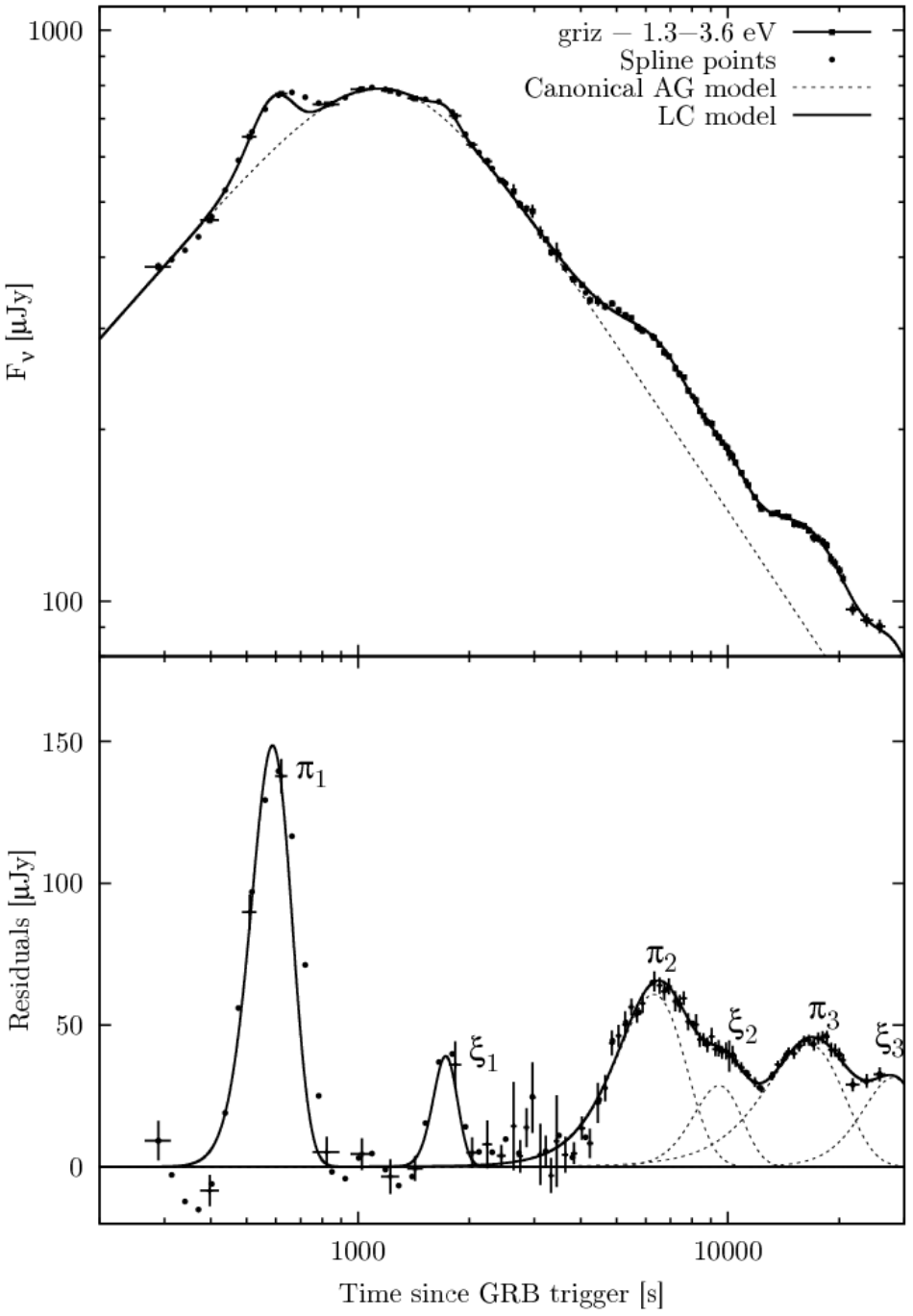

Figure 4.6 White light curve of the afterglow of XRF 071031 (upper panel, shown are the data and the cubic spline interpolation with equally spaced nodes in $\log(t)$). The data were fitted using the sum of a smoothly connected power law for the canonical afterglow (dashed line) and Gaussian profiles to account for the evident flux excess (solid line). The lower panel shows the residuals to the smoothly connected power law, as well their modeling by six Gaussians.

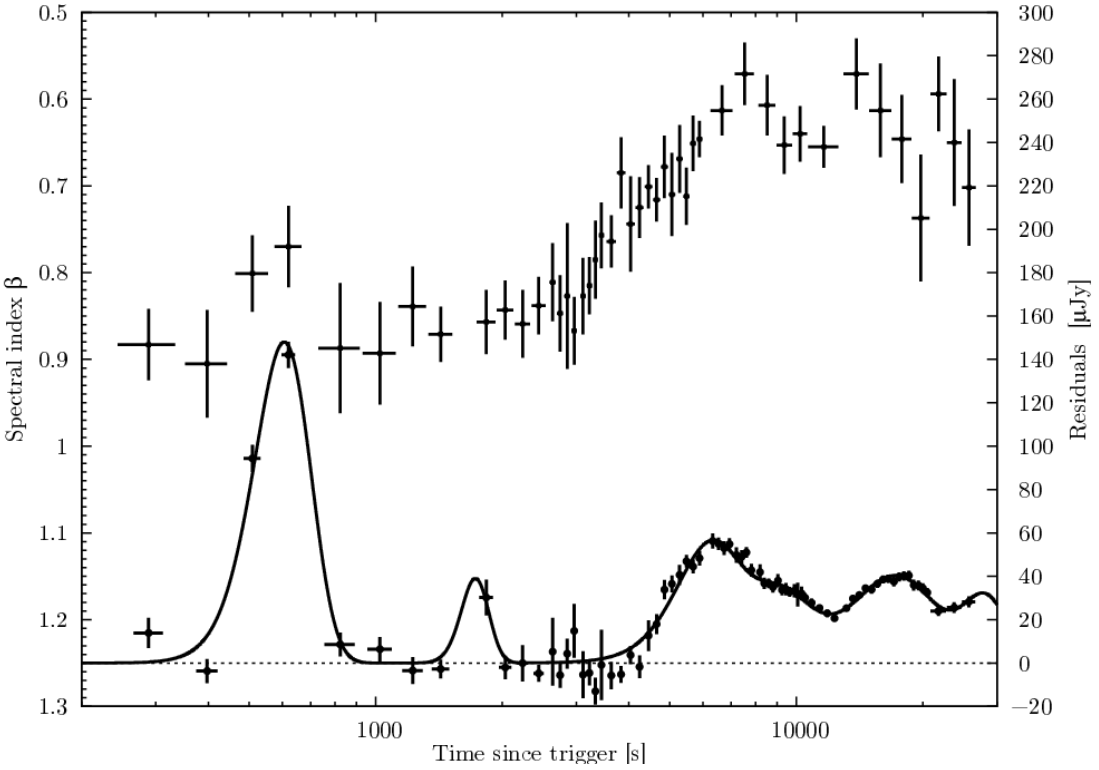

Figure 4.7 Color evolution of the optical/NIR afterglow of XRF 071031. A direct comparison of the spectral index β (upper points, - left y-axis) against the residuals to a fit of a canonical afterglow light curve model (lower points, - right y-axis). The plot clearly indicates a correlation of the spectral hardening and the rebrightening episodes in the light curve.

space region of $\Delta T/T$ versus $\Delta F/F$ and thus resemble the morphology of previous flares.

4.3.4 Spectral Evolution

The spectral index β, where $F_\nu \propto \nu^{-\beta}$ of the optical/NIR SED is observed to evolve with time (Fig. 4.7). Remarkably, the chromatic evolution is correlated with the residuals of the data against the light curve fits. Applying a standard statistical correlation analysis yields a correlation coefficient of ~ -0.73, and thus a null hypothesis probability of $\sim 10^{-6}$.

The correlation of spectral hardening and bumpiness suggests that this is an intrinsic feature of the emission component in the bumps, rather than the afterglow itself. In the ISM model for example, the cooling frequency $\nu_{\rm m}$ moving through the optical bands would identify itself by a spectral softening (Sari et al., 1998), in contrast to the observations. A hardening of the spectrum would be expected in a wind-like environment (Granot & Sari, 2002b) with a change in the spectral index of 0.5. The observed change (see Fig. 4.7) is ~ 0.2 and therefore not compatible with a cooling break passing the optical bands also in the wind model.

In addition to the observed chromatic evolution in the optical bands, also the X-ray data show strong spectral changes throughout the observations. This is already indicated by the evolving hardness ratio of the two XRT bands (1.5-10 keV over 0.3-1.5 keV), shown in the lowest panel of

Fig. 4.5.

This evolution becomes more evident, when including individual early flares from Fig. 4.1 into the analysis. For each flare in Tab. 4.4, a spectrum was extracted and fitted by single and broken power-law models. The rest-frame column density $N_{\rm H}$ at $z = 2.692$ was obtained by fitting the late photon counting data and found to be consistent with zero within a 1σ confidence level. Combined with the negligible $A_{\rm V}$ from the optical data and assuming a constant $N_{\rm H}$ in the burst environment, the intrinsic $N_{\rm H}$ is neglected in the spectral fits. There is strong evidence that the flares are better modelled by broken rather than single power laws as shown in Tab. 4.4, which is similar to flares seen in, e.g., GRB 051117A (Goad et al., 2007), GRB 050713A (Guetta et al., 2007), and 061121 (Page et al., 2007).

From the X-ray data alone, there is evidence for a break in the spectrum in the 1 keV range for the early flares. This is consistent with the result of Butler & Kocevski (2007), who find that the peak energy of the flare spectrum $E_{\rm P}$ crosses the X-ray bands on a typical time scale of 10^2 to 10^4 s. Combining the excess flux in the optical bands for π_1 and the X-ray spectrum in ϕ_1, the spectrum can be constrained over a broad energy range. For the optical bands the dominant emission process is FS emission even at early times, and the afterglow model fitting was used to disentangle the different components. In this way estimates of the flux attributed to the flare component can be obtained. As shown in Fig. 4.8, the broadband spectrum of the first flare is reasonably well (χ^2=129 with 114 d.o.f) described by a Band function (Band et al., 1993) with an $E_{\rm P}$ of 1.79 ± 0.59 keV and a very reasonable set of parameters $\alpha = -0.78 \pm 0.03$ and $\beta = -1.92^{+0.11}_{-0.17}$ as compared to the BATSE sample (Kaneko et al., 2006).

We caution that this fit implicitly assumes that the excess emission seen in the optical bands is correlated with the X-ray flare and the applied model of the underlying FS emission traces the afterglow reasonably well. As the fundamental shape of the afterglow can be different than the empirical Beuermann profile, this might introduce significant systematic errors in the analysis. Additionally, an underestimated or even varying column density $N_{\rm H}$ would change the soft X-ray absorption and thus the overall broadband and X-ray fits.

For the later flares the different components attributed to FS and flare emission cannot be deconvolved with high certainty. The X-ray data are faint and affected by the underlying afterglow, and the excess flux in the optical bands is strongly dependent on the parameters of the light curve fitting. In particular, there is a strong ambiguity between the sharpness of the break and the light curve decay. Given the large uncertainties, the optical color attributed to later bumps is compatible with the slope of the lower energy part of the Band function found for the first flare. $E_{\rm P}$, however, can no longer be constrained, but it is interesting to speculate that a similar Band function with an $E_{\rm P}$ between the optical and X-ray bands would account for the observed excess fluxes.

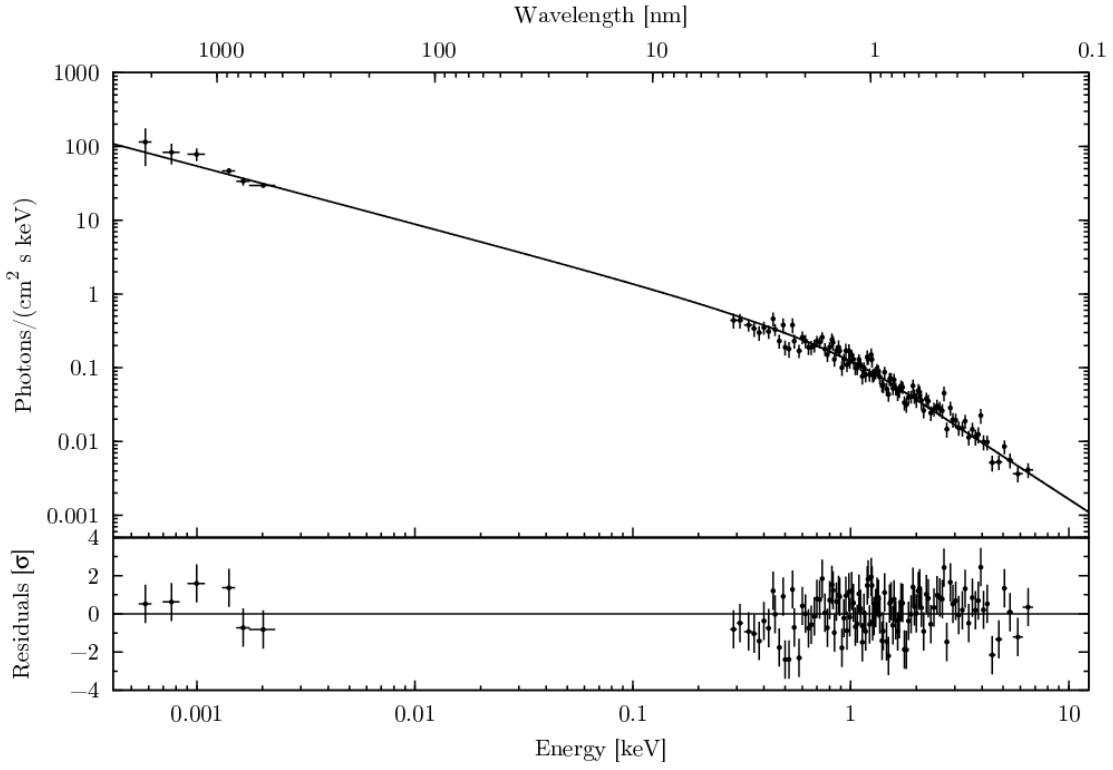

Figure 4.8 Broadband spectrum of the first flare π_1 with simultaneous optical and X-ray coverage. The data are fitted by a Band function with $E_{\rm P} = 1.79 \pm 0.59$ keV, $\alpha = -0.78 \pm 0.03$, and $\beta = -1.92^{+0.11}_{-0.17}$.

4.4 Discussion

4.4.1 The Likely Cause of the Flares

Previously, bumps or flares in optical afterglow light curves have been reproduced using either a superimposed reverse shock component for early flares, inhomogeneities in the circumburst medium (e.g. Wang & Loeb, 2000), or the angular distribution of the energy in the jet (patchy shell model; e.g. Kumar & Piran, 2000) or late energy injection by refreshed shocks (e.g. Rees & Mészáros, 1998) for later flares. However, a clear discrimination in the individual previous cases was not possible due to the lack of simultaneous coverage in broad wavelength ranges.

Although we cannot completely rule out a reverse shock component for the first bump, it seems likely that it is produced by the same mechanism as the later ones. After subtracting the rising power law, the decline of the first bump can be fitted with a power law of index ~ -7. This would be surprisingly fast for a reverse shock, which is expected to decline with $\sim t^{-2}$ in the basic fireball model (e.g. Nakar & Piran, 2004) and not faster than $\sim t^{-3}$ for more complicated models (Kobayashi & Sari, 2000). The fact that the morphology is comparable to the later bumps additionally hints on a common origin. Therefore, we try to account for all bumps with as few assumptions as possible, thus searching for a phenomenological explanation for all bumps observed.

Recently, Nakar & Granot (2007) found that density jumps in the circumburst medium cannot account for the majority of fluctuations previously observed in GRB afterglow light curves. Only large contrasts in the circumburst medium density are able to produce bumps with a change in the temporal power-law decay index $\delta\alpha \approx 1$ in the light curve with a long transition time, which scales linearly with contrast. Thus, signatures of inhomogeneities in the circumburst medium in the optical light curve are expected to be smoother to what is observed.

A jet with inhomogeneities in the angular energy distribution produces episodic bumps when the cone of a relativistically beamed patch enters the field of the view of the observer (Zhang et al., 2006). Similar to refreshed shocks, these patches inject additional energy into the blastwave, the afterglow emission is boosted to a higher level and resumes the same power-law index as before the bump (Zhang & Mészáros, 2002b). A characteristic for rebrightenings due to patchy shells or refreshed shocks consequentially is a step like afterglow light curve. Given the steepening of the power law post bump (Fig. 4.4), this scenario seems inconsistent with the bumps observed in XRF 071031. We note, however, that the refreshed shock scenario can produce rebrightenings on relatively short time scales under certain conditions, where the light curve drops back to the initial decay (e.g. Guidorzi et al., 2007).

Although the morphology of the light curve and optical bumps in the GROND data might be explained within the framework of variable external density or energy dissipation in the FS, both the spectral evolution and the correlation with the X-ray data argue for an independent origin and a second emission component. A hardening of the spectral index for flares in an optical light curve is not unprecedented (Greiner et al., 2009a), and suggests a different emission than the generic afterglow FS. In addition, the first pronounced bump in the optical light curve is already observed during the rise of the afterglow at 600 s, when the apparent onset of the FS just started.

If all previously observed X-ray flares are due to the same physical process, it is very likely that they do not originate from external shocks that give rise to the afterglow emission, but from late time internal shocks (e.g. Burrows et al., 2005a; Zhang et al., 2006; Chincarini et al., 2007; Butler & Kocevski, 2007). Thus, X-ray flares seem to be produced by a similar mechanism as the prompt γ-rays, which are also caused by internal shocks in the standard model (Rees & Mészáros, 1992). Detailed analysis for GRB 050820A (Vestrand et al., 2006) showed that the optical emission contemporaneous with the prompt phase can be explained as the superposition of forward shock and emission correlated with the γ-rays. Similarly for XRF 071031, after subtracting the dominating FS in the optical bands, the flare spectrum from NIR to X-rays is well described with a Band function.

Remarkably, the optical bumps show features which have been previously observed in X-ray flares: a hardening of their spectra (e.g. Burrows et al., 2005a; Butler & Kocevski, 2007; Falcone et al., 2007; Goad et al., 2007) and a correlation of the duration with the time where the bump occurs, i.e. a roughly constant $\Delta T/T$ (Chincarini et al., 2007; Kocevski et al., 2007). They are, however, less pronounced than typical X-ray flares. Temporal analysis of the early data shows that the optical bump peaks significantly later than the X-ray flare. A hard to soft evolution of $E_{\rm P}$ which is found in the majority of all bright flares where a detailed spectral analysis is possible (e.g. Burrows et al., 2005a; Romano et al., 2006a; Perri et al., 2007; Falcone et al., 2007) provides a natural explanation for the time difference between the flare in the X-ray and optical wavelength range. Spectral lags and a broadening towards lower energies have been observed in a number of previous X-ray flares and the prompt emission (e.g. Norris et al., 1996; Romano et al., 2006b; Perri et al., 2007).

Based on the light curve fitting, the observed peak of the early optical flare is delayed by $\tau \sim 130$ s compared to the X-rays, which corresponds to 35 s in the bursts rest frame. As the temporal coverage of the optical light curve is sparse in the early time frame, this delay is strongly dependent on the assumed functional form of the afterglow and flare morphology, but in any case it is significantly longer than what is typically observed as spectral lags in the prompt phase. Typical values for prompt lags range from slightly negative (i.e. soft preceding hard bands) to several seconds for long lag GRBs (e.g. Norris et al., 2000; Gehrels et al., 2006; McBreen et al., 2008; Foley et al., 2008). The observed time difference in the case of XRF 071031, however, is based on entirely different energy ranges. In particular, the difference between hard and soft energy bands is around a factor of 10^3 for X-rays versus optical, while it is ~ 10 for BAT channels.

Combining bump morphology, color evolution, broadband spectrum and the temporal connection to the X-ray data as shown in Fig. 4.9, the most likely origin of the bumps in the optical/NIR light curve of XRF 071031 is the same as in the X-rays, namely the soft tail of emission correlated with late internal shocks.

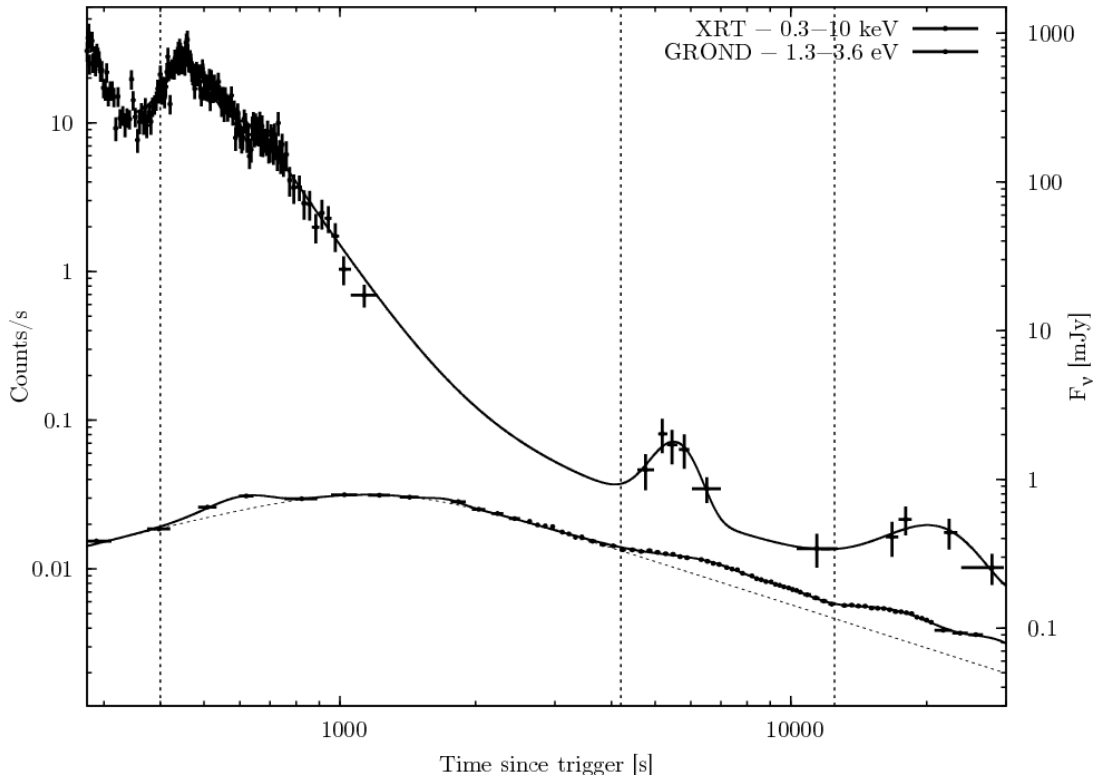

Figure 4.9 Combined plot of XRT light curve (crosses, left y axis) and GROND white light (dots, right y axis). The vertical dashed lines indicate the emergence of the bumps from the underlying optical afterglow emission.

4.4.2 Paucity of Detection of Correlated Early Optical Bumps and X-ray Flares

While a number of bursts have shown considerable variability in the optical bands during X-ray flares (e.g. Pandey et al., 2006; Boër et al., 2006; Page et al., 2007; Malesani et al., 2007), the early optical light curve is generally not as strongly affected as the X-rays by flaring episodes. The UVOT and ground-based robotic telescopes with their fast response provide a good sample of optical observations simultaneous with the XRT light curve. If the first optical bump and the first X-ray flare in XRF 071031 are correlated as suggested by the data, the signature of a typical X-ray flare in the optical light curve can be approximated with the ratio of absolute optical to X-ray peak flux obtained for XRF 071031.

GRB 060607A for example, showed significant X-ray flaring very early in the X-ray light curve with only marginally correlated optical emission (Ziaeepour et al., 2008). However, the afterglow was very bright, reaching ~ 14.3 mag in the r band (Nysewander et al., 2007). If the flare was described with a similar spectrum as in XRF 071031, the expected optical counterpart of the brightest X-ray flare is estimated to have a peak amplitude of ~ 200 μJy and could only be resolved with continuous photometric monitoring with a precision of at least 0.03 mag. Thus, if the emission in the flares is not strong enough with respect to the FS, a bright afterglow can easily outshine flare signatures in the optical bands even for very bright X-ray flares. In fact, GRB 061121 (Page et al., 2007) had simultaneous coverage with BAT, XRT and UVOT of the prompt emission with a peak flux density in the X-rays of ~ 15 mJy. Page et al. (2007) find that most of the flux is emitted in the γ-ray and X-ray bands, while the UVOT data only showed a relatively small increase in brightness.

4.5 Conclusions

The detailed light curve and spectral evolution of the afterglow of XRF 071031 showed several remarkable features. The most salient one is the achromatic early rise in brightness, resulting in a peak of the optical/NIR light curve at around 1 ks. The achromatic turnover from rise to decay suggests the apparent onset of the FS as its origin, due to either the increase in radiating electrons in the pre-deceleration phase or a structured outflow seen off axis. In the latter case the increase in brightness is caused by the deceleration of the shock, so that the relativistically beamed cone widens and gradually enters the sight line of the observer.

Superimposed onto the afterglow continuum emission are bumps which have a harder SED and appear in similar epochs in the optical/NIR as well as in the X-ray bands. Based on the GROND data collected for XRF 071031, we conclude that the variation in the light curve are most probably the optical counterparts of X-ray flares, and therefore directly connect variability in an optical light curve with the emergence of X-ray flares. Although emission from external shocks or a combination of different effects cannot be completely ruled out, an internal origin seems to nicely account for the majority of observations: the light curve shape and in particular the morphology of the bumps, the spectral hardening in the optical SED, the observed decrease in $E_{\rm P}$ from the prompt emission

Table 4.1. Secondary standards in the GRB field in the GROND filter bands from 1 to 10

Ra/Dec Deg [J2000]	g' mag	r' mag	i' mag	z' mag	J mag	H mag	K_S mag
6.4098/-58.0831	15.44 ± 0.02	14.55 ± 0.02	14.28 ± 0.02	14.13 ± 0.02	13.09 ± 0.04	12.55 ± 0.04	12.50 ± 0.06
6.4186/-58.0723	16.32 ± 0.02	15.73 ± 0.02	15.54 ± 0.02	15.43 ± 0.02	14.46 ± 0.04	14.07 ± 0.04	14.00 ± 0.06
6.3933/-58.0662	17.84 ± 0.03	17.32 ± 0.03	17.18 ± 0.03	17.10 ± 0.03	16.18 ± 0.04	15.94 ± 0.06	15.65 ± 0.07
6.3672/-58.0536	20.71 ± 0.05	19.33 ± 0.03	18.53 ± 0.03	18.13 ± 0.03	16.86 ± 0.05	16.41 ± 0.07	16.28 ± 0.08
6.4579/-58.0492	20.03 ± 0.04	18.90 ± 0.03	18.49 ± 0.03	18.31 ± 0.03	17.07 ± 0.05	16.68 ± 0.07	16.45 ± 0.08
6.3663/-58.0782	20.09 ± 0.04	18.62 ± 0.03	17.60 ± 0.03	17.13 ± 0.03	15.80 ± 0.04	15.30 ± 0.05	14.92 ± 0.06
6.3751/-58.0631	21.26 ± 0.05	20.13 ± 0.04	19.72 ± 0.04	19.52 ± 0.04	18.29 ± 0.07	17.87 ± 0.08	17.79 ± 0.10
6.4021/-58.0496	22.72 ± 0.10	20.85 ± 0.05	20.06 ± 0.05	19.65 ± 0.05	17.94 ± 0.06	17.35 ± 0.07	16.11 ± 0.08
6.4117/-58.0575	22.49 ± 0.08	21.21 ± 0.06	20.76 ± 0.06	20.51 ± 0.07	18.56 ± 0.07	17.78 ± 0.08	16.86 ± 0.10
6.4375/-58.0485	21.28 ± 0.05	20.77 ± 0.05	20.61 ± 0.05	20.59 ± 0.07	19.29 ± 0.09	18.91 ± 0.10	17.98 ± 0.15

Table 4.2. Parametrization of the excess flux in the GROND bands using Gaussians

Bump	T_{mid} [s]	$\Delta T/2$ [s]	Amplitude [μJy]	$\Delta T/T_{mid}$	$\Delta F/F$
π_1	587 ± 12	84 ± 18	149 ± 5	0.29 ± 0.06	0.24 ± 0.01
ξ_1	1726 ± 6	130 ± 4	39 ± 5	0.15 ± 0.01	0.06 ± 0.01
π_2	6302 ± 156	1648 ± 136	60 ± 5	0.52 ± 0.05	0.26 ± 0.02
ξ_2	9439 ± 377	1461 ± 254	29 ± 4	0.31 ± 0.06	0.18 ± 0.02
π_3	16505 ± 135	4013 ± 263	43 ± 2	0.49 ± 0.03	0.46 ± 0.02
ξ_3	28000	5000	32 ± 4	0.36	0.55 ± 0.03

to the flares, and the broadband flare spectrum from NIR to X-rays. The spectral similarities to the prompt phase strengthen the picture of X-rays flares as later and softer examples of the prompt emission due to internal shocks. This connection provides additional evidence that inner engine activity may last or be revived on a time scale of hours or days at least for some bursts.

Table 4.3. Parametrization of the excess flux in the X-ray bands using Gaussians

Bump	T_{mid} [s]	$\Delta T/2$ [s]	Amplitude [Counts/s]	$\Delta T/T_{mid}$	$\Delta F/F$
ϕ_1	459 ± 2	42 ± 2	14.5 ± 0.8	0.18 ± 0.01	1.36 ± 0.07
ϕ_2	5528± 85	604 ± 114	0.047 ± 0.01	0.22 ± 0.04	1.20 ± 0.20
ϕ_3	20507 ± 952	4557 ± 1088	0.012 ± 0.002	0.44 ± 0.10	1.28 ± 0.13

Table 4.4. Spectral fits to the XRT flares using XSPEC.

Flare	Times [s]	Model	Photon Index 1	Break energy [keV]	Photon Index 2	χ^2/dof
1	137 - 150	Single	$1.23^{+0.05}_{-0.05}$	-	-	323/131
1	137 - 150	Double	$0.72^{+0.09}_{-0.09}$	$1.84^{+0.17}_{-0.36}$	$1.85^{+0.12}_{-0.19}$	157/129
2	189 - 217	Single	$1.72^{+0.09}_{-0.05}$	-	-	180/85
2	189 - 217	Double	$1.14^{+0.14}_{-0.15}$	$1.26^{+0.16}_{-0.13}$	$2.20^{+0.13}_{-0.11}$	89/83
3	236 - 284	Single	$1.87^{+0.05}_{-0.05}$	-	-	146/74
3	236 - 284	Double	$1.23^{+0.19}_{-0.18}$	$1.07^{+0.16}_{-0.12}$	$2.39^{+0.17}_{-0.14}$	67/72
4 (Φ_1)	396 - 547	Single	$1.64^{+0.04}_{-0.04}$	-	-	172/110
4 (Φ_1)	396 - 547	Double	$1.26^{+0.19}_{-0.32}$	$0.98^{+0.22}_{-0.20}$	$1.88^{+0.08}_{-0.08}$	120/108

Chapter 5

The Bright Optical/NIR Afterglow of the Faint GRB 080710 - Evidence of a Jet Viewed Off-axis [1]

ABSTRACT

We investigate the optical/near-infrared light curve of the afterglow of GRB 080710 in the context of rising afterglows. Optical and near-infrared photometry was performed using the seven channel imager GROND and the Tautenburg Schmidt telescope. X-ray data were provided by the X-ray Telescope onboard the *Swift* satellite. We construct an empirical light curve model using the available broadband data, which is well-sampled in the time and frequency domains. The optical/NIR light curve of the afterglow of GRB 080710 is dominated by an initial increase in brightness, which smoothly turns over into a shallow power law decay. At around 10 ks post-burst, there is an achromatic break from shallow to steeper decline in the afterglow light curve with a change in the power law index of $\Delta\alpha \sim 0.9$. The initially rising achromatic light curve of the afterglow of GRB 080710 can be accounted for with a model of a burst viewed off-axis or a single jet in its pre-deceleration phase and in an on-axis geometry. A unified picture of the afterglow light curve and prompt emission properties can be obtained with an off-axis geometry, suggesting that late and shallow rising optical light curves of GRB afterglows might be produced by geometric effects.

5.1 Introduction

The launch of the *Swift* satellite (Gehrels et al., 2004) in 2004 opened a new field of gamma-ray burst (GRB) afterglow physics. With its precise localization by the Burst Alert Telescope (BAT;

[1] T. Krühler, J. Greiner, P. Afonso, D. Burlon, C.Clemens, R. Filgas, D.A. Kann, S. Klose, A. Küpcü Yoldaş, S. McBreen, F. Olivares, A. Rau, A. Rossi, S. Schulze, G. P. Szokoly, A. Updike and A. Yoldaş (2009), *A&A*, accepted, arXiv:0908.2250

Barthelmy et al., 2005), rapid slewing capabilities and early follow-up with two instruments in the X-ray and ultraviolet/optical regime, studies of the early afterglow phase were possible for the first time with larger sample statistics of around 50 per year.

Long GRBs are generally classified according to the spectral properties of their prompt emission. While conventional GRBs (CGRBs) have the peak energy of their observed spectrum in the 300 keV range (Preece et al., 2000), the spectrum of X-ray rich bursts (XRRs) and X-ray flashes (XRFs) peak at significantly lower energies, typically around 50 keV for XRRs or 10 keV for XRFs respectively (e.g., Heise et al., 2001; Kippen et al., 2003). The spectral and temporal properties (e.g., Sakamoto et al., 2005) and their afterglows similar to those of CGRBs provide strong evidence, however, that XRRs/XRFs represent a softer region of a continuous GRB distribution (e.g., Lamb et al., 2005; Sakamoto et al., 2008).

A unified picture of the subclasses of GRBs can be obtained by attributing the observed differences in their peak energy to the same objects being observed at different angles with respect to the symmetry axis of the GRB jet (e.g., Yamazaki et al., 2002). The kinetic energy in the jet per solid angle ε is usually parametrized as a top hat (e.g., Rhoads, 1999; Woods & Loeb, 1999), Gaussian (Zhang & Mészáros, 2002a), power-law structured outflow with $\varepsilon \propto (\theta/\theta_{jet})^{-q}$ (Mészáros et al., 1998), or a top hat with lower energetic wings. The resulting shape of the afterglow light curve then depends on the viewing angle and jet structure (e.g., Rossi et al., 2002).

In an inhomogeneous or structured jet model, the initial bulk Lorentz factor as well as the specific deceleration time and radius are dependent on the distance to the symmetry axis of the jet (Kumar & Granot, 2003). Hence, a geometric offset in the observer's line of sight from the jet's symmetry axis will have a distinct signature in the optical light curve (e.g., Granot & Kumar, 2003). Because of the relativistic beaming of the decelerating ejecta, an observer located off-axis to the central jet will see a rising optical afterglow light curve at early times (e.g., Panaitescu et al., 1998; Granot & Sari, 2002b). The steepness of the rise would then be characteristic of the off-axis angle and the jet structure: the farther the observer is located from the central emitting cone or the faster the energy per solid angle decreases outside the jet, the shallower is the observed rise in a structured jet model (Panaitescu & Vestrand, 2008). A rest-frame peak energy $E_{\rm peak}^{\rm rest}$ of the spectrum of the prompt phase consistent with an XRF would thus correspond to a shallow rise or early plateau phase of the afterglow. With decreasing off-axis angle, both $E_{\rm peak}^{\rm rest}$ and the optical afterglow rise index will increase to resemble those of XRRs and steeper rising early afterglow light curves.

5.2 Observations

At T_0=07:13:10 UT on 10 July 2008, *Swift* triggered and located GRB 080710, but did not slew immediately to the burst (Sbarufatti et al., 2008). Because of an observing constraint, observations with the two narrow field instruments, the X-ray- (XRT; Burrows et al., 2005b) and UV/Optical Telescope (UVOT; Roming et al., 2005) started 0.87 h and 0.89 h after the trigger (Landsman & Sbarufatti, 2008). The burst had a relatively smooth fast rise - exponential decay temporal

structure with $T_{90} = 120 \pm 17$ s in the 15-350 keV band and weak indication of a precursor 120 s before the main peak (Tueller et al., 2008). Above 100 keV, the burst was only marginally detected by BAT and its spectrum is well described with a single power law of index -1.47 ± 0.23 and a total fluence in the 15-150 keV range of $(1.4 \pm 0.2) \times 10^{-6}$ erg/cm^2 (Tueller et al., 2008). Using the spectral slope from the BAT data, and following Sakamoto et al. (2009), the peak energy of the prompt emission spectrum can be constrained to be 110^{+340}_{-60} keV, including the uncertainties in the BAT power law slope. The fluence ratio of GRB 080710 between the two BAT bands 25-50 keV and 50-100 keV is $S(25\text{-}50\text{ keV})/S(50\text{-}100\text{ keV}) = 0.70 \pm 0.15$, and the burst thus qualifies as a CGRB in the observer's frame, with errors ranging to a fluence ratio similar to those of XRRs when applying the working definition of Sakamoto et al. (2008).

Assuming a spectral shape of a Band function (Band et al., 1993) with a peak energy of around 110 keV and a high energy index of -2.5, standard ΛCDM cosmology ($\Omega_M = 0.27$, $\Omega_\Lambda = 0.73$, $H_0 = 71$ (km/s)/Mpc) and a redshift z of 0.845 (Perley et al., 2008a; Fynbo et al., 2009), we derive a bolometric (1 keV to 10 MeV) energy release for GRB 080710 of $\log E_{\gamma,\mathrm{iso}}[\mathrm{erg}] = 51.75$ with a rest-frame peak energy of $E^{\mathrm{rest}}_{\mathrm{peak}} \sim 200$ keV. Peak energies of the observed prompt spectrum of 50 keV, 300 keV, or 500 keV result in $\log\ E_{\gamma,\mathrm{iso}}[\mathrm{erg}] \approx 51.70$, 51.94, or 52.14, respectively. Compared to a sample of previous bursts of known redshift (e.g., Amati et al., 2008), these estimates place GRB 080710 at the lower energy end of GRBs, with an inferred bolometric energy release of around 10^3 times less than the extremely energetic GRB 080916C (Abdo et al., 2009a; Greiner et al., 2009c). Hence, a low $E^{\mathrm{rest}}_{\mathrm{peak}}$ in the 50-200 keV range is also supported by the Amati relation (Amati et al., 2002), and is consistent with the most reliable estimate derived using the BAT spectral slope. Given the low redshift and prompt emission properties of GRB 080710, it thus seems very likely that $E^{\mathrm{rest}}_{\mathrm{peak}}$ is in a range that is typically associated with a XRR in the GRB rest frame (100-300 keV, Sakamoto et al., 2008), although a hard burst cannot be completely excluded by the observations.

GROND (Greiner et al., 2008) at the 2.2 m MPI/ESO telescope at LaSilla observatory responded to the *Swift* trigger and initiated automated observations, which started 384 s after the burst. During the first two hours, only the $g'r'i'z'$ CCDs of GROND were operating. Observations in all seven colors $g'r'i'z'JHK_S$ simultaneously started 1.98 h later and continued until the start of the local nautical twilight at 10:27 UT. Afterwards, GROND switched to a NIR-only mode, where only imaging in JHK_S was performed. TLS imaging was obtained between 00:09 UT and 01:43 UT on 11 July 2008 in filters BVR and I (Schulze et al., 2008). In addition, GROND imaged the field of GRB 080710, both 3 and 4 days after the burst.

The XRT light curve was downloaded from the XRT light-curve repository (Evans et al., 2007), and spectra were obtained with the `xrtpipeline` tool using the latest calibration frames from the *Swift* CALDB and standard parameters. The spectra were fitted using the XSPEC package (Arnaud, 1996) with a foreground hydrogen column density at the Galactic value of $N_{\mathrm{H}} = 4.1 \times 10^{20}\,\mathrm{cm}^{-2}$ (Kalberla et al., 2005). Optical/NIR data (see Tables 5.1 and 5.2) were reduced using standard IRAF tasks (Tody, 1993) similar to the procedure outlined in Krühler et al. (2008).

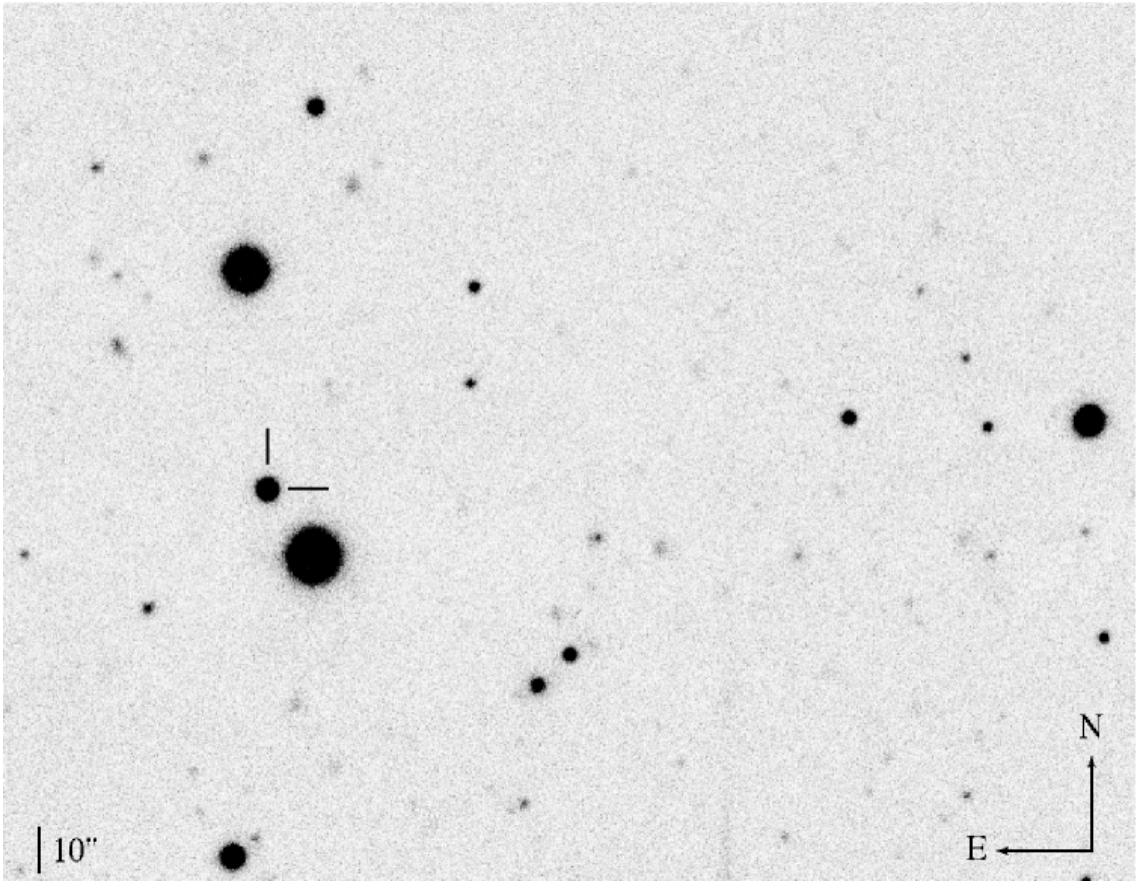

Figure 5.1 GROND r' band image of the field of GRB 080710 obtained approximately 2 ks after T_0. The optical afterglow is marked and the image shown is roughly 4.2′ by 3.2′.

5.3 Results

5.3.1 Afterglow Light Curve

The optical light curve (Fig. 5.2) exhibited two salient features during observations. First, it shows an initial rise in brightness to a peak at around 2000 s, and second, there is a break in the light curve at roughly 10 ks.

The light curve was parametrized with an empirical model of three smoothly connected power laws. The global χ^2 of $F_{\nu,i}(t)$, where i denotes the individual filter or bandpass, was minimized by assuming an achromatic functional form of $F_{\nu,i}(t) = \eta_{\nu,i} \times F_\nu(t)$, where only the overall flux normalization $\eta_{\nu,i}$ depends on the filter, and $F_\nu(t)$ was adapted from Liang et al. (2008). As a result of the high precision of the data and good sampling in the time domain, all parameters were allowed to vary and are presented in Table 5.3. In principle, all fit parameters depend on the choice of T_0. Setting T_0 to the time of the precursor (i.e., -120 s), we find that the fit parameters describing the early/late power laws vary by a maximum of 20% and 2%, respectively. Hence, the uncertainty in T_0 does not change the results derived significantly or affect the overall conclusions.

The decay after the peak at 2 ks with an index of -0.63 ± 0.02 is too shallow to be explained by the normal decay phase, and the late temporal slope of -1.57 ± 0.01 is roughly consistent with the closure relations for the normal decay in the $\nu_m < \nu < \nu_c$ regime for a homogeneous ISM-type circumburst medium in the slow cooling case ($\alpha = 3\beta/2$) (e.g., Zhang & Mészáros, 2004). There is therefore no apparent evidence of a jet-break before 350 ks, and thus $\theta_{\rm jet} > 10^\circ$ according to Sari & Piran (1999).

5.3.2 Broad-band Spectrum

Using the optical/NIR and X-ray data, the afterglow spectrum can be constrained over a broad wavelength range. Four different time intervals were selected to construct a broad-band spectral energy distribution (SED, Fig. 5.3). The different epochs are indicated in the light curve plot with shaded regions, and the SED fit parameters are presented in Table 5.4.

As already indicated by the light curve, there is no sign of spectral evolution throughout the observation. Both the early turnover from rising to falling, as well as the second break are achromatic with high measurement accuracy. The optical/NIR SED alone is consistent with a power law of the X-ray spectral index without strong signatures of curvature due to intrinsic reddening. The expected Galactic foreground extinction $A_V = 0.23$ mag (Schlegel et al., 1998) however is significant, so some amount of host extinction might be masked by the uncertainty in the foreground correction. In addition, the optical data obtained hardly probe the rest-frame UV regime, where most of any intrinsic extinction would be apparent.

Given that the light curve evolution is similar in both energy ranges and the extrapolation of the X-ray data reproduces the optical flux well, i.e., $\beta_{\rm opt} \sim \beta_{\rm ox} \sim \beta_{\rm x}$, both the optical/NIR and X-ray emission probe the same segment of the afterglow synchrotron spectrum. This implies that

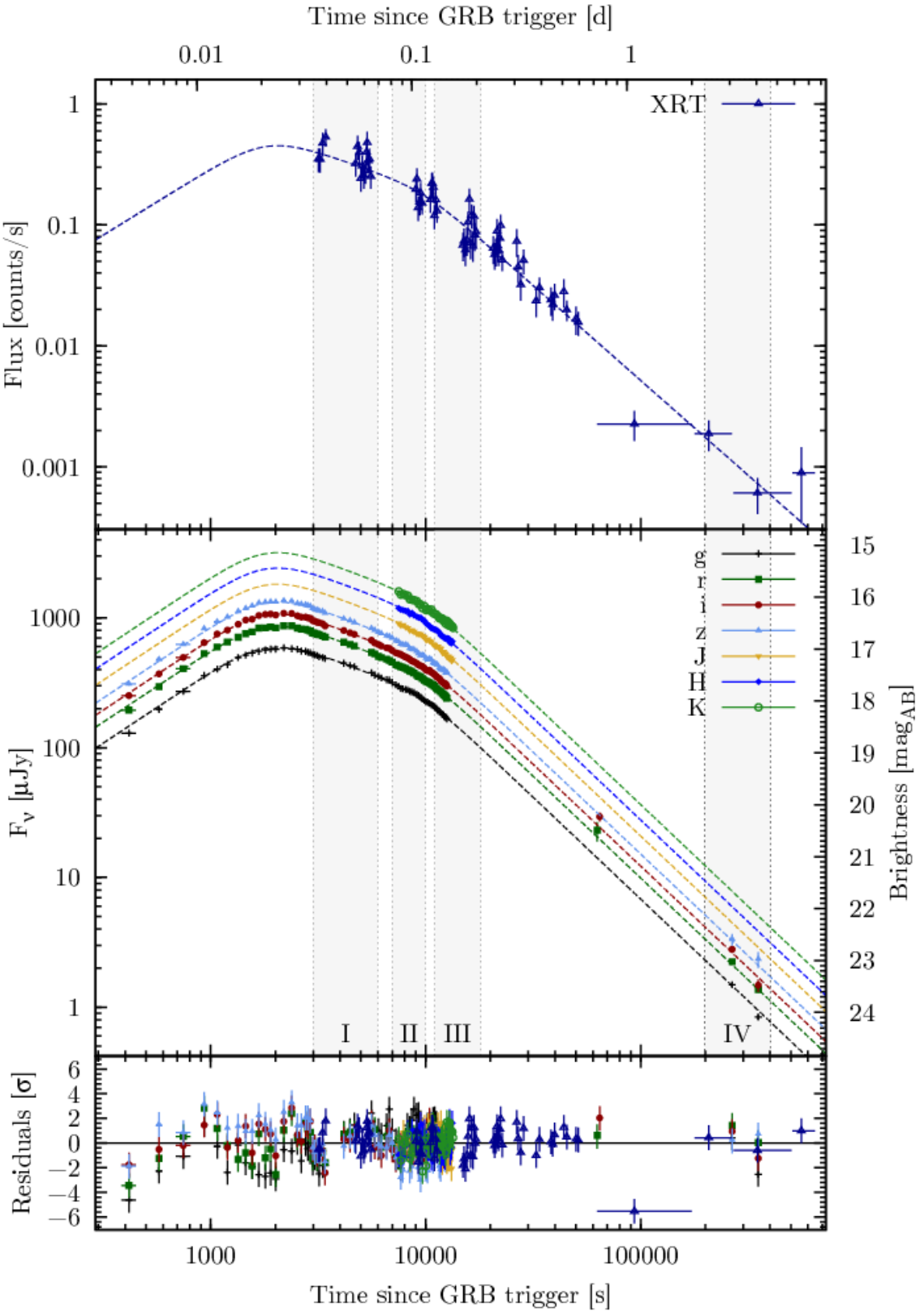

Figure 5.2 Light curves of the X-ray (top panel) and optical/NIR (middle panel) afterglow of GRB 080710. Residuals to the combined light curve fit are shown in the lowest panel. Data shown are not corrected for Galactic foreground reddening. Upper limits are not shown to enhance clarity.

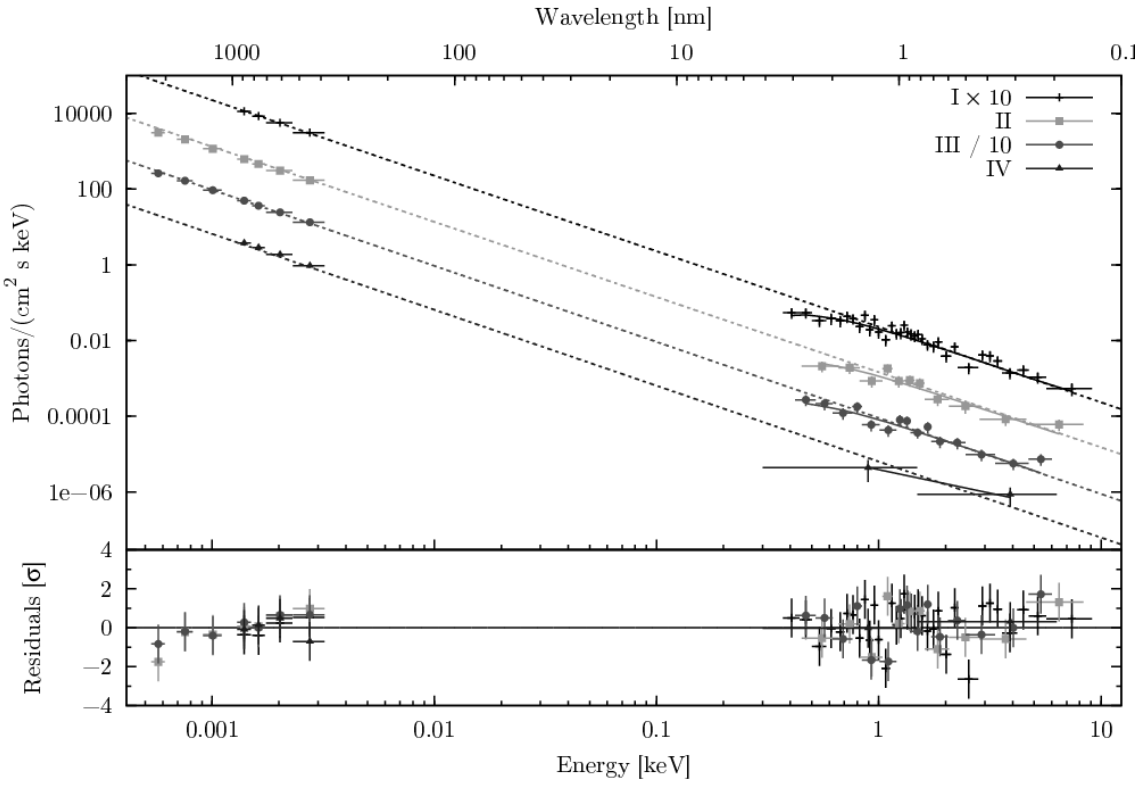

Figure 5.3 Broad-band spectral energy distribution from XRT and GROND at different epochs (upper panel). The data were fitted with a power-law, modified by a Galactic and intrinsic hydrogen column. The best fit power law is shown in dotted lines, the best fit model including the soft X-ray absorption in solid lines. In the lower panel the residuals of the data to the best fit model.

the X-ray and optical data are above the typical synchrotron frequency ν_m and in the spectral regime of $\max(\nu_m, \nu_c) < \nu_{\rm opt} < \nu_X$, or $\nu_m < \nu_{\rm opt} < \nu_X < \nu_c$, where the latter is consistent with a fireball model in a homogeneous ISM and slow cooling case. The spectral index of the electron distribution p would then be $p = 2\beta = 2.00 \pm 0.02$ or $2\beta + 1 = 3.00 \pm 0.02$, respectively. Given that not all bursts are consistent with the closure relations in the basic fireball scenario (e.g., Evans et al., 2008), we consider both cases in the following. Consequentially, the expected break in the synchrotron afterglow spectrum at the cooling frequency ν_c could be below the optical at the start of the observations 6 minutes after the burst, or, assuming $\nu_m < \nu < \nu_c$, above the X-rays for the entire observational period.

5.4 Discussion

A number of previous bursts have shown a rising optical afterglow at early times, e.g., GRBs 060418, 060607A (Molinari et al., 2007) amongst others (e.g., Krühler et al., 2008; Ferrero et al., 2009; Greiner et al., 2009a; Oates et al., 2009; Rykoff et al., 2009; Klotz et al., 2009). Similar to the X-ray Flash 071031 (Krühler et al., 2009), the optical SED does not show significant evolution during the rise, and all bands peak at the same time.

An achromatic rising component is generally related to either the onset of the fireball forward shock (e.g., Sari & Piran, 1999) seen face-on, or to an outflow seen off-axis (e.g., Panaitescu et al., 1998). In the first case, the apparent increase in brightness is caused by the increasing number of radiating electrons. The time of the light curve peak at $T_0 + 2$ ks is much later than the end of significant γ-ray emission ($T_0 + 40$ s), so the afterglow can be described in the thin shell approximation. The jet is then expected to produce a rising early light curve with a peak when the swept-up circumburst medium starts to decelerate the ejecta efficiently. Depending on the profile of the circumburst medium, the rise has indices of ~ 2 ($\nu_c < \nu_{opt}$) or 3 ($\nu_c > \nu_{opt}$) in an ISM, or ~ 0.5 in an wind-like environment (Panaitescu & Vestrand, 2008). Given that the majority of bursts prefer a circumburst medium with an ISM profile, and the late afterglow decline is consistent with this, we thus consider only the ISM, thin shell case in the following.

In the off-axis case, the peak is a geometric effect: as the shock decelerates, the relativistically beamed emission cone widens and gradually enters the sight line of the observer. The light curve morphology is then dependent on the jet structure and off-axis angle θ_{obs}, and reaches a maximum when $\Gamma \sim (\theta_{\rm obs} - \theta_{\rm c})^{-1}$, where $\theta_{\rm c}$ is the angle of an uniform cone around the symmetry axis of the jet.

There is no evidence of chromatic evolution, which would be the case if the peak was caused by a ν_m moving through the optical bands, or dust destruction, and none of these processes can produce the early achromatic rise. In addition, there is also no sign of a reverse shock, which is expected to decline with a temporal index of -1.75 for $p = 2$, or -2.5 for $p = 3$. The latter, however, might be masked by a dominating forward shock, or have happened before the start of the GROND observations.

5.4.1 On-axis Jet in its Pre-deceleration Phase

If the light-curve peak was caused by a jet in its pre-deceleration phase, conclusions about the motion of the ultra-relativistic outflow from the central engine can be drawn. Using the time of the absolute light curve maximum $t_{\rm max} \approx 2$ ks, $\log E_{\gamma,{\rm iso}}[{\rm erg}] = 51.70 - 52.14$ and following Molinari et al. (2007), we find initial Lorentz factors of the bulk outflow of around $\Gamma_0^{\rm ISM} \approx 90 - 100$ ($\Gamma_0^{\rm wind} \approx 30 - 40$). This is at the very low end of the theoretically expected velocity of the outflow to produce γ-rays (e.g., Piran, 2005), and together with the divergence in the measured (1.1) and expected ($\sim 2 - 3$) rise index, makes the scenario of a single on-axis decelerating jet appears somewhat contrived. In addition, a small population of afterglows shows a very late peak or long plateau (e.g., XRF 030723 (Fynbo et al., 2004) or GRB 060614 (Della Valle et al., 2006)), where the derived Lorentz-factor in an on-axis configuration from the optical afterglow peak are uncomfortably small. Furthermore, all previously observed rise indices have a broad distribution (e.g. Panaitescu & Vestrand (2008); Oates et al. (2009); Rykoff et al. (2009); Klotz et al. (2009) and references therein) from early plateau to very fast rising curves, and they do not cluster around the expected t^{2-3}. Consequently, it seems plausible that at least some rising afterglows are not caused by the onset of the afterglow, but rather by a geometrical offset of the observer's sight line with respect to the jet's symmetry axis.

5.4.2 Jet Seen Off-axis

In contrast to the model of an on-axis jet in its pre-deceleration phase, an off-axis scenario is able to account for a broad range of observed rise indices. The peak time and rise index then relates to the off-axis angle or jet structure and could therefore describe a wide diversity of early afterglows in a single framework (Panaitescu & Vestrand, 2008).

If the energy in the jet outer wings decreases rapidly, the early emission of the line-of-sight ejecta is negligible compared to the central part, and the jet structure can be approximated by a homogeneous top-hat, where the burst energetics can be used to constrain the offset angle. Following Granot & Sari (2002b), a homogeneous jet with a half opening angle $\theta_{\rm jet}$ and a Lorentz factor Γ seen off-axis at an angle $\theta_{\rm obs}$ will appear less energetic by a factor of b^6, where $b = \Gamma\,(\theta_{\rm obs} - \theta_{\rm jet})$. Assuming a mean value of $\log E_{\gamma,{\rm iso}}[{\rm erg}] = 53$ and, hence adopting $b^6 \lesssim 10$ for GRB 080710, it follows that $\theta_{\rm obs} - \theta_{\rm jet} \lesssim 3^\circ/\Gamma_{100}$. If viewed on-axis, $E_{\rm peak}$ would then be $b^2\,E^{\rm obs}_{\rm peak} \approx 300$ keV.

However, the jet geometry need not necessarily be a simple top-hat. In a realistic jet model, the jet viewed off-axis is inhomogeneous, has a top-hat structure with wings of lower energy, or is Gaussian shaped (e.g. Zhang et al., 2003b; Eichler & Granot, 2006). In addition, some bursts show evidence that their jet structure consists of two jets (Berger et al., 2003; Granot et al., 2006; Racusin et al., 2008). In this two-component jet model, a narrow, fast jet produces the prompt γ-rays and early afterglow, and a slow wide jet dominates the late afterglow emission (Peng et al., 2005).

In these cases, the resulting afterglow light curve in an off-axis geometry is a superposition of two different components: the emission from the ejecta with lower Lorentz-factors, which typically dominates at late times, and the relativistic spreading of the decelerating jet around the symmetry axis. The relative energies, jet structure, and offset angle then define the light-curve morphology. In particular, the delayed onset of the broad jet emission in its pre-deceleration phase might be responsible for the shallow decay observed after the peak. Remarkably, the light curve is equally well ($\chi^2 = 485$ for 425 d.o.f) reproduced by using the sum of the afterglow of two jets, where the narrow one is viewed slightly off-axis (Fig. 5.4). Hence, the shallow decay phase could be the result of the superposition of the narrow-jet afterglow and the rise of the broad jet with $\Gamma_0 \sim 50$, $\theta_{\rm jet} > 10^\circ$ in its pre-deceleration phase. After the emergence of the broad jet afterglow, it subsequently dominates the light curve morphology (Fig. 5.4). The two-component model thus provides a phenomenological explanation of the shallow decay phase by attributing the shallow slope to the increasing energy dissipation in the pre-deceleration phase of the broader jet in a specific jet configuration. The opening angle of the narrow jet can be constrained from the light-curve fitting to around $2^\circ - 4^\circ$, but its evolution is masked by the brighter broad jet at later times (Fig. 5.4). An alternative, jet geometry independent mechanism of energy injection during a decay phase that is shallower than expected, is the refreshed shock scenario (e.g. Rees & Mészáros, 1998; Zhang et al., 2006). A long lived central engine or a simultaneous ejection of shells with a distribution of Lorentz factors could cause the continuous energy injection required for a shallow decay (e.g. Nousek et al., 2006).

An off-axis viewing angle in a two-component or structured jet model with an energy injection can thus provide a consistent picture for the light-curve morphology and the relatively low estimates

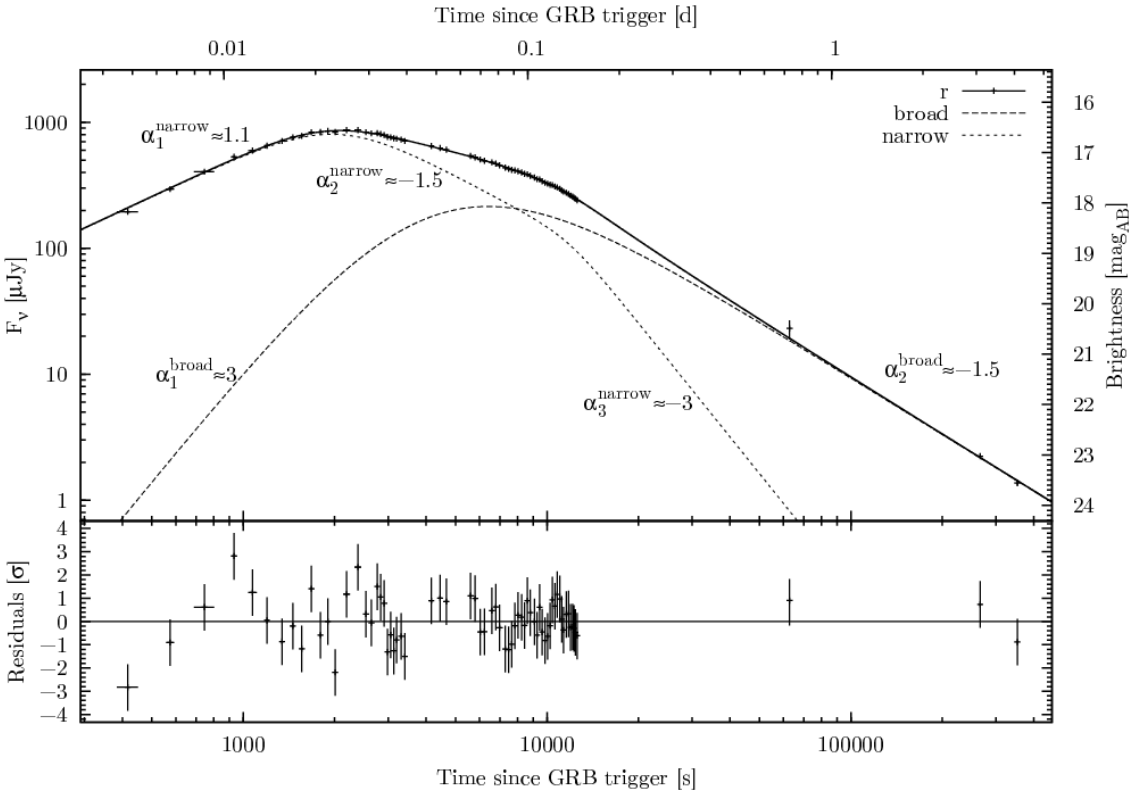

Figure 5.4 Tentative two-component fit for GRB 080710 as the superposition of the afterglow of two jets with $\nu_m < \nu_{\rm opt} < \nu_X < \nu_c$ and p∼3 for both components. The narrow jet is viewed slightly off-axis and produces a shallow rise as its emission spreads during deceleration due to relativistic beaming effects. The broad jet is viewed on-axis with $\Gamma_0 \sim 50$, $\theta_{\rm jet} > 10°$ and has the expected steep rise during its pre-deceleration phase. Shown is the GROND r' band data, all other bands are omitted to enhance clarity.

of $E_{\gamma,\ \rm iso}$ and $E_{\rm peak}^{\rm rest}$ of the prompt emission of GRB 080710. In an off-axis scenario, a lower $E_{\rm peak}^{\rm rest}$ of the prompt emission spectrum would correspond to a later and fainter afterglow maximum, since both are caused by geometric effects. We caution that the spectral properties of BAT bursts are generally not well constrained, and GRB 080710 is no exception in this respect. The BAT data, however, indicate a mildly soft event, which could be associated with a XRR in the burst rest-frame, consistent with the off-axis interpretation of the optical light curve in a unified model.

5.5 Conclusions

The broad-band light curve of the afterglow of GRB 080710 shows two salient features, both achromatic with high precision: an early rise in its brightness, peaking at ∼ 2 ks, and a turnover from a shallow to steep decline at ∼ 10 ks. The early rise could be caused by a jet in its pre-deceleration phase, or a viewing angle outside the central cone. The latter scenario is naturally able to explain a late-rising afterglow for a soft and weak burst due to a viewing angle offset with respect to the symmetry axis of the jet. An off-axis scenario provides a consistent description of the properties of GRB 080710, and can additionally account for a broad range of rise indices.

Consequently, some of the rising afterglow light curves, especially late and shallow ones, might not represent the same class of afterglows that rise because of increasing emission in the pre-deceleration phase, but rather provide evidence of an off-axis location of the observer. The achromatic early increase in brightness observed in the mildly soft GRB 080710 is too shallow to be accounted for with the onset of the afterglow, but significantly steeper than observed in the XRFs 071031 (Krühler et al., 2009) and 080330 (Guidorzi et al., 2009). This might already reflect a common dependence of both $E_{\rm peak}^{\rm rest}$, and the rise index of the early optical light curve, on the off-axis angle in an unified model: the softer the prompt emission, the more off-axis, and the shallower the rise. This interpretation remains to be tested by the study of a larger sample of early afterglows with well constrained energetics and light curves of the prompt emission from combined *Swift*/BAT and *Fermi*/GBM detections, whether and how the structure of an early rise in the optical afterglow is related to prompt emission properties, and in particular, the rest frame $E_{\rm peak}^{\rm rest}$ and $E_{\gamma,\rm iso}$. A possible correlation would then shed light on the nature of the early afterglow rise, the shallow decay segment, and the jet structure in general.

Table 5.1. griz photometric data

$T_{\rm mid} - T_0$ [ks]	Exposure [s]	Filter	Brightness$^{(a)}$ $\rm mag_{AB}^{(bc)}$ g'	Brightness$^{(a)}$ $\rm mag_{AB}^{(bc)}$ r'	Brightness$^{(a)}$ $\rm mag_{AB}^{(bc)}$ i'	Brightness$^{(a)}$ $\rm mag_{AB}^{(bc)}$ z'
0.4169	66	$g'r'i'z'$	18.619 ± 0.028	18.175 ± 0.026	17.899 ± 0.026	17.673 ± 0.028
0.5745	35	$g'r'i'z'$	18.162 ± 0.024	17.724 ± 0.018	17.478 ± 0.018	17.200 ± 0.019
0.7457	115	$g'r'i'z'$	17.815 ± 0.016	17.381 ± 0.010	17.162 ± 0.015	16.909 ± 0.016
0.9334	35	$g'r'i'z'$	17.509 ± 0.013	17.086 ± 0.009	16.875 ± 0.011	16.604 ± 0.016
1.0726	71	$g'r'i'z'$	17.385 ± 0.008	16.961 ± 0.006	16.711 ± 0.009	16.474 ± 0.011
1.1977	35	$g'r'i'z'$	17.300 ± 0.008	16.865 ± 0.006	16.637 ± 0.008	16.381 ± 0.009
1.3423	35	$g'r'i'z'$	17.163 ± 0.007	16.773 ± 0.006	16.523 ± 0.007	16.274 ± 0.008
1.4556	35	$g'r'i'z'$	17.118 ± 0.007	16.701 ± 0.005	16.442 ± 0.007	16.215 ± 0.007
1.5595	35	$g'r'i'z'$	17.075 ± 0.007	16.668 ± 0.005	16.425 ± 0.007	16.169 ± 0.007
1.6767	35	$g'r'i'z'$	17.044 ± 0.006	16.596 ± 0.005	16.354 ± 0.007	16.112 ± 0.007
1.7947	35	$g'r'i'z'$	17.020 ± 0.006	16.595 ± 0.005	16.334 ± 0.007	16.095 ± 0.008
1.8996	35	$g'r'i'z'$	17.003 ± 0.006	16.573 ± 0.005	16.326 ± 0.007	16.089 ± 0.007
2.0065	35	$g'r'i'z'$	17.003 ± 0.006	16.593 ± 0.005	16.343 ± 0.006	16.094 ± 0.006
2.1892	115	$g'r'i'z'$	16.976 ± 0.005	16.552 ± 0.004	16.312 ± 0.004	16.070 ± 0.005
2.3835	115	$g'r'i'z'$	16.995 ± 0.005	16.553 ± 0.004	16.315 ± 0.004	16.078 ± 0.005
2.5359	35	$g'r'i'z'$	17.007 ± 0.006	16.597 ± 0.004	16.363 ± 0.007	16.121 ± 0.006
2.6421	35	$g'r'i'z'$	17.042 ± 0.006	16.617 ± 0.005	16.386 ± 0.007	16.136 ± 0.007
2.7614	35	$g'r'i'z'$	17.044 ± 0.006	16.617 ± 0.005	16.387 ± 0.006	16.147 ± 0.007
2.8323	35	$g'r'i'z'$	17.061 ± 0.006	16.635 ± 0.005	16.401 ± 0.007	16.159 ± 0.007
2.9105	35	$g'r'i'z'$	17.074 ± 0.006	16.652 ± 0.005	16.409 ± 0.007	16.176 ± 0.007
2.9854	35	$g'r'i'z'$	17.103 ± 0.006	16.692 ± 0.005	16.453 ± 0.007	16.219 ± 0.007
3.0564	35	$g'r'i'z'$	17.110 ± 0.006	16.696 ± 0.005	16.463 ± 0.007	16.236 ± 0.007
3.1276	35	$g'r'i'z'$	17.125 ± 0.007	16.718 ± 0.005	16.483 ± 0.007	16.248 ± 0.008
3.1962	35	$g'r'i'z'$	17.151 ± 0.006	16.724 ± 0.005	16.492 ± 0.007	16.261 ± 0.008
3.3151	35	$g'r'i'z'$	17.164 ± 0.006	16.744 ± 0.005	16.513 ± 0.007	16.273 ± 0.008
3.4059	35	$g'r'i'z'$	17.181 ± 0.007	16.771 ± 0.005	16.554 ± 0.008	16.309 ± 0.007
4.1611	115	$g'r'i'z'$	17.273 ± 0.005	16.869 ± 0.004	16.643 ± 0.005	16.418 ± 0.006
4.4496	115	$g'r'i'z'$	17.315 ± 0.005	16.911 ± 0.004	16.689 ± 0.005	16.452 ± 0.006
4.6632	115	$g'r'i'z'$	17.341 ± 0.005	16.944 ± 0.004	16.716 ± 0.005	16.488 ± 0.006
5.6014	115	$g'r'i'z'$	17.456 ± 0.005	17.067 ± 0.004	16.830 ± 0.005	16.601 ± 0.006
5.8030	115	$g'r'i'z'$	17.501 ± 0.006	17.094 ± 0.004	16.881 ± 0.006	16.637 ± 0.006
6.0290	115	$g'r'i'z'$	17.529 ± 0.005	17.140 ± 0.004	16.910 ± 0.006	16.675 ± 0.006
6.2166	115	$g'r'i'z'$	17.556 ± 0.006	17.163 ± 0.004	16.941 ± 0.005	16.700 ± 0.006
6.5862	115	$g'r'i'z'$	17.591 ± 0.006	17.197 ± 0.004	16.977 ± 0.006	16.746 ± 0.006
6.7883	115	$g'r'i'z'$	17.598 ± 0.006	17.219 ± 0.004	16.984 ± 0.006	16.757 ± 0.006
6.9845	115	$g'r'i'z'$	17.643 ± 0.006	17.254 ± 0.004	17.028 ± 0.006	16.788 ± 0.007
7.2804	115	$g'r'i'z'$	17.689 ± 0.006	17.300 ± 0.004	17.073 ± 0.006	16.839 ± 0.007
7.4691	115	$g'r'i'z'$	17.713 ± 0.006	17.323 ± 0.004	17.087 ± 0.006	16.853 ± 0.006
7.6567	115	$g'r'i'z'$	17.760 ± 0.005	17.342 ± 0.004	17.101 ± 0.004	16.902 ± 0.006
7.8462	115	$g'r'i'z'$	17.769 ± 0.005	17.355 ± 0.004	17.130 ± 0.005	16.918 ± 0.006
8.0363	115	$g'r'i'z'$	17.779 ± 0.004	17.371 ± 0.004	17.150 ± 0.005	16.918 ± 0.006
8.2434	115	$g'r'i'z'$	17.786 ± 0.006	17.397 ± 0.004	17.170 ± 0.007	16.928 ± 0.007
8.4312	115	$g'r'i'z'$	17.812 ± 0.005	17.423 ± 0.004	17.197 ± 0.005	16.989 ± 0.007
8.6219	115	$g'r'i'z'$	17.826 ± 0.004	17.432 ± 0.004	17.226 ± 0.004	17.005 ± 0.006
8.8119	115	$g'r'i'z'$	17.836 ± 0.006	17.461 ± 0.005	17.247 ± 0.005	17.010 ± 0.006
9.0840	115	$g'r'i'z'$	17.875 ± 0.006	17.498 ± 0.005	17.274 ± 0.008	17.043 ± 0.010
9.2723	115	$g'r'i'z'$	17.898 ± 0.006	17.527 ± 0.004	17.304 ± 0.006	17.086 ± 0.007
9.4591	115	$g'r'i'z'$	17.929 ± 0.005	17.534 ± 0.004	17.324 ± 0.006	17.123 ± 0.008
9.6457	115	$g'r'i'z'$	17.960 ± 0.005	17.570 ± 0.004	17.333 ± 0.005	17.116 ± 0.006
9.8478	115	$g'r'i'z'$	17.989 ± 0.006	17.599 ± 0.005	17.366 ± 0.007	17.132 ± 0.008
10.037	115	$g'r'i'z'$	18.013 ± 0.005	17.619 ± 0.004	17.401 ± 0.005	17.180 ± 0.006
10.227	115	$g'r'i'z'$	18.025 ± 0.005	17.636 ± 0.004	17.419 ± 0.005	17.206 ± 0.007
10.420	115	$g'r'i'z'$	18.046 ± 0.006	17.646 ± 0.005	17.408 ± 0.004	17.187 ± 0.008

Table 5.1 (cont'd)

$T_{\rm mid} - T_0$ [ks]	Exposure [s]	Filter	Brightness[(a)] $\rm mag_{AB}^{(bc)}$ g'	Brightness[(a)] $\rm mag_{AB}^{(bc)}$ r'	Brightness[(a)] $\rm mag_{AB}^{(bc)}$ i'	Brightness[(a)] $\rm mag_{AB}^{(bc)}$ z'
10.622	115	$g'r'i'z'$	18.072 ± 0.006	17.674 ± 0.005	17.446 ± 0.007	17.203 ± 0.008
10.811	115	$g'r'i'z'$	18.091 ± 0.005	17.692 ± 0.004	17.467 ± 0.005	17.266 ± 0.006
11.001	115	$g'r'i'z'$	18.114 ± 0.005	17.718 ± 0.004	17.494 ± 0.005	17.281 ± 0.006
11.194	115	$g'r'i'z'$	18.142 ± 0.005	17.753 ± 0.007	17.523 ± 0.006	17.289 ± 0.006
11.333	115	$g'r'i'z'$	18.175 ± 0.006	17.776 ± 0.004	17.547 ± 0.007	17.302 ± 0.008
11.574	115	$g'r'i'z'$	18.199 ± 0.005	17.798 ± 0.005	17.567 ± 0.008	17.365 ± 0.006
11.763	115	$g'r'i'z'$	18.222 ± 0.005	17.822 ± 0.004	17.613 ± 0.008	17.391 ± 0.006
11.957	115	$g'r'i'z'$	18.258 ± 0.006	17.855 ± 0.009	17.633 ± 0.008	17.400 ± 0.007
12.134	66	$g'r'i'z'$	18.268 ± 0.011	17.877 ± 0.007	17.656 ± 0.010	17.395 ± 0.010
12.270	66	$g'r'i'z'$	18.300 ± 0.007	17.895 ± 0.005	17.671 ± 0.007	17.415 ± 0.010
12.410	66	$g'r'i'z'$	18.320 ± 0.011	17.915 ± 0.006	17.671 ± 0.009	17.462 ± 0.010
12.552	66	$g'r'i'z'$	18.348 ± 0.013	17.948 ± 0.008	17.714 ± 0.011	17.443 ± 0.013
62.856	300	R[(d)]		20.49 ± 0.18		
64.523	4 x 300	I[(d)]		20.23 ± 0.09		
266.59	8 x 365	$g'r'i'z'$	23.47 ± 0.06	23.02 ± 0.05	22.79 ± 0.07	22.59 ± 0.11
353.11	8 x 365	$g'r'i'z'$	24.09 ± 0.07	23.56 ± 0.06	23.28 ± 0.12	22.97 ± 0.15

[(a)] Not corrected for Galactic foreground reddening
[(b)] In the light curve fitting, a systematic error of 0.012 mag was added quadratically to the quoted statistical error
[(c)] For the SED fitting, the aditional error of the absolute calibration of 0.05 mag was added
[(d)] Calibrated using the GROND r' and i' field calibration, including a (r'-i') color term

Table 5.2. JHK_S photometric data

$T_{\rm mid} - T_0$ [ks]	Exposure [s]	Filter	Brightness[(a)] $\rm mag_{AB}^{(bc)}$ J	Brightness[(a)] $\rm mag_{AB}^{(bc)}$ H	Brightness[(a)] $\rm mag_{AB}^{(bc)}$ K
7.4943	12 x 10	JHK_S	16.506 ± 0.009	16.215 ± 0.017	15.887 ± 0.019
7.6818	12 x 10	JHK_S	16.541 ± 0.008	16.240 ± 0.017	15.954 ± 0.019
7.8710	12 x 10	JHK_S	16.533 ± 0.008	16.251 ± 0.011	15.940 ± 0.013
8.0611	12 x 10	JHK_S	16.571 ± 0.008	16.264 ± 0.013	15.962 ± 0.014
8.2685	12 x 10	JHK_S	16.591 ± 0.009	16.267 ± 0.012	15.968 ± 0.014
8.4560	12 x 10	JHK_S	16.638 ± 0.008	16.329 ± 0.015	16.042 ± 0.016
8.6469	12 x 10	JHK_S	16.638 ± 0.008	16.309 ± 0.012	16.052 ± 0.014
8.8370	12 x 10	JHK_S	16.664 ± 0.009	16.346 ± 0.013	16.058 ± 0.015
9.1091	12 x 10	JHK_S	16.703 ± 0.009	16.378 ± 0.014	16.075 ± 0.016
9.2966	12 x 10	JHK_S	16.706 ± 0.008	16.397 ± 0.011	16.135 ± 0.013
9.4841	12 x 10	JHK_S	16.714 ± 0.008	16.397 ± 0.013	16.140 ± 0.015
9.6707	12 x 10	JHK_S	16.745 ± 0.009	16.437 ± 0.012	16.215 ± 0.014
9.8729	12 x 10	JHK_S	16.765 ± 0.009	16.455 ± 0.017	16.175 ± 0.018
10.062	12 x 10	JHK_S	16.825 ± 0.009	16.508 ± 0.015	16.252 ± 0.016
10.252	12 x 10	JHK_S	16.810 ± 0.008	16.533 ± 0.016	16.231 ± 0.017
10.447	12 x 10	JHK_S	16.842 ± 0.008	16.556 ± 0.017	16.258 ± 0.018
10.646	12 x 10	JHK_S	16.857 ± 0.009	16.599 ± 0.017	16.236 ± 0.018
10.835	12 x 10	JHK_S	16.908 ± 0.008	16.611 ± 0.017	16.310 ± 0.019
11.025	12 x 10	JHK_S	16.916 ± 0.008	16.620 ± 0.015	16.321 ± 0.016
11.213	12 x 10	JHK_S	16.949 ± 0.009	16.629 ± 0.014	16.334 ± 0.016
11.415	12 x 10	JHK_S	16.950 ± 0.009	16.658 ± 0.014	16.370 ± 0.016
11.598	12 x 10	JHK_S	16.989 ± 0.009	16.684 ± 0.011	16.411 ± 0.013
11.788	12 x 10	JHK_S	16.993 ± 0.008	16.737 ± 0.012	16.405 ± 0.014
11.983	12 x 10	JHK_S	17.071 ± 0.009	16.751 ± 0.013	16.414 ± 0.015
12.140	6 x 10	JHK_S	17.048 ± 0.011	16.770 ± 0.013	16.465 ± 0.014
12.277	6 x 10	JHK_S	17.079 ± 0.011	16.794 ± 0.014	16.453 ± 0.016
12.417	6 x 10	JHK_S	17.099 ± 0.010	16.788 ± 0.016	16.512 ± 0.017
12.560	6 x 10	JHK_S	17.141 ± 0.011	16.805 ± 0.016	16.458 ± 0.017
12.707	6 x 10	JHK_S	17.154 ± 0.010	16.796 ± 0.015	16.478 ± 0.016
12.806	6 x 10	JHK_S	17.144 ± 0.010	16.820 ± 0.014	16.543 ± 0.016
12.904	6 x 10	JHK_S	17.177 ± 0.011	16.808 ± 0.012	16.500 ± 0.014
13.003	6 x 10	JHK_S	17.174 ± 0.011	16.878 ± 0.024	16.553 ± 0.025
13.116	6 x 10	JHK_S	17.170 ± 0.011	16.863 ± 0.015	16.544 ± 0.016
13.209	6 x 10	JHK_S	17.226 ± 0.010	16.887 ± 0.017	16.555 ± 0.018
13.308	6 x 10	JHK_S	17.210 ± 0.010	16.856 ± 0.014	16.569 ± 0.016
13.408	6 x 10	JHK_S	- - -	16.883 ± 0.019	16.593 ± 0.020
269.07	240 x 10	JHK_S	> 22.47	> 21.97	> 21.224
354.88	240 x 10	JHK_S	> 22.29	> 22.04	> 21.082

[(a)] Not corrected for Galactic foreground reddening, but converted to AB magnitudes for consistency with Tab. 5.1
[(b)] In the light curve fitting, a systematic error of 0.02 mag was added quadratically to the quoted statistical error
[(c)] For the SED fitting, the aditional error of the absolute calibration of 0.07 (J and H) and 0.09 (K) mag was added

Table 5.3. Light curve fits

Bands	$F_\nu(t)$	$\alpha_{\rm r}^{(a)}$	s_1	$t_{\rm b,1}$ [s]	$\alpha_{d,1}^{(a)}$	s_2	$t_{\rm b,2}$ [s]	$\alpha_{\rm d,2}^{(a)}$	χ^2/d.o.f
g'	TPL$^{(b)}$	1.20 ± 0.11	2.2 ± 0.5	1775 ± 62	-0.64 ± 0.04	7.2 ± 1.7	9665 ± 170	-1.58 ± 0.01	58 / 59
r'	TPL$^{(b)}$	1.11 ± 0.07	2.6 ± 0.4	1816 ± 39	-0.65 ± 0.03	6.7 ± 1.3	9767 ± 157	-1.55 ± 0.01	49 / 60
i'	TPL$^{(b)}$	1.10 ± 0.05	3.1 ± 0.5	1836 ± 37	-0.63 ± 0.03	5.5 ± 1.2	9752 ± 185	-1.56 ± 0.02	52 / 60
z'	TPL$^{(b)}$	1.10 ± 0.06	3.4 ± 0.5	1835 ± 34	-0.60 ± 0.04	4.2 ± 1.0	9795 ± 268	-1.56 ± 0.03	61 / 59
JHK	DPL$^{(c)}$	—	—	—	-0.53 ± 0.15	5.7 ± 1.7	9542 ± 527	-1.57 ± 0.15	84 / 99
g'-K	TPL$^{(b)}$	1.11 ± 0.03	2.9 ± 0.2	1829 ± 19	-0.63 ± 0.02	5.7 ± 0.5	9763 ± 83	-1.57 ± 0.01	425 / 362
XRT-K	TPL$^{(b)}$	1.11 ± 0.03	2.9 ± 0.2	1829 ± 19	-0.63 ± 0.02	5.7 ± 0.5	9759 ± 82	-1.57 ± 0.01	488 / 428

$^{(a)}$ Power law indices α of the segmented light curve, which are connected via breaks with smoothness s at break times $t_{\rm b}$
$^{(b)}$ Smoothly connected triple power law
$^{(c)}$ Smoothly connected double power law

Table 5.4. SED fits

Epoch	Spectral index β	$N_{\rm H}^{(a)}$ [10^{22}cm^2]	χ^2/d.o.f
I	1.00 ± 0.01	0.19 ± 0.09	36 / 36
II	0.99 ± 0.01	0.17 ± 0.10	15 / 15
III	1.01 ± 0.01	$0.13\ ^{+0.15}_{-0.13}$	18 / 19
IV	1.01 ± 0.01	$0.53\ ^{+1.30}_{-0.53}$	0.3 / 3

$^{(a)}$ Intrisic hydrogen column desity, in excess of the frozen Galactic foreground of $N_{\rm H}$=4.1×10^{20} cm^{-2}

Chapter 6

Summary and Outlook

While this thesis set up the framework of data reduction, analysis and science tools for GROND observations and focused on the analysis of individual afterglows, there remains a lot to be studied in GRB afterglow physics. The next steps will include a combination of all GROND observed afterglows to a homogeneous sample. Using the properties of this sample, which yields unprecedented number statistics as well as coverage in time and frequency domain, many open question in GRB physics can be addressed in a systematic way: the nature of optically dark or sub-luminous afterglows, the average amount of dust extinction, the typical dust attenuation law in GRB host galaxies and details about the optical afterglow light curve morphology are just few examples. Together with the large sample of XRT light curves, furthermore the correlation between the X-ray and optical afterglow can be studied, providing new insights into afterglow physics. This combined data set might be able to answer, what is the dust-to-gas ratio in the burst environment and its host galaxy, where are the achromatic jet breaks or how common are chromatic breaks, how exactly does the early optical afterglow evolve as compared to the X-rays, and is the standard fireball model able to account for a large set of well sampled afterglows in both, the X-ray and optical regime, or are the previous modifications to the fireball model just further complications of a fundamentally deficient model ?

In addition we are just beginning to utilize GRBs as probes of the early universe. After 5 years of *Swift* operation, there is now a growing number of ground-based instruments available dedicated to and specialized on afterglow observations. Because of its unprecedented spectral coverage and sensitivity, GROND is able to detect the majority of afterglows of GRBs to redshifts of 10 and above. GROND can thus systematically provide a rapid trigger on extremely distant events for spectroscopy on 8 m class telescopes. The detection of two ultra high-z GRBs within the last 9 months (GRB 080913, GRB 090423), both exceeding the redshift of the most distant GRB so far, and the latter clearly exceeding the distance to the most distant object known to date, demonstrate the potential of GRBs to investigate the very early Universe, and possibly even the first generation of stars. Although number statistics are still low, first cosmological applications already provide information about the dark ages of the Universe, which is not accessible by other means except GRBs.

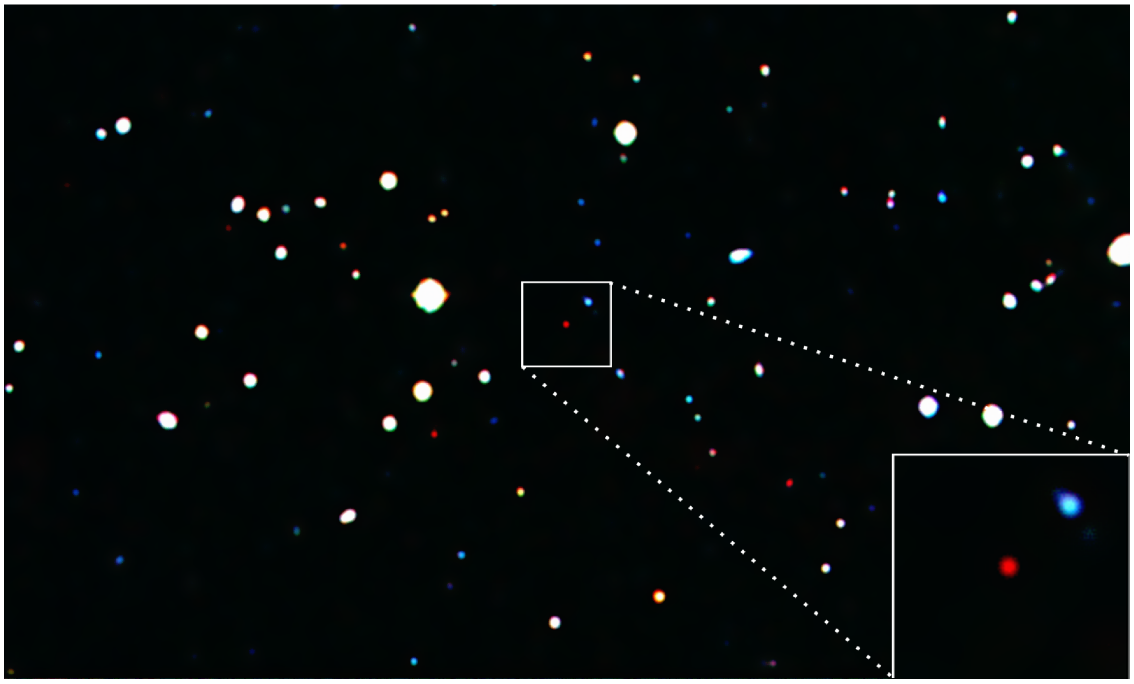

Figure 6.1 The most distant spectroscopically confirmed object in the universe so far: GRB 090423 at redshift 8.3 as obtained with GROND on 23.04.2009

A new field of GRB science has opened with the launch of the *Fermi* satellite. Combined with the distance information obtained with ground-based telescopes, the high energy photons detected by GBM and LAT will give strong constraints on the prompt γ-ray spectrum and emission mechanisms, the energy scale of quantum gravity and the extragalactic background light. 40 years after the discovery of GRBs there are now two missions in orbit, focusing on afterglow (*Swift*) and prompt phase (*Fermi*), whereas previously the focus was on one or the other. Combining the information obtained with these satellites with ground-based follow-up observations, will provide more information of the physical concepts in GRB astronomy than ever before. This data set will result in a better understanding of GRB physics and the evolution of the early Universe within a time scale of a few years.

Bibliography

Abdo, A. A. et al. 2009a, Science, 323, 1688

—. 2009b, Nature, submitted, arXiv:0908.1832

Adelman-McCarthy, J. K. et al. 2008, ApJS, 175, 297

Akerlof, C. et al. 1999, Nature, 398, 400

Aloy, M. A., Müller, E., Ibáñez, J. M., Martí, J. M., & MacFadyen, A. 2000, ApJ, 531, L119

Amati, L., Guidorzi, C., Frontera, F., Della Valle, M., Finelli, F., Landi, R., & Montanari, E. 2008, MNRAS, 391, 577

Amati, L. et al. 2002, A&A, 390, 81

Arnaud, K. A. 1996, in ASPC Ser., Vol. 101, Astronomical Data Analysis Software and Systems V, ed. G. H. Jacoby & J. Barnes, 17

Atwood, W. B. et al. 2009, ApJ, 697, 1071

Band, D. et al. 1993, ApJ, 413, 281

Barthelmy, S. D. et al. 2005, Space Science Reviews, 120, 143

—. 2007, GRB Coordinates Network, 6692

Beloborodov, A. M. 2005, ApJ, 618, L13

Berger, E. 2009, ApJ, 690, 231

Berger, E. & Murphy, D. 2007, GRB Coordinates Network, 6695

Berger, E., Penprase, B. E., Cenko, S. B., Kulkarni, S. R., Fox, D. B., Steidel, C. C., & Reddy, N. A. 2006, ApJ, 642, 979

Berger, E. et al. 2003, Nature, 426, 154

—. 2007, ApJ, 664, 1000

Bertin, E. & Arnouts, S. 1996, A&AS, 117, 393

Beuermann, K. et al. 1999, A&A, 352, L26

Blake, C. H. et al. 2005, Nature, 435, 181

Blandford, R. D. & McKee, C. F. 1976, Physics of Fluids, 19, 1130

Bloom, J. S., Frail, D. A., & Kulkarni, S. R. 2003, ApJ, 594, 674

Bloom, J. S. et al. 2009, ApJ, 691, 723

Boër, M., Atteia, J. L., Damerdji, Y., Gendre, B., Klotz, A., & Stratta, G. 2006, ApJ, 638, L71

Bolzonella, M., Miralles, J.-M., & Pelló, R. 2000, A&A, 363, 476

Bouwens, R. J., Illingworth, G. D., Franx, M., & Ford, H. 2008, ApJ, 686, 230

Breeveld, A. A. & Stroh, M. 2007, GRB Coordinates Network, 7028

Bromm, V. & Loeb, A. 2002, ApJ, 575, 111

Brun, R. & Rademakers, F. 1997, Nucl. Instrum. Meth., A389, 81

Burrows, D. N. et al. 2005a, Science, 309, 1833

—. 2005b, Space Science Reviews, 120, 165

Butler, N. R. & Kocevski, D. 2007, ApJ, 663, 407

Butler, N. R., Kocevski, D., Bloom, J. S., & Curtis, J. L. 2007, ApJ, 671, 656

Bykov, A. M. & Mészáros, P. 1996, ApJ, 461, L37

Calzetti, D. 2001, PASP, 113, 1449

Cardelli, J. A., Clayton, G. C., & Mathis, J. S. 1989, ApJ, 345, 245

Cenko, S. B. et al. 2009, ApJ, 693, 1484

Chevalier, R. A. & Li, Z.-Y. 2000, ApJ, 536, 195

Chincarini, G. et al. 2007, ApJ, 671, 1903

Clemens, C. 2009, PhD thesis, TU München / Max-Planck-Institut für extraterrestrische Physik

Cobb, B. E. 2007, GRB Coordinates Network, 7024

Covino, S. et al. 2008, MNRAS, 388, 347

Cummings, J. et al. 2007, GRB Coordinates Network, 6699

Dado, S., Dar, A., & De Rújula, A. 2002, A&A, 388, 1079

Dai, Z. G. & Cheng, K. S. 2001, ApJ, 558, L109

Dai, Z. G. & Lu, T. 1998, A&A, 333, L87

Dar, A. & de Rújula, A. 2004, Phys. Rep., 405, 203

de Ugarte Postigo, A. et al. 2005, A&A, 443, 841

Della Valle, M. et al. 2006, Nature, 444, 1050

Dermer, C. D. 2004, ApJ, 614, 284

Dickey, J. M. & Lockman, F. J. 1990, ARA&A, 28, 215

Draine, B. T. 2003, ARA&A, 41, 241

Drenkhahn, G. & Spruit, H. C. 2002, A&A, 391, 1141

Duley, W. W. & Lazarev, S. 2004, ApJ, 612, L33

Eichler, D. & Granot, J. 2006, ApJ, 641, L5

Evans, P. A. et al. 2007, A&A, 469, 379

—. 2008, ArXiv:0812.3662

Falcone, A. D. et al. 2006, ApJ, 641, 1010

—. 2007, ApJ, 671, 1921

Faucher-Giguère, C.-A., Prochaska, J. X., Lidz, A., Hernquist, L., & Zaldarriaga, M. 2008, ApJ, 681, 831

Fenimore, E. E., Epstein, R. I., & Ho, C. 1993, A&AS, 97, 59

Ferrero, P. et al. 2009, A&A, 497, 729

Firmani, C., Ghisellini, G., Ghirlanda, G., & Avila-Reese, V. 2005, MNRAS, 360, L1

Fishman, G. J. et al. 1993, A&AS, 97, 17

—. 1994, ApJS, 92, 229

Fitzpatrick, E. L. 1986, AJ, 92, 1068

Fitzpatrick, E. L. & Massa, D. 1986, ApJ, 307, 286

Foley, S., McGlynn, S., Hanlon, L., McBreen, S., & McBreen, B. 2008, A&A, 484, 143

Fox, A. J., Ledoux, C., Vreeswijk, P. M., Smette, A., & Jaunsen, A. O. 2008, A&A, 491, 189

Fox, D. B. et al. 2005, Nature, 437, 845

Fox, D. W. et al. 2003, Nature, 422, 284

Frail, D. A. et al. 2001, ApJ, 562, L55

Frontera, F. et al. 1998, A&A, 334, L69

Fryer, C. L., Hungerford, A. L., & Young, P. A. 2007, ApJ, 662, L55

Fryer, C. L., Woosley, S. E., & Hartmann, D. H. 1999, ApJ, 526, 152

Fryer, C. L., Young, P. A., & Hungerford, A. L. 2006, ApJ, 650, 1028

Fukugita, M., Ichikawa, T., Gunn, J. E., Doi, M., Shimasaku, K., & Schneider, D. P. 1996, AJ, 111, 1748

Fynbo, J. P. U. et al. 2001, A&A, 373, 796

—. 2004, ApJ, 609, 962

—. 2005, GRB Coordinates Network, 3749

—. 2006, A&A, 451, L47

—. 2007, ESO Messenger, 130, 43

—. 2009, ArXiv:0907.3449

Gal-Yam, A. et al. 2006, Nature, 444, 1053

Galama, T. J. & Wijers, R. A. M. J. 2001, ApJ, 549, L209

Galama, T. J. et al. 1998, Nature, 395, 670

Gehrels, N., Piro, L., & Leonard, P. J. T. 2007, Scientific American Reports, 17, 34

Gehrels, N. et al. 2004, ApJ, 611, 1005

—. 2006, Nature, 444, 1044

Genet, F., Daigne, F., & Mochkovitch, R. 2007, MNRAS, 381, 732

Ghirlanda, G., Ghisellini, G., Lazzati, D., & Firmani, C. 2004, ApJ, 613, L13

Ghisellini, G., Ghirlanda, G., Nava, L., & Firmani, C. 2007, ApJ, 658, L75

Goad, M. R. et al. 2007, A&A, 468, 103

Gordon, K. D., Calzetti, D., & Witt, A. N. 1997, ApJ, 487, 625

Granot, J., Königl, A., & Piran, T. 2006, MNRAS, 370, 1946

Granot, J. & Kumar, P. 2003, ApJ, 591, 1086

Granot, J. & Sari, R. 2002a, ApJ, 568, 820

—. 2002b, ApJ, 568, 820

Greiner, J. et al. 2003a, Nature, 426, 157

—. 2003b, GRB Coordinates Network, 2020

—. 2007a, GRB Coordinates Network, 6694

—. 2007b, ESO Messenger, 130, 12

—. 2008, PASP, 120, 405

—. 2009a, ApJ, 693, 1912

—. 2009b, ApJ, 693, 1610

—. 2009c, A&A, 498, 89

Groot, P. J. et al. 1998, ApJ, 493, L27

Guetta, D. et al. 2007, A&A, 461, 95

Guidorzi, C. et al. 2005, ApJ, 630, L121

—. 2007, A&A, 474, 793

—. 2009, A&A, 499, 439

Haislip, J. et al. 2007, GRB Coordinates Network, 7022

Heise, J., in't Zand, J., Kippen, R. M., & Woods, P. M. 2001, in Gamma-ray Bursts in the Afterglow Era, ed. E. Costa, F. Frontera, & J. Hjorth, 16

Hjorth, J. et al. 2003, Nature, 423, 847

Hopkins, A. M. & Beacom, J. F. 2006, ApJ, 651, 142

Immler, S., Mangano, V., Kuin, N. P. M., & Cummings, J. 2007, GCN Report, 78

Ioka, K., Kobayashi, S., & Zhang, B. 2005, ApJ, 631, 429

Jakobsson, P. et al. 2006, A&A, 447, 897

James, F. & Roos, M. 1975, Comput. Phys. Commun., 10, 343

Kalberla, P. M. W., Burton, W. B., Hartmann, D., Arnal, E. M., Bajaja, E., Morras, R., & Pöppel, W. G. L. 2005, A&A, 440, 775

Kaneko, Y., Preece, R. D., Briggs, M. S., Paciesas, W. S., Meegan, C. A., & Band, D. L. 2006, ApJS, 166, 298

Kann, D. A., Klose, S., & Zeh, A. 2006, ApJ, 641, 993

Kann, D. A. et al. 2008, ApJ, submitted

Katz, J. I. 1994, ApJ, 432, L107

Kawai, N. et al. 2006, Nature, 440, 184

Kippen, R. M., Woods, P. M., Heise, J., in't Zand, J. J. M., Briggs, M. S., & Preece, R. D. 2003, in AIPC, Vol. 662, Gamma-Ray Burst and Afterglow Astronomy 2001, ed. G. R. Ricker & R. K. Vanderspek, 244

Kistler, M. D., Yuksel, H., Beacom, J. F., Hopkins, A. M., & Wyithe, J. S. B. 2009, ArXiv e-prints

Klebesadel, R. W., Strong, I. B., & Olson, R. A. 1973, ApJ, 182, L85

Klose, S. et al. 2003, ApJ, 592, 1025

Klotz, A., Boër, M., Atteia, J. L., & Gendre, B. 2009, AJ, 137, 4100

Kobayashi, S. & Sari, R. 2000, ApJ, 542, 819

Kobayashi, S. & Zhang, B. 2007, ApJ, 655, 973

Kocevski, D., Butler, N., & Bloom, J. S. 2007, ApJ, 667, 1024

Kouveliotou, C., Meegan, C. A., Fishman, G. J., Bhat, N. P., Briggs, M. S., Koshut, T. M., Paciesas, W. S., & Pendleton, G. N. 1993, ApJ, 413, L101

Krühler, T. 2006, Master's thesis, TU München / Max-Planck-Institut für extraterrestrische Physik

Krühler, T., Greiner, J., Afonso, P., Küpcü-Yoldaş, A., Yoldaş, A., & Szokoly, G. P. 2007, GRB Coordinates Network, 7021

Krühler, T. et al. 2008, ApJ, 685, 376

—. 2009, ApJ, 697, 758

Kumar, P. & Granot, J. 2003, ApJ, 591, 1075

Kumar, P. & Piran, T. 2000, ApJ, 535, 152

Küpcü-Yoldaş, A. 2006, PhD thesis, TU München / Max-Planck-Institut für extraterrestrische Physik

Küpcü-Yoldaş, A., Krühler, T., Greiner, J., Yoldaş, A., Clemens, C., Szokoly, G., Primak, N., & Klose, S. 2008, in AIPC Ser., Vol. 1000, AIPC Ser., ed. M. Galassi, D. Palmer, & E. Fenimore, 227

Lamb, D. Q., Donaghy, T. Q., & Graziani, C. 2005, ApJ, 620, 355

Lamb, D. Q. & Reichart, D. E. 2000, ApJ, 536, 1

Landsman, W. B. & Sbarufatti, B. 2008, GCN, 7965

Lazzati, D., Rossi, E., Covino, S., Ghisellini, G., & Malesani, D. 2002, A&A, 396, L5

Le Floc'h, E. et al. 2003, A&A, 400, 499

Ledoux, C., Jakobsson, P., Jaunsen, A. O., Thöne, C. C., Vreeswijk, P. M., Malesani, D., Fynbo, J. P. U., & Hjorth, J. 2007, GRB Coordinates Network, 7023

Levan, A. J. et al. 2006, ApJ, 648, L9

Li, A., Liang, S. L., Kann, D. A., Wei, D. M., Klose, S., & Wang, Y. J. 2008, ApJ, 685, 1046

Liang, E.-W., Racusin, J. L., Zhang, B., Zhang, B.-B., & Burrows, D. N. 2008, ApJ, 675, 528

Liang, E. W. et al. 2006, ApJ, 646, 351

Liang, S. L. & Li, A. 2009, ApJ, 690, L56

Lipkin, Y. M. et al. 2004, ApJ, 606, 381

Lipunov, V. M., Postnov, K. A., & Prokhorov, M. E. 2001, Astronomy Reports, 45, 236

Lithwick, Y. & Sari, R. 2001, ApJ, 555, 540

Loeb, A. & Barkana, R. 2001, ARA&A, 39, 19

MacFadyen, A. I. & Woosley, S. E. 1999, ApJ, 524, 262

MacFadyen, A. I., Woosley, S. E., & Heger, A. 2001, ApJ, 550, 410

Madau, P. 1995, ApJ, 441, 18

Maiolino, R., Schneider, R., Oliva, E., Bianchi, S., Ferrara, A., Mannucci, F., Pedani, M., & Roca Sogorb, M. 2004, Nature, 431, 533

Malesani, D. et al. 2007, A&A, 473, 77

Mangano, V., Sbarufatti, B., La Parola, V., Troja, E., Evans, P., & Immler, S. 2007, GRB Coordinates Network, 6702

McBreen, S., Hanlon, L., McGlynn, S., McBreen, B., Foley, S., Preece, R., von Kienlin, A., & Williams, O. R. 2006, A&A, 455, 433

McBreen, S. et al. 2008, ApJ, 677, L85

McGlynn, S. et al. 2005, Nuovo Cimento C, 28, 481

Meegan, C. et al. 2009, ArXiv e-prints

Meegan, C. A., Fishman, G. J., Wilson, R. B., Horack, J. M., Brock, M. N., Paciesas, W. S., Pendleton, G. N., & Kouveliotou, C. 1992, Nature, 355, 143

Mészáros, P. 2002, ARA&A, 40, 137

—. 2006, Rep. Prog. Phys., 69, 2259

Mészáros, P., Laguna, P., & Rees, M. J. 1993, ApJ, 415, 181

Mészáros, P. & Rees, M. J. 1993, ApJ, 405, 278

—. 1997, ApJ, 476, 232

—. 1999, MNRAS, 306, L39

Mészáros, P., Rees, M. J., & Papathanassiou, H. 1994, ApJ, 432, 181

Mészáros, P., Rees, M. J., & Wijers, R. A. M. J. 1998, ApJ, 499, 301

Molinari, E. et al. 2007, A&A, 469, L13

Monet, D. G. et al. 2003, AJ, 125, 984

Motta, V. et al. 2002, ApJ, 574, 719

Nakar, E. 2007, Phys. Rep., 442, 166

Nakar, E. & Granot, J. 2007, MNRAS, 380, 1744

Nakar, E. & Piran, T. 2004, MNRAS, 353, 647

—. 2005, MNRAS, 360, L73

Natta, A. & Panagia, N. 1984, ApJ, 287, 228

Noll, S., Pierini, D., Pannella, M., & Savaglio, S. 2007, in ASPC Ser., Vol. 380, Deepest Astronomical Surveys, ed. J. Afonso, H. C. Ferguson, B. Mobasher, & R. Norris, p. 461

Norris, J. P., Marani, G. F., & Bonnell, J. T. 2000, ApJ, 534, 248

Norris, J. P., Nemiroff, R. J., Bonnell, J. T., Scargle, J. D., Kouveliotou, C., Paciesas, W. S., Meegan, C. A., & Fishman, G. J. 1996, ApJ, 459, 393

Nousek, J. A. et al. 2006, ApJ, 642, 389

Nysewander, M., Reichart, D. E., Crain, J. A., Foster, A., Haislip, J., Ivarsen, K., Lacluyze, A., & Trotter, A. 2007, arXiv: 0708.3444

Oates, S. R. et al. 2009, MNRAS, 395, 490

O'Brien, P. T. et al. 2006, ApJ, 647, 1213

Oke, J. B. & Gunn, J. E. 1983, ApJ, 266, 713

Ota, K. et al. 2008, ApJ, 677, 12

Paciesas, W. S. et al. 1999, ApJS, 122, 465

Paczynski, B. 1986, ApJ, 308, L43

—. 1998, ApJ, 494, L45

Page, K. L. et al. 2007, ApJ, 663, 1125

Panaitescu, A. 2005, MNRAS, 363, 1409

—. 2006, Nuovo Cimento B Serie, 121, 1099

Panaitescu, A. & Kumar, P. 2000, ApJ, 543, 66

Panaitescu, A., Mészáros, P., Burrows, D., Nousek, J., Gehrels, N., O'Brien, P., & Willingale, R. 2006a, MNRAS, 369, 2059

Panaitescu, A., Mészáros, P., Gehrels, N., Burrows, D., & Nousek, J. 2006b, MNRAS, 366, 1357

Panaitescu, A., Mészáros, P., & Rees, M. J. 1998, ApJ, 503, 314

Panaitescu, A. & Vestrand, W. T. 2008, MNRAS, 387, 497

Pandey, S. B. et al. 2006, A&A, 460, 415

Pedersen, H. et al. 1998, ApJ, 496, 311

Pe'er, A., Ryde, F., Wijers, R. A. M. J., Mészáros, P., & Rees, M. J. 2007, ApJ, 664, L1

Pei, Y. C. 1992, ApJ, 395, 130

Peng, F., Königl, A., & Granot, J. 2005, ApJ, 626, 966

Perley, D. A., Chornock, R., & Bloom, J. S. 2008a, GCN, 7962

Perley, D. A. et al. 2008b, ApJ, 672, 449

Perna, R., Armitage, P. J., & Zhang, B. 2006, ApJ, 636, L29

Perri, M. et al. 2007, A&A, 471, 83

Piran, T. 1999, Phys. Rep., 314, 575

—. 2000, Phys. Rep., 333, 529

—. 2005, Reviews of Modern Physics, 76, 1143

Piran, T., Sari, R., & Zou, Y.-C. 2009, MNRAS, 393, 1107

Preece, R. D., Briggs, M. S., Mallozzi, R. S., Pendleton, G. N., Paciesas, W. S., & Band, D. L. 2000, ApJS, 126, 19

Prevot, M. L., Lequeux, J., Prevot, L., Maurice, E., & Rocca-Volmerange, B. 1984, A&A, 132, 389

Prochaska, J. X., Thöne, C. C., Malesani, D., Fynbo, J. P. U., & Vreeswijk, P. M. 2007, GRB Coordinates Network, 6698

Racusin, J. L., Liang, E. W., Burrows, D. N., Falcone, A., Sakamoto, T., Zhang, B. B., Zhang, B., Evans, P., & Osborne, J. 2009, ApJ, 698, 43

Racusin, J. L. et al. 2008, Nature, 455, 183

Ramirez-Ruiz, E., Celotti, A., & Rees, M. J. 2002, MNRAS, 337, 1349

Rees, M. J. & Mészáros, P. 1992, MNRAS, 258, 41P

—. 1994, ApJ, 430, L93

—. 1998, ApJ, 496, L1

Rhoads, J. E. 1997, ApJ, 487, L1

—. 1999, ApJ, 525, 737

Richardson, D., Branch, D., & Baron, E. 2006, AJ, 131, 2233

Rol, E., Wijers, R. A. M. J., Kouveliotou, C., Kaper, L., & Kaneko, Y. 2005, ApJ, 624, 868

Romano, P. et al. 2006a, A&A, 456, 917

—. 2006b, A&A, 450, 59

Roming, P. W. A. et al. 2005, Space Science Reviews, 120, 95

—. 2006, ApJ, 652, 1416

—. 2009, ApJ, 690, 163

Rossi, E., Lazzati, D., & Rees, M. J. 2002, MNRAS, 332, 945

Rossi, E. M., Lazzati, D., Salmonson, J. D., & Ghisellini, G. 2004, MNRAS, 354, 86

Rybicki, G. B. & Lightman, A. P. 1979, Radiative processes in astrophysics

Rykoff, E. S. et al. 2004, ApJ, 601, 1013

—. 2009, ArXiv: 0904.0261

Sakamoto, T. et al. 2005, ApJ, 629, 311

—. 2008, ApJ, 697, 570

—. 2009, ApJ, 693, 922

Salvaterra, R. et al. 2009, ArXiv:0906.1578

Sari, R. & Piran, T. 1999, ApJ, 520, 641

Sari, R., Piran, T., & Halpern, J. P. 1999, ApJ, 519, L17

Sari, R., Piran, T., & Narayan, R. 1998, ApJ, 497, L17

Sato, G. et al. 2007, ApJ, 657, 359

Savage, B. D. & Sembach, K. R. 1996, ARA&A, 34, 279

Savaglio, S. 2006, New Journal of Physics, 8, 195

Savaglio, S. & Fall, S. M. 2004, ApJ, 614, 293

Savaglio, S., Glazebrook, K., & LeBorgne, D. 2009, ApJ, 691, 182

Sbarufatti, B., Baumgartner, W. H., Evans, P. A., Guidorzi, C., Hoversten, E. A., La Parola, V., Mangano, V., Markwardt, C. B., Page, K. L., Romano, P., & Ukwatta, T. N. 2008, GCN, 7957

Schady, P. et al. 2007, MNRAS, 377, 273

Schlegel, D. J., Finkbeiner, D. P., & Davis, M. 1998, ApJ, 500, 525

Schulze, S., Kann, D. A., Rossi, A., Gonsalves, E., Hoegner, C., & Stecklum, B. 2008, GCN, 7972

Seaton, M. J. 1979, MNRAS, 187, 73P

Shemi, A. & Piran, T. 1990, ApJ, 365, L55

Skrutskie, M. F. et al. 2006, AJ, 131, 1163

Smith, J. A. et al. 2002, AJ, 123, 2121

Spruit, H. C. & Drenkhahn, G. D. 2004, in ASPC Ser., Vol. 312, ASPC Ser., ed. M. Feroci, F. Frontera, N. Masetti, & L. Piro, 357

Stamatikos, M. et al. 2007, GRB Coordinates Network, 7029

Stanek, K. Z., Garnavich, P. M., Kaluzny, J., Pych, W., & Thompson, I. 1999, ApJ, 522, L39

Stanek, K. Z. et al. 2003, ApJ, 591, L17

Stetson, P. B. 1987, PASP, 99, 191

Stratta, G., Fiore, F., Antonelli, L. A., Piro, L., & De Pasquale, M. 2004, ApJ, 608, 846

Stratta, G., Maiolino, R., Fiore, F., & D'Elia, V. 2007, ApJ, 661, L9

Stroh, M. C., Falcone, A., & Racusin, J. L. 2007a, GRB Coordinates Network, 7027

Stroh, M. C. et al. 2007b, GRB Coordinates Network, 7020

Tanvir, N. R. et al. 2009, Nature, accepted, ArXiv:0906.1577

Tody, D. 1993, in ASPC Ser., Vol. 52, Astronomical Data Analysis Software and Systems II, ed. R. J. Hanisch, R. J. V. Brissenden, & J. Barnes, 173

Totani, T., Kawai, N., Kosugi, G., Aoki, K., Yamada, T., Iye, M., Ohta, K., & Hattori, T. 2006, PASJ, 58, 485

Tueller, J. et al. 2008, GCN, 7969

Updike, A. C. et al. 2008, ApJ, 685, 361

Usov, V. V. 1994, MNRAS, 267, 1035

van Paradijs, J., Kouveliotou, C., & Wijers, R. A. M. J. 2000, ARA&A, 38, 379

van Paradijs, J. et al. 1997, Nature, 386, 686

Vestrand, W. T. et al. 2005, Nature, 435, 178

—. 2006, Nature, 442, 172

Vietri, M. 1997, ApJ, 488, L105

Vlahakis, N., Peng, F., & Königl, A. 2003, ApJ, 594, L23

Vreeswijk, P. M. et al. 2004, A&A, 419, 927

Wang, X. & Loeb, A. 2000, ApJ, 535, 788

Watson, D. et al. 2006, ApJ, 652, 1011

Wijers, R. A. M. J. & Galama, T. J. 1999, ApJ, 523, 177

Wijers, R. A. M. J., Rees, M. J., & Mészáros, P. 1997, MNRAS, 288, L51

Wijers, R. A. M. J. et al. 1999, ApJ, 523, L33

Wild, V., Hewett, P. C., & Pettini, M. 2006, MNRAS, 367, 211

Woods, E. & Loeb, A. 1999, ApJ, 523, 187

Woosley, S. E. 1993, ApJ, 405, 273

Woosley, S. E. & Bloom, J. S. 2006, ARA&A, 44, 507

Yamazaki, R., Ioka, K., & Nakamura, T. 2002, ApJ, 571, L31

Yüksel, H., Kistler, M. D., Beacom, J. F., & Hopkins, A. M. 2008, ApJ, 683, L5

Zeh, A., Klose, S., & Hartmann, D. H. 2004, ApJ, 609, 952

Zeh, A., Klose, S., & Kann, D. A. 2006, ApJ, 637, 889

Zhang, B. 2007, Chinese Journal of Astronomy and Astrophysics, 7, 1

Zhang, B., Fan, Y. Z., Dyks, J., Kobayashi, S., Mészáros, P., Burrows, D. N., Nousek, J. A., & Gehrels, N. 2006, ApJ, 642, 354

Zhang, B. & Kobayashi, S. 2005, ApJ, 628, 315

Zhang, B., Kobayashi, S., & Mészáros, P. 2003a, ApJ, 595, 950

Zhang, B. & Mészáros, P. 2002a, ApJ, 571, 876

—. 2002b, ApJ, 566, 712

—. 2004, International Journal of Modern Physics A, 19, 2385

Zhang, W., Woosley, S. E., & Heger, A. 2004, ApJ, 608, 365

Zhang, W., Woosley, S. E., & MacFadyen, A. I. 2003b, ApJ, 586, 356

Ziaeepour, H. et al. 2008, MNRAS, 385, 453

Danksagung

Ich bedanke mich sehr herzlich bei allen Personen, die diese Arbeit maßgeblich beeinflusst, gefördert und ermöglicht haben: Ganz besonders bei meinem Betreuer und GROND PI Jochen und bei allen Mitgliedern des GROND Teams. Herzlichen Dank Abdullah, Adria, Andrea, Aybüke, Benni, Clemi, Felipe, Fritz, Gyula, Heinz, Paulo, Robert, Martin, Matthias, Natalia, Sebastian, Stefan, Sylvio, Uwe und Walter. Desweiteren danke ich allen, die mir außer den eben Genannten mit Rat und Tat bei der Arbeit geholfen haben: Andreas, Alex, Arne, Elisabetta, Sheila und Sandra. Ich bedanke mich außerdem beim "Cluster of Excellence for Fundamental Physics: Origin and Structure of the Universe", beim MPE, und insbesondere bei allen Mitgliedern und dem früheren Leiter der Hochenergieastrophysik Günther Hasinger. Grosser Dank gebührt auch der Belegschaft des LaSilla Observatoriums fürs Kochen, Putzen, Waschen, Fußball spielen und nicht zuletzt für die Unterstützung beim Beobachten.

Zum Schluss bedanke ich mich noch ganz besonders bei meinen Eltern und Schwestern Susanne und Andrea, für ihre andauernde Unterstützung, Zusprache, Zuneigung und Geduld bei jedwedem Problem. Ihr seid die beste Familie die man sich wünschen kann. Und zu allerletzt bedanke ich mich bei der Person, ohne die nichts so schön wäre, wie es ist: Danke, Sabine!